NTNU – Trondheim
Norwegian University of
Science and Technology

Energy absorption and damage prevention in a submerged floating tunnel during internal blast loading

Anders Tømte

Civil and Environmental Engineering (2 year)
Submission date: June 2015
Supervisor: Aase Gavina Roberg Reyes, KT
Co-supervisor: Tore Børvik, KT
Martin Kristoffersen, KT

Norwegian University of Science and Technology
Department of Structural Engineering

Department of Structural Engineering
FACULTY OF ENGINEERING SCIENCE AND TECHNOLOGY
NTNU – Norwegian University of Science and Technology

MASTER'S THESIS 2015

for

Anders Tømte

Energy absorption and damage prevention in a submerged floating tunnel during internal blast loading

1. INTRODUCTION

Protection of engineering structures against blast loading has received a lot of attention in recent years. The newly proposed coastal highway route E39 seeks to connect Trondheim to Kristiansand along the coast without using any ferry connections. One of the critical points is the crossing of the Sognefjord, where a submerged floating tunnel made of normal-strength concrete has been suggested as a means of crossing. Internal blast loading (due to e.g. an accident or a terrorist attack) to a structure like this can be extremely critical, and it is important to verify that the structure is able to withstand a realistic blast load, or at least minimise the damage, as a breach could have disastrous consequences. Aluminium foam may be used as an internal liner to absorb energy and thereby protect the concrete walls against the blast load. Computational methods are now available to predict both the loading and structural response in these extreme loading situations, and experimental validation of such methods is necessary in the development of safe and cost-effective structures. In this study blast experiments will be performed, and the data will be used for validation and verification of some frequently used computational methods involving blast loading.

2. OBJECTIVES

The main objective of the research project is to investigate how aluminium foam behaves under blast loading, and to validate to which extent this can be predicted using computational tools.

3. A SHORT DESCRIPTION OF THE RESEARCH PROJECT

The main topics in the research project will be as follows;

1. A comprehensive literature review should be conducted to understand the blast load phenomenon, blast load design, shock tube facilities, constitutive and failure modelling of aluminium foam exposed to extreme loadings, and explicit finite element methods.
2. Aluminium foams with various densities should be considered.
3. Proper constitutive relations and failure criteria are chosen and calibrated based on material tests.
4. The SIMLab Shock Tube Facility will be used to expose sandwich structures consisting of thin aluminium plates and aluminium foam to blast loading, as an alternative to explosive detonations. The shock tube experiments will be used to investigate typical dynamic responses and failure modes of the plated structures exposed to blast loading.
5. Non-linear FE numerical simulations of the shock tube experiments will be performed, and the numerical results shall be compared and discussed based on the experimental findings.

Supervisors: Aase Reyes (NTNU), Martin Kristoffersen (NTNU), Tore Børvik (NTNU)

The thesis must be written according to current requirements and submitted to the Department of Structural Engineering, NTNU, no later than June 10th, 2015.

NTNU, January 14th, 2015

Aase Reyes
Professor

Preface

This master's thesis is written at Structural Impact Laboratory (SIMLab), Department of Structural Engineering at Norwegian University of Science and Technology (NTNU), spring 2015.

I would like to thank my supervisor Professor Aase Gavina Roberg Reyes for great assistance and advice during the process. Assistant supervisor Professor Tore Børvik also deserves credit for great advice regarding blast loads and general involvement in the thesis. PhD candidate Vegard Aune was involved in the Shock Tube experiments and deserves thanks for his dedication and advice regarding the experiments. Special thanks goes to David Morin for help with setting up the numerical model and research scientist Trond Auestad for great help with the experiments.

Trondheim, NTNU, 10. Juni 2015

Anders Tømte

Abstract

Experiments on sandwich structures with an aluminum foam core and aluminum sheet plates are done in the shock tube facility at SIMLab. Aluminum foam is a lightweight material with many applications in a wide range of fields. It is a good energy absorber in uniaxial compression and therefore a great protective material. Additionally, aluminum foam is good at absorbing sound and has great fire resistance.

The Norwegian Public Roads Administration (NPRA) currently investigates the possibility of building a submerged floating tunnel across the Sognefjord. The investigation is part of a project to remove all ferries across the fjords along Norway's coastal highway (E39). An important consideration regarding the safety of such a structure is the resistance against explosions caused by an accident inside the tunnel or other sources.

When an explosion occurs, a blast wave will be generated and propagate away from the source. A shock tube facility is used to simulate the properties of a blast wave and for investigating blast effects on structures like sandwich plates with aluminum foam core.

Uniaxial compression tests on aluminum foam are performed to achieve the material properties before the sandwich plates are tested in the shock tube. A strain-hardening model for uniaxial and hydrostatic compression is calibrated with the stress-strain curves from the uniaxial compression tests. A power-law description is used to account for the density sensitivity of aluminum foam. The densities of the aluminum plates ranged from 0.21 to 0.42 g/cm^3. Various degree of failure was observed in the foam for the different tests in the shock tube.

A numerical model have been created in Abaqus/Explicit as an attempt to simulate the shock tube experiments. A Matlab script provided the input parameters required for the simulations. Results from the analyses showed some similarities between the analyses and the experiments. The displacements were quite accurate, but the failure of the aluminum foam core were somewhat different in the numerical analyses compared to the experiments in the shock tube.

At the end, parameter studies are performed on sandwich structures with an equivalent thickness compared to monolithic aluminum plates, and on a concrete plate with an aluminum foam layer. The results from the equivalent thickness study showed that an equivalent sandwich structure did not performed better than the monolithic plate. From the analyses on concrete plates with an aluminum foam layer, the response in the concrete part increased when adding aluminum foam.

Sammendrag

Aluminiumskum er et lett materiale i forhold til sin styrke i trykk. Det har mange nyttige egenskaper som kan brukes til en rekke formål. Materialet er godt egnet til å oppta energi når det blir utsatt for laster i rent trykk. Derfor tenkes det at det kan være nyttig til å beskytte større konstruksjoner mot ytre påvirkninger som eksplosjoner. Aluminiumskum isolerer også godt mot lyder og har gode beskyttelsesegenskaper mot brann. Sandwichplater med aluminiumsskumkjerne har blitt testet i en shocktube for å finne ut hvordan materialet oppfører seg under eksplosjonslaster.

Statens Vegvesen gjennomfører i disse dager en studie om bygging av en rørtunnel over Sognefjorden. Denne studien er en del av et større prosjekt populært kalt ''Fergefri E39'', hvor målet er å sørge for at fergene som i dag er nødvendige for å krysse de brede og dype fjordene langs E39 blir avviklet. For å oppnå dette er det nødvendig å finne nye og innovative bruløsninger. En viktig faktor i prosjekteringen av en eventuell rørtunnel er dens sikkerhet mot eksplosjoner forårsaket av ulykker eller terrorangrep.

Når en eksplosjon oppstår, vil en trykkbølge oppstå og spre seg vekk fra der den oppsto. En shocktube kan simulere egenskapene til en trykkbølge og brukes til å undersøke effekter fra eksplosjoner på sandwichplatene med kjerne av aluminiumskum.

Enaksiale trykkforsøk har blitt gjennomført for å finne egenskapene til aluminiumskummet. En fastningsmodell for enaksialt og hydrostatisk trykk ble kalibrert med spenning-tøyningsdiagram fra enaksiale trykkforsøk. En potensligning ble introdusert for å ta hensyn til skummets densitet. Densiteten til aluminiumskummet varierte fra 0.21 til 0.42 g/cm^3. Fra testene i shocktuben ble det observert brudd i skummet i større eller mindre grad avhengig av hvilken densitet og hvilket trykk som ble testet for.

En numerisk modell ble etablert i Abaqus/Eksplisitt for å simulere forsøkene i shocktuben. Ved hjelp av et script fra Matlab ble alle inputparameterne generert til simuleringene. Resultatene fra analysene og forsøkene ble sammenlignet og viste en del likheter i forskyvning, men bruddet i skummet viste mer varierende verdier.

Til slutt ble det gjennomført noen parameterstudier i Abaqus/Eksplisitt. Et parameterstudie ble gjennomført for å sammenligne sandwichplater med samme vekt som 4 mm monolittiske aluminiumsplater og et annet parameterstudie ble gjort for å se på effekten av aluminiumskum på betongplater.

Contents

Nomenclature

a	Length of plate
a_1	Speed of sound
b	Decay coefficient
c_d	Dilatational wave speed
C_0	Constant
C_1	Constant
d	Diameter
D	Flexural rigidity
e	Engineering strain
e_V	Volumetric engineering strain
E	Young's modulus
f	Yield function
f_{ck}	Compression strength
f_{ct}	Splitting tension strength
F	Force
h	Enthalpy
i_s	Specific impulse
I_r	Reflected impulse
L	Length
L_0	Initial length
L^e	Characteristic length of an element in a FE mesh
m	Molecular weight
M_S	Mach number
M_x	Bending moment
n	Constant
p	Hydrostatic pressure
P	Pressure
P_{Dyn}	Dynamic pressure
P_{Sta}	Static pressure
P_{Stag}	Stagnation pressure
P_0	Ambient pressure
P_r	Peak reflected overpressure
P_s	Peak side-on overpressure
q	Uniform static pressure
R	Stand-off distance, gas constant
t	Thickness of plate, time
t_+	Positive phase of a shock wave
t_-	Negative phase of a shock wave
t_a	Shock front arrival time
T	Temperature
u	Flow velocity
U	Energy absorption
U_S	Velocity of shock wave
v	Particle velocity
w_C	Displacement in the field
W	Equivalent mass TNT
x, y, z	Cartesian coordinates
Y	Yield strength

Z	Scaled distance
α	Pressure-sensitivity coefficient
α_2	Scale factor
β	Shape factor
ε	Logarithmic (true) strain
$\dot{\bar{\varepsilon}}$	Equivalent strain rate
ε_D	Densification strain
$\dot{\varepsilon}_{ij}^P$	Plastic strain rate tensor
ε_V	Volumetric logarithmic (true) strain
$\dot{\epsilon}_e$	Von Mises effective plastic strain rate
$\dot{\epsilon}_m$	Volumetric plastic strain rate
$\dot{\epsilon}_{ij}^{\prime P}$	Deviatoric plastic strain rate tensor
γ	Linear strain-hardening coefficient
γ_1	Ratio of heat capacity at constant pressure and constant volume
δ_{ij}	Kroenecker delta
ν	Poisson's ratio
ν^P	Plastic Poisson's ratio
ρ_f	Foam density
ρ_{f0}	Base material density
σ	Stress
$\hat{\sigma}$	Equivalent stress
σ_d	Dynamic plateau stress
σ_e	Von Mises effective stress, engineering stress
$\sigma_{ij}^{\prime}$	Deviatoric stress tensor
σ_m	Mean stress
σ_p	Plateau stress
σ_s	Tension failure stress
σ_t	True stress
Φ	Yield function

1 Introduction

1.1 Background

The Norwegian Public Roads Administration (NPRA) are currently investigating the potential of eliminating all ferries along Norway's coastal highway E39 [1]. The road is part of the European trunk road system and runs along the western coast of Norway from Kristiansand in south to Trondheim in central Norway. The distance is almost 1100 km and eight ferries currently works along the route. The fjords in western Norway are wide and deep and in order to create a highway free of ferries, massive investments and innovation is needed to create concepts capable of dealing with large widths and deep water levels. The project may reduce the travelling time from Kristiansand to Trondheim by 7-9 hours, to a total of about 12-13 hours.

1.2 Crossing of the Sognefjord

The Sognefjord is used as a pilot site for developing new concepts for bridges because it is 4 km wide and because vast depths of down to 1300 m makes anchoring to the bottom difficult. This makes the Sognefjord the most difficult and challenging fjord to cross. There are three main alternatives for crossing the Sognefjord: a suspension bridge, a floating bridge, or a submerged floating tunnel. Combinations of the three are also considered.

A submerged floating tunnel is the alternative that will be related to this thesis. A concept developed by Reinertsen Olav Olsen Group for a submerged floating tunnel is described roughly in [2], and more detailed in [3]. This concept consists of two circular cross-sections in concrete connected together with a truss. The outer diameter of the concrete tubes is 12.6 m and the thickness of the wall is 0.8 m. The submerged floating tunnel is located in a horizontal curve with a radius of 2682 m and the total length of the structure is 4083 m. The feasibility study done by Reinertsen Olav Olsen Group is a robust and flexible solution regarding the functional and environmental demands from the society.

1.3 Safety of a submerged floating tunnel

An important consideration regarding the safety of a submerged floating tunnel is the resistance against accidents that may cause a hazardous explosion inside the tunnel. In a worst-case scenario, a semi-trailer carrying huge load of flammable gas can collide in some way and hit the walls in the tunnel or other vehicles. This has the potential of creating a massive explosion inside the tunnel and expose the structure with rapid, high-pressure impulsive loads. It is important that the concrete walls can withstand this impulsive load and that no collapse or cracking let water into the tunnel. The construction costs for this type of projects are huge and a disastrous accident will influence the society both economically and socially.

Therefore, it is important to investigate how to protect the main structure against damages caused by this type of extreme load cases. In this thesis, aluminum foam based structures are investigated as possible energy absorbing material against blast loadings. The effect of

aluminum foam as a protective layer on concrete walls were initially the subject for this thesis. However, new findings during the process changed the scope of the thesis to focus only on the behavior of aluminum foam during blast loading.

1.4 Energy absorption of blast loading

First, it is important to get an overview of research done on the subject. Many researchers have shown interest in the behavior of different types of aluminum foam structures subjected to blast loadings in recent years. Aluminum foams as claddings on concrete panels or slabs and the behavior of sandwich panels under blast loading have been investigated. There have been used different setups for simulating an air blast wave. Some have performed experiments with TNT and compared results with numerical models, while others have used a shock tube facility similar as in this thesis. The structures tested varies in density, thickness and area with different boundary conditions. A short description of some of the most relevant papers on the subject are now presented.

1.4.1 Foam panels on concrete structures

In 2001, Hanssen et al. [4] performed full-scale field tests to investigate the behavior of aluminum foam panels subjected to blast loading. The test setup consisted of charges that detonated at a given stand-off distance from the foam panels connected to the bob of a ballistic pendulum. The calculation of the energy and impulse transfer was based on the maximum swing of the pendulum as shown in Fig. 1.

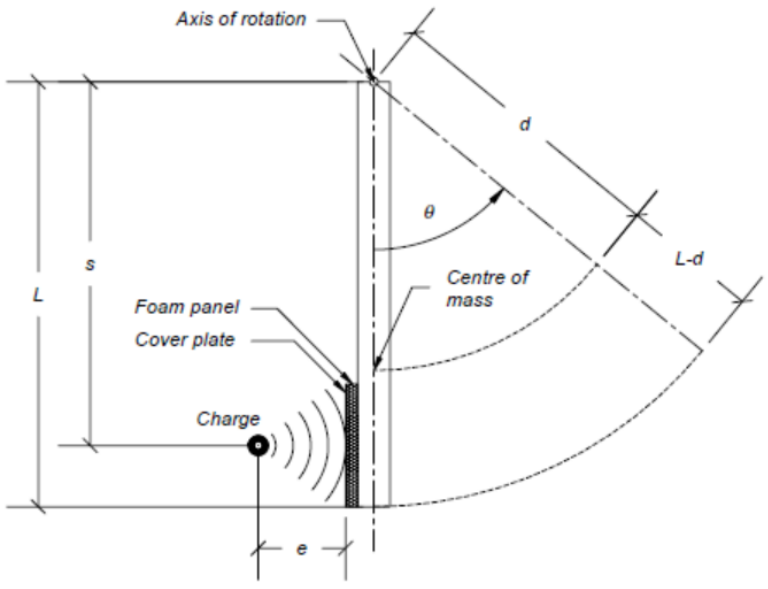

Fig. 1 Simplified illustration of blast-loaded pendulum [4]

They tested two different foam densities at 0.15 g/cm^3 and 0.35 g/cm^3 with charge masses of 1.0 kg and 2.5 kg PE4 at a stand-off distance of 500 mm. A 10 mm aluminum cover plate were added in some of the tests to investigate the effect. The results were quite surprising as the observed energy and impulse transfer increased by adding a foam panel. According to the

authors, a reason for the increased swing could be due to a continuous changing in the shape of the initially plane foam surface into a concave shape. Another important observation was the fact that a cover plate removed all fragmentation of the foam panels, but somehow increased the force levels transferred to the structure. The paper discussed the reasons for this phenomenon, but did not come up with a definite conclusion.

Schenker et al. [5] performed full-scale field tests of concrete slabs subjected to blast loads. One of the goals were to study the capabilities of aluminum foam to act as a structural protection layer against blast wave loads. The experimental setup consisted of two pairs of 3 m concrete slabs with an aluminum foam attached to one of the plates. An explosion of nearly 1000 kg hemispherical TNT charge at a stand-off distance of 20 m generated the blast wave. The experimental setup is shown in Fig. 2.

Fig. 2 experimental setup of 3 m span slabs mounted side by side [5]

The authors measured accelerations, velocities, displacements and cracks in the concrete after impact. The results clearly indicated that by adding a layer of aluminum foam on the concrete slabs, the concrete was less damaged and experienced lower accelerations, velocities and displacements. The conclusion was that when the aluminum foam was added, the response of the slab was modified, but a definite conclusion required more research and testing.

In 2011, Wu et al. [6] tested a total of five foam-protected concrete slabs and one control reinforced concrete (RC) slab against blast loading. The experiments conducted were full-scale blast tests on RC slabs with dimensions 2000 x 1000 x 100 mm. A steel frame was used together with bolts to clamp the concrete slab as in Fig. 3. A 5 m high and 3.7 m wide pipe frame was constructed to set up the charge at given stand-off distances above the test specimen. Fig. 4 shows a picture of the experimental setup.

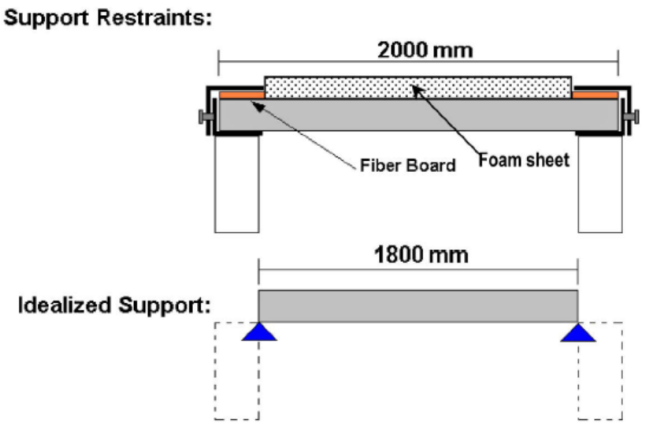

Fig. 3 Support conditions of the structure [6]

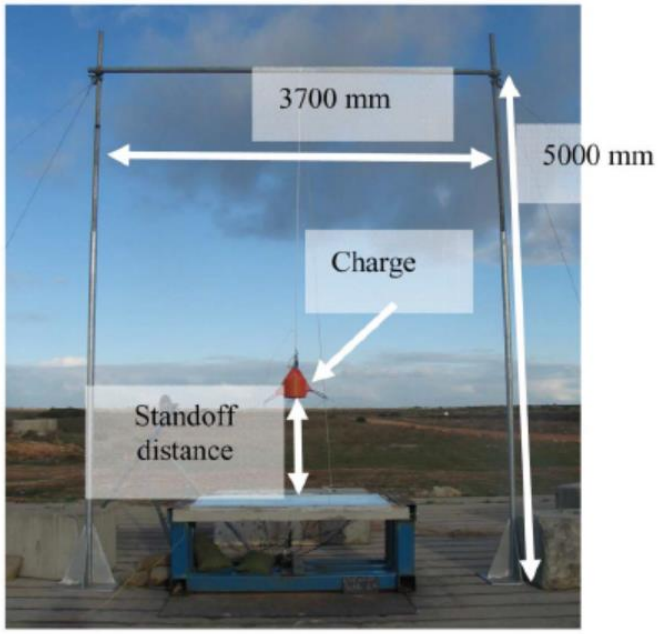

Fig. 4 Blast test setup [6]

The aluminum foam layers were 12.7 mm and 25 mm thick with density 0.45 g/cm^3, and 43.2 mm thick with density 0.14 g/cm^3. Blast waves from explosive charges consisting of the equivalent of 8.05 kg Composition B at stand-off distances 0.92 m, 1.47 m and 1.50 m loaded the structures. In order to check the efficiency of the aluminum foam layer, the authors measured incident overpressures, displacements, acceleration histories and strain histories along the depth of the slabs. Results showed that foam layers used to protect RC slabs were effective in protection against blast effects on the slabs.

Table 1 Summary of aluminum foam panels exposed to blast loading

Reference	Type of experiment	Loading	Results
Hanssen et al. [4]	Effect of blast loading on foam panels	Charge mass of 1.0-2.5 kg PE4 with stand-off distance 500 mm	Increased load levels when adding aluminum foam panels
Schenker et al. [5]	Foam panels on concrete slabs against a blast wave	Hemispheric, 1000 kg TNT blast at stand-off distance 20 m	Reduced the response on the concrete slab with aluminum foam
Wu et al. [6]	Blast testing on foam protected RC slabs	Explosives from 8 to 14 g at stand-off distance 1.5 m	Effective in protection against blast effects on the slabs

1.4.2 Sandwich panels

Zhu et al. [7] performed experiments on sandwich panels with different relative densities of the aluminum foam core. The specimens consisted of two identical face-sheets with thicknesses of 0.8 mm and 1.0 mm and relative foam densities of 6% and 10% with thicknesses 20 mm and 30 mm. A typical test specimen is shown in Fig. 5a. The structure was clamped with three Ø16 bolts on each side and Ø18 bolts at each corner. The loaded part of the plates were 250 x 250 mm as in Fig. 5b.

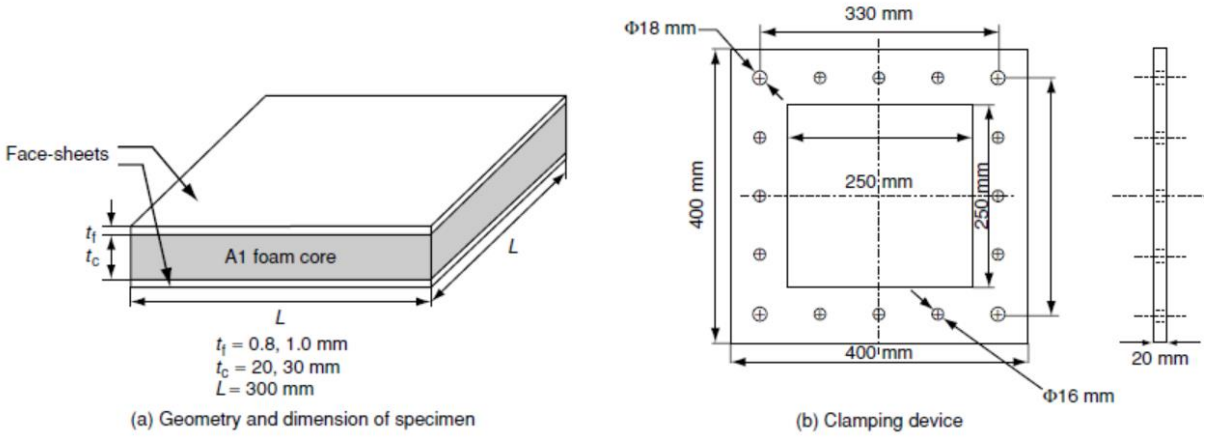

Fig. 5 Specimen and clamping device [7]

An explosive charge was placed in front of the center of the specimen with a stand-off distance of 200 mm. A four-cable pendulum system measured the impulsive loading on the structure. In addition, a thorough numerical analysis was performed to investigate the energy absorption and failure modes. Effects of impulse level, face-sheet thickness, relative density of the core and core thickness were discussed. The results showed that in the case of energy absorption, thinner face-sheets could raise the total internal energy while denser and thicker core could increase its portion of energy dissipation.

Liu et al. [8] investigated the response of sandwich panels with aluminum foam core under blast loading. A sandwich structure composed of two steel plates and an aluminum foam core, as shown in Fig. 6a, were tested. For comparison, experiments were also done on a structure as in Fig. 6b with three layers of steel plates. The steel sheets and foam core were placed on top of each other without an adhesive layer in between. The structure was clamped with four nails on each side of the square sandwich panel.

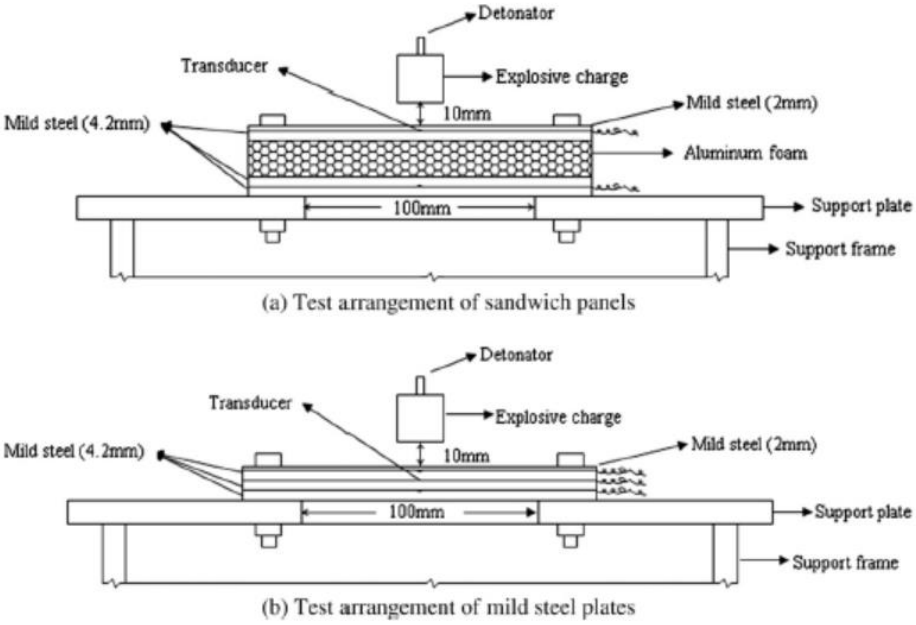

Fig. 6 Test arrangement in the experiment [8]

The explosive charge was placed 10 mm above the front face of the structure. Relative foam densities ranging from 0.16 to 0.23 were tested. The results showed a reduced peak load by at least 60% in the sandwich panels compared to mild steel plates alone. The dissipation of energy was mainly due to formation and growth of cracks.

Zhang et al. [9] tested three different corrugated core arrangements of sandwich steel plates. The experiment was done in a shock tube facility to simulate blast loads as seen in Fig. 7.

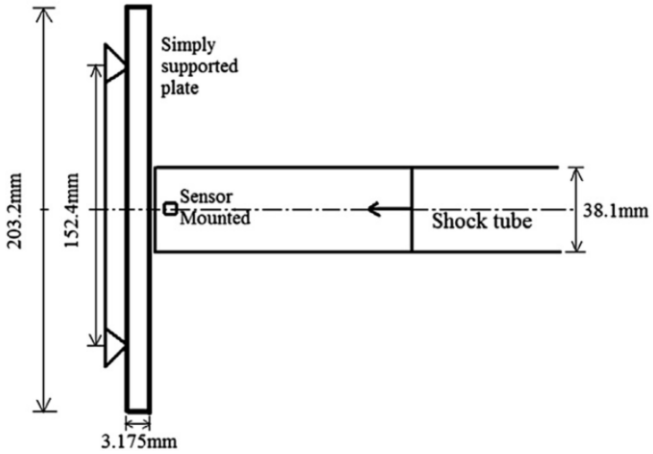

Fig. 7 A view of the shock tube [9]

The structure consisted of four corrugated layers arranged with uniform and non-uniform thickness. The shape of the corrugated layers was similar to a half-sine curve. Three different thicknesses were used to investigate the dynamic behavior. A simply supported plate with a span of 152.4 mm between the rigid supports were loaded with a pressure wave from the tube with a diameter of 38.1 mm.

The incident peak overpressure used in the study was 0.70 MPa. Results showed that the configuration with a smooth graded core from high to less relative density outperforms the other configurations with simply supported boundary conditions. An example of the deformation of the sandwich plates is shown in Fig. 8.

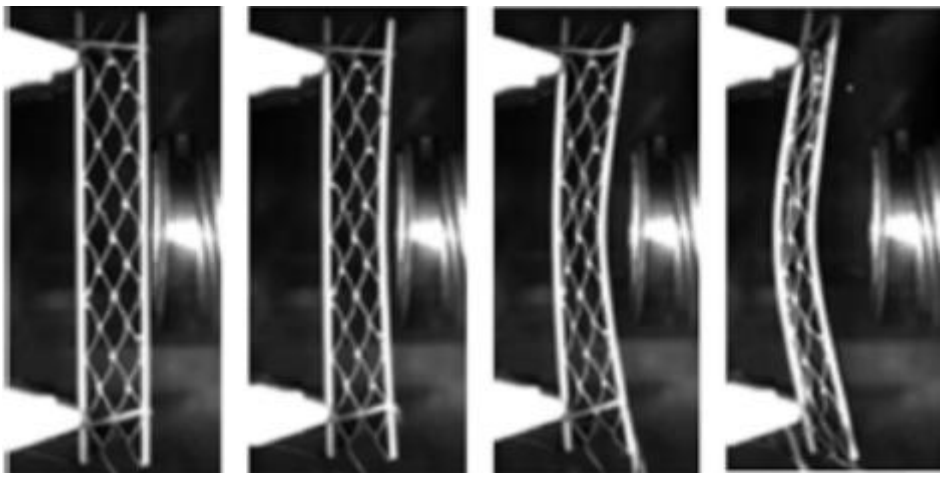

Fig. 8 Deformation of corrugated sandwich plate [9]

In 2013, Yazici et al. [10] performed similar experiments as in [9], but filled the core with polymeric foam to investiage the resistance against blast loading. The incident peak overpressure of the shock wave was 1.1 MPa in this experiment. The test specimen had face sheets of dimensions 50.8 x 203.2 x 3.2 mm and sinusoidal corrugated layers with thickness 0.44 mm. The boundary conditions were simply supported and a high-speed digital camera documented the deformation history. A numerical study was done to investigate the effect of fixed boundary conditions. Results showed that the face sheet thickness was more effective than the corrugated steel thickness when fixed boundary conditions were applied. When foam infill was used, the back-face deformation was reduced by more than 50%, while increasing the mass of the panel by only 2.30%.

Table 2 Summary of different sandwich structures subjected to blast loading

Reference	Type of experiment	Loading	Results	Comments
Zhu et al. [7]	Sandwich panels with an aluminum foam core against blast loading	Charge mass ranging from 20-40 g TNT with stand-off distance of 200 mm	Great energy dissipation in the foam core structure	
Liu et al. [8]	Aluminum foam-steel panel sandwich composites against blast loading	Cylindrical 10 g charge at 10 mm stand-off distance	Peak load reduced by approximately 62 % compared to mild steel plates alone	
Zhang et al. [9]	Sandwich panels with graded corrugated cores in a shock tube	Shock tube with peak reflected overpressure of 3 MPa	Midpoint deflections vary from 10-25 mm depending on core composition	Simply supported boundary conditions
Yazici et al. [10]	Foam filled corrugated core steel sandwich structures in a shock tube	Shock tube with peak reflected overpressure of 5.5 MPa	Displacements were reduced by more than 50 % when adding foam in the core	Simply supported boundary conditions

1.4.3 Summary

In addition to these investigations, other researchers such as Wadley and Deshpande suggests aluminum foam panels as an effective energy absorbing material and the behavior of sandwich structures against blast loadings. Wadley et al. [11] explored the possibility of utilizing the excellent absorption capacity of aluminum foams in protection against air blasts in order to minimize injuries caused by the explosion. Wadley et al. [12] experimentally investigated the mechanisms of projectile penetration of aluminum corrugated core sandwich panels. Liu et al. [13] investigated the response of buffer plates of solid face sheets backed by a foam core subjected to impulsive loading impacted by high-velocity soil. Park et al. [14] tested carbon fiber-epoxy composite square honeycombs in quasi-static and dynamic compression. St-Pierre et al. [15] explored the dynamic indentation response of sandwich panels with a corrugated or Y-frame core using the finite element method. Wadley et al. [16] explored deformations and fracture of impulsively loaded sandwich structures.

The use of aluminum foam panels as a sacrificial cladding on concrete structures is possibly a good way of protecting against a blast event, while sandwich structures is better at absorbing energy than mild steel plates alone. In addition, the use of a foam infill in the sandwich structure reduces deformations due to blast loading. A further investigation on this topic is to find out if aluminum foam plates are capable of dealing with high pressures from blast waves. Additionally, it could be useful to investigate the need of such protection materials in larger structures such as buildings and bridges. In this thesis, a sandwich structure with an aluminum

foam core and sheet plates made of aluminum with thickness 0.8 mm is considered. The sandwich structures will be tested in the SIMLab Shock Tube Facility and the results will be compared to numerical analyses. Later, it will be performed a numerical investigation on the effect of using aluminum foam in sandwich plates compared to monolithic aluminum plates. The effect of adding an aluminum foam layer on a concrete plate will also be investigated numerically. The main objective, however, is to investigate the behavior of aluminum foam in the shock tube and compare the results with numerical analyses.

2 Theory

2.1 Material properties

2.1.1 Aluminum

For the solid aluminum material, the von Mises criterion is used. This is an isotropic criterion and can be calibrated by a single uniaxial tension test. The theory is taken from Lubliner [17].

When the von Mises yield criterion is used in combination with the associated flow rule, the yield function becomes

$$f = J_2 - \left(Y/\sqrt{3}\right)^2 = 0 \tag{1}$$

where Y is the current yield stress of the material and

$$J_2 = \frac{1}{2}\sigma'_{ij}\sigma'_{ij} \tag{2}$$

while σ'_{ij} is the deviatoric stress tensor and defined as

$$\sigma'_{ij} = \sigma_{ij} - p \cdot \delta_{ij}. \tag{3}$$

Here, the hydrostatic stress tensor $p = \frac{1}{3}\sigma_{kk}$, and δ_{ij} represents the Kronecker delta.

When assuming isotropic hardening, the yield surface changes size uniformly in all directions such that the yield stresses increases uniformly with plastic straining.

Aluminum is rather rate-insensitive with respect to the flow stress according to Chen et al. [18]. Therefore, no rate-dependent effects are taken into account. By performing some differentiations the plastic strain increment becomes

$$d\varepsilon^p_{ij} = d\lambda\sigma'_{ij}. \tag{4}$$

In addition, after including the von Mises effective stress σ_e and effective plastic strain increment $d\varepsilon^p_{ij}$ before integrating, an expression for the plastic straining of the material becomes

$$\varepsilon^p_{ij} = \frac{3}{2}\frac{\varepsilon^p_e}{\sigma_e}\sigma'_{ij}. \tag{5}$$

2.1.2 Aluminum foam

A good understanding of the material properties is important in order to achieve appropriate accuracy and validation in the calculations. Aluminum foam is a material that has been considered and studied for many applications with respect to crashworthiness of structures. Unlike metals, aluminum foam is not a continuum, but rather a complicated three-dimensional cellular structure. This anatomy makes the material excellent in absorbing energy in compression through a nearly perfectly plastic force versus deformation curve. The material

has some great properties, which makes it useful in a wide range of fields. Some of these properties are non-combustibility, sound absorption, low weight to strength ratio, fire resistance and easy recycling. In this thesis, the energy absorption capacity is of major interest. Many researchers have engaged in the investigation of the mechanical behavior of metallic foams. Some of the factors that have been considered are inhomogeneous structure, complex non-linear behavior, strain-rate, density and hydrostatic stress tensor sensitivity.

Foam structure

Metallic foams are three-dimensional cellular structures with low density as an important advantage. The base material of the foam makes up the structure. The most common base material is aluminum, but other metal foams such as steel, titanium, zinc and magnesium also exist. Other types of foam structures are polymeric and organic foams. In fact, wood can also be considered as a cellular structure similar to metal or polymeric foams. Foams can be further divided into structures with closed cells and open cells.

However, in this thesis, aluminum foam produced by Hydro Aluminum AS is used. It is manufactured by a continuous casting procedure and a foam sheet is produced as shown in Fig. 9. For the aluminum foam plates used in this thesis, the base material consists of 8% silica and 0.5% magnesium balancing the aluminum (AlSi8Mg). The produced densities are in the range of 0.1 to 0.5 g/cm^3.

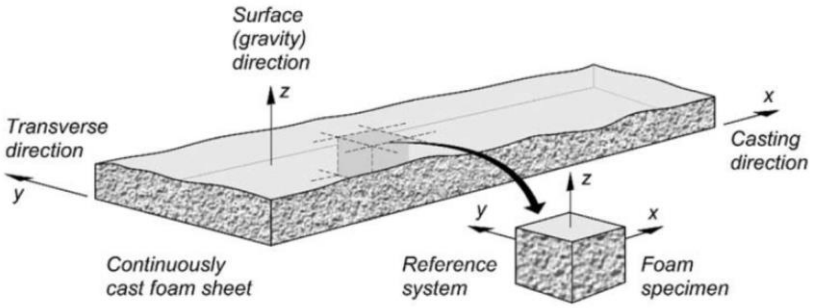

Fig. 9 Continuously casted foam sheet with reference system [19]

Hanssen et al. [19] introduced a reference system to increase control of anisotropy in the material properties coming from gravity forces or other process parameters. In Fig. 9, *x* denotes the casting direction, while the transverse *y*-direction is aligned with the width of the foam sheet and the z-direction is the direction through the thickness of the foam. The same reference system will be utilized in this thesis when describing the properties of foam.

The cell structure of the foam varies according to the direction considered. Examples of the cell structure in different directions are shown in Fig. 10.

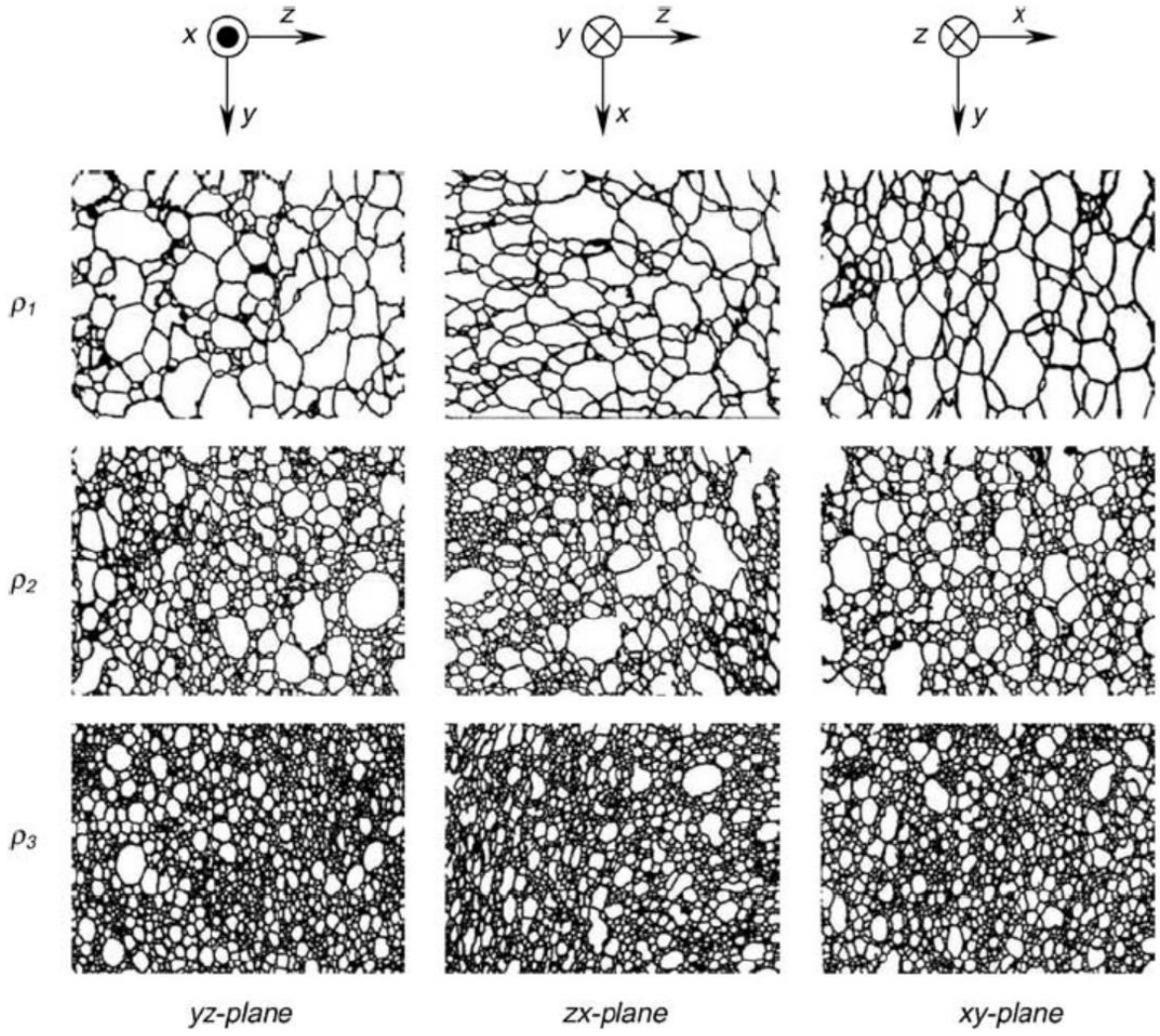

Fig. 10 Example of aluminum foam cell structure [19]

Foam properties

In order to get an appropriate model for aluminum foams, the behavior under uniaxial and hydrostatic compression was investigated. In reference [19], a lot of different tests on aluminum foams were performed, including uniaxial and hydrostatic compression, uniaxial tension and the effect of loading velocity. The foam tested is the same as the foam used in this thesis. Here, only properties from uniaxial compression have been tested.

For aluminum foams, the uniaxial, compressive behavior is described by a plateau region where the stresses increase slowly up to large strains. When the material is strained up to densification, the material will experience rapidly increasing stress levels.

Energy absorption of foam is related to the area under the stress-strain curve in compression [20]:

$$U = \int_0^{\varepsilon_D} \sigma \, d\varepsilon \tag{6}$$

Where U is the energy absorbed per unit initial volume up to the densification strain ε_D.

When aluminum foam is used as a protective cladding on a structure, not only the energy absorption itself should be considered. It is also important to keep the stress transferred to the structure behind as low as possible.

Aluminum foams experience large volumetric deformations for hydrostatic load conditions. The influence of hydrostatic pressure in the mechanical behavior is a fundamental factor in the constitutive modeling of aluminum foams.

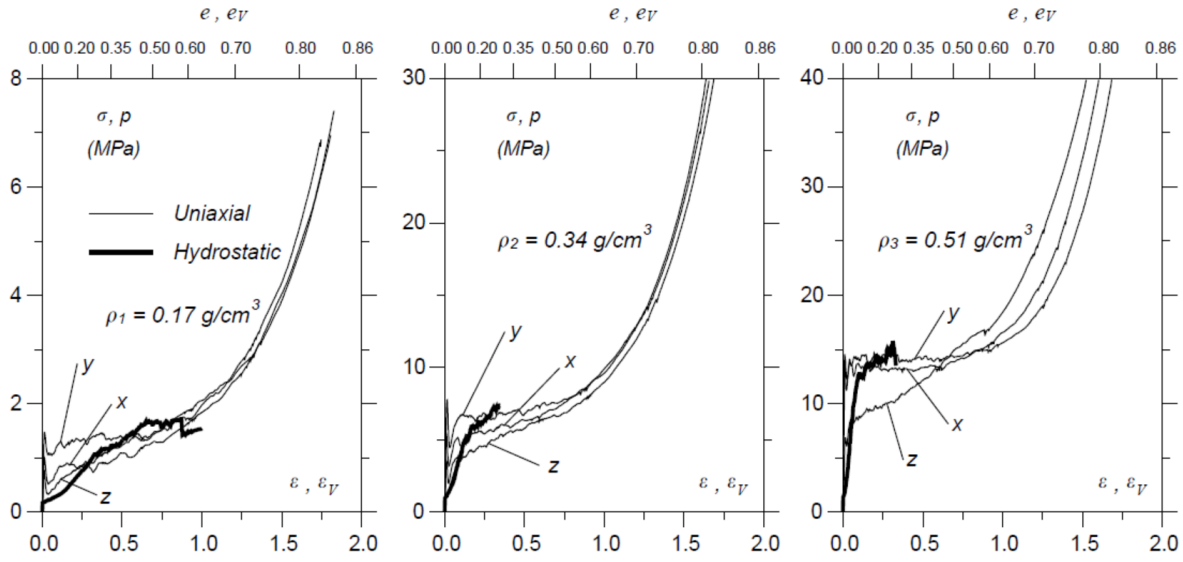

Fig. 11 Uniaxial and hydrostatic data for aluminum foam specimens [19]

The average results of the uniaxial and hydrostatic compression tests on aluminum foam cubes done in [19] are shown in Fig. 11. The influence of foam density and direction can be seen from the figure. For the uniaxial case, Fig. 11 shows true stress σ vs. both true strain ε and engineering strain *e*. Fig. 12 shows the development of the apparent Young's modulus E as a function of the same parameters. For hydrostatic loading, the pressure is denoted *p*, while e_V and ε_V gives the corresponding engineering and logarithmic volumetric strains.

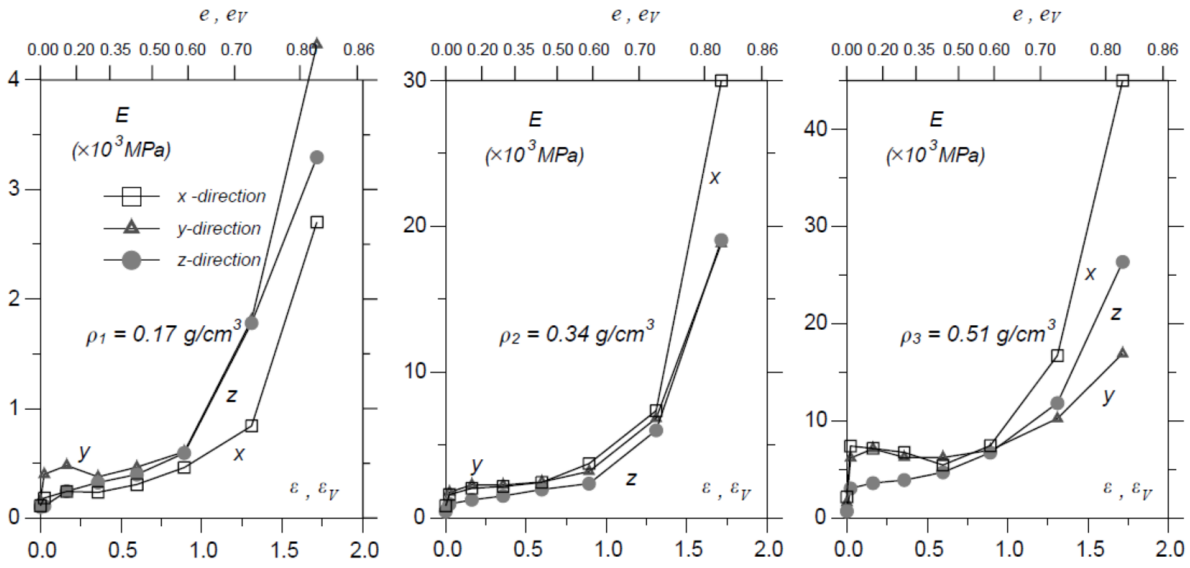

Fig. 12 Young's modulus as a function of strain for the uniaxial case [19]

In order to organize the material data, a strain hardening model were suggested for both uniaxial and hydrostatic loading in compression as follows [19]:

$$\sigma = \sigma_p + \gamma \frac{\varepsilon}{\varepsilon_{\mathrm{D}}} + \alpha \, ln\left[\frac{1}{1-(\varepsilon/\varepsilon_{\mathrm{D}})^{\beta}}\right], \quad \varepsilon_{\mathrm{D}} = -\ln\left[\frac{\rho_f}{\rho_{f0}}\right]. \tag{7}$$

The first term represents the initial level of the plateau stress σ_p (uniaxial or hydrostatic) immediately after the elastic region is covered. This part is completely independent of true strain ε. The second term is a linear strain-hardening term and the slope of the stress-strain curve is represented by the linear strain-hardening coefficient γ. The last term represents non-linear strain hardening and is defined by the scale factor α and shape factor β. A key issue with this model is that the strain hardening is given as a function of the strain ε relative to the compaction strain ε_{D}. Note that the compaction strain is dependent on the relative density of the foam ρ_f/ρ_{f0} . The model has been calibrated to material tests and it is clearly seen from Fig. 13 that it accurately represents the measured stress-strain curves.

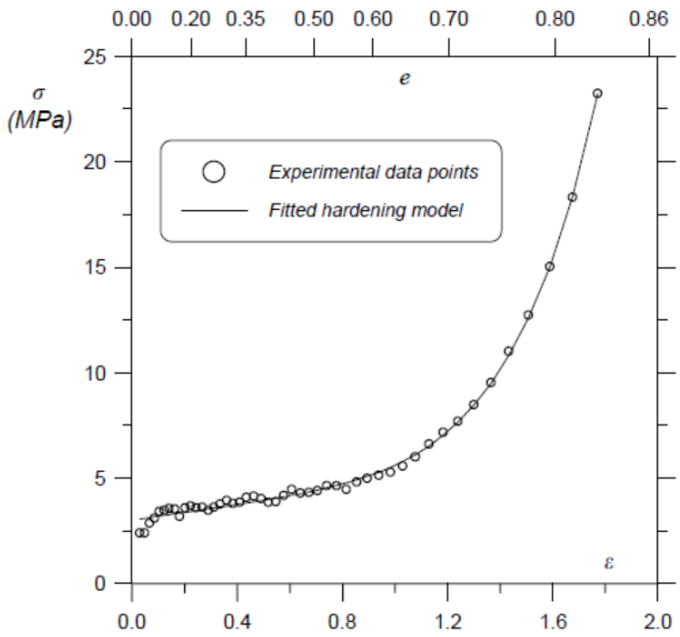

Fig. 13 Fit of calibrated strain-hardening model for the foam [19]

This model for strain-hardening together with the calibration data in [19] constitute a complete description of the strain-hardening properties of the aluminum foam.

In uniaxial tension, aluminum foam show sudden, brittle failure at a failure stress quite similar to the initial plateau stress in uniaxial compression. A correlation between the failure stress in tension σ_s and the initial plateau stress σ_p in compression is illustrated in Fig. 14. From this figure, it is possible to assume the tensile failure stress as $\sigma_s = \sigma_p$. The tests and calibrations have been done in [19].

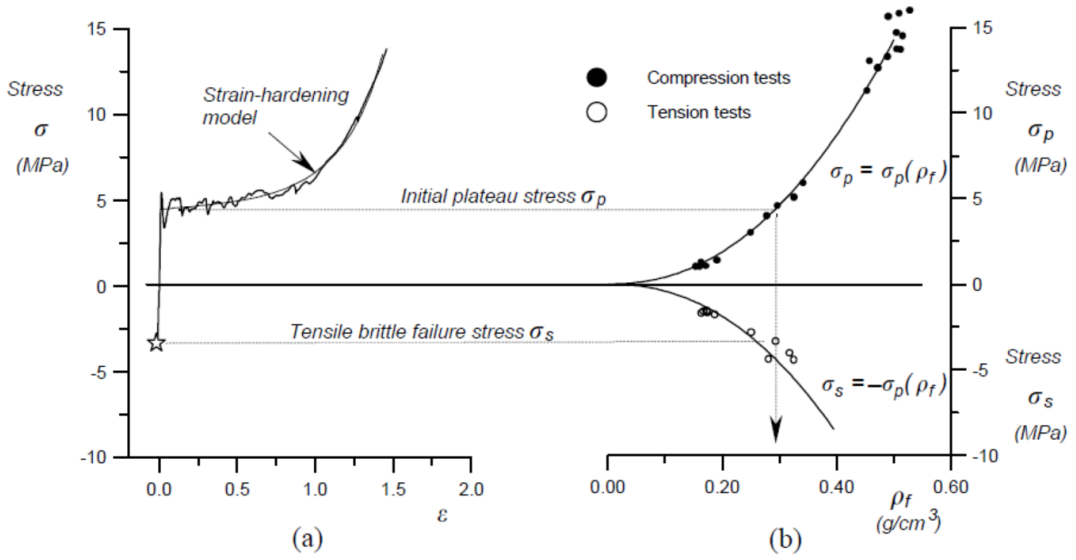

Fig. 14 Tensile properties of aluminum foam [19]

Strain-rate sensitivity

Blast loads on structures happens at high velocities and consequently the strain-rate gets high. The behavior of aluminum foams at high strain-rates must be determined in order to validate the use of stress-strain curves from quasi-static, uniaxial compression tests.

Deshpande and Fleck [21] investigated the high strain-rate compressive behavior of aluminum foams by using a Split-Hopkinson pressure bar (SHPB) and direct impact tests. The SHPB technique is a way of determining the stress versus strain behavior of materials at high strain rates. In shortness, the SHPB consists of a striker bar, incident pressure bar, transmitter pressure bar and a momentum trap. The specimen is subjected to an incident pressure pulse of approximately constant amplitude and of a duration proportional to the length of the striker bar. A more detailed description of the SHPB is given in [21].

Studies of the dynamic properties of cellular materials like wood and honeycombs have attributed the strength increase under dynamic loading conditions to micro-inertial effects and to shock wave propagation [21]. For dynamic loading, micro-inertial effects occurs when the collapse mode switches from the quasi-static mode to a new mode involving additional stretching that dissipates more energy. Structures have been divided in two classes, Type I and Type II, as in Fig. 15a. Type I structures have a quasi-static stress-strain curve as in Fig. 15b where the micro-inertial effects under high strain rates are neglected. Type II structures changes from a strongly softening bending mode of collapse into an initial phase of axial compression of the struts due to lateral inertia forces when loaded with rapid pressures [21].

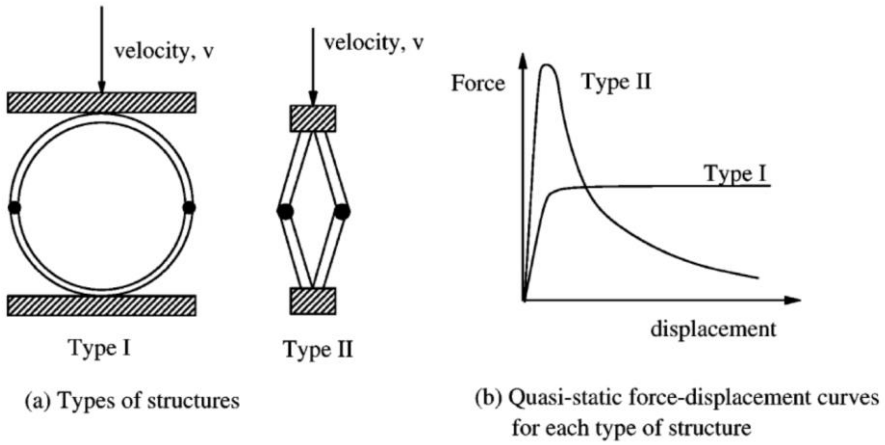

Fig. 15 Velocity-sensitive structures [21]

As a foam is subjected to loads at high velocity, a shock wave will propagate through the foam. In [21], a simple one-dimensional shock model is utilized to estimate the elevation of collapse stress due to the impact velocity. This one-dimensional shock model is based upon the assumption that the material exhibits a rigid-perfectly-plastic behavior in its uniaxial stress-strain response similar to a locking solid as in Fig. 16. The plateau stress, σ_p, and densification strain, ε_D, is demonstrated through this model.

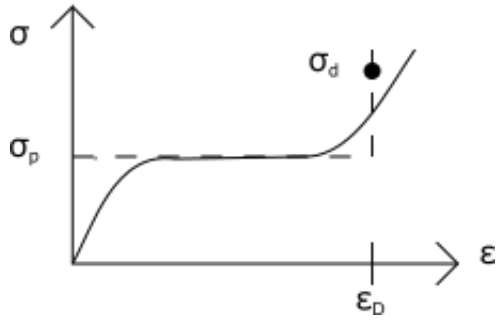

Fig. 16 Idealized stress-strain curve [21]

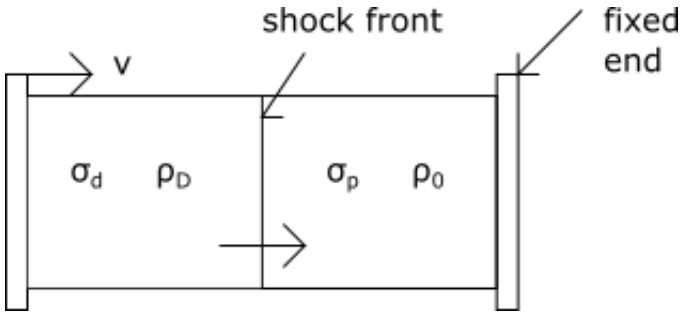

Fig. 17 Shock model parameters [21]

Fig. 17 illustrates the shock model parameters. Following Reid and Peng [22], an enhanced dynamic plateau stress σ_d is given by

$$\sigma_d = \sigma_p + \frac{\rho_0 v^2}{\varepsilon_D}. \tag{8}$$

When a shock wave moves through the material, the stress ahead of the shock wave equals σ_p. Behind the shock front moving with particle velocity *v*, the material has attained a densification strain and the density has increased from ρ_0 to ρ_D. The compressive stress has been raised to σ_d.

The behavior of different aluminum foams have been investigated with strain rates up to 5000 s^{-1} [21]. Fig. 18 illustrates quasi-static and dynamic stress-strain curves for various densities of aluminum foams.

The stresses have been normalized to remove the effect of relative density. The figure shows that there is no significant difference between the quasi-static and dynamic stress-strain curves. In addition, there is no change in the collapse mode for dynamic loading compared to the quasi-static mode. Thus, aluminum foam can be considered a rate-insensitive material for the purpose of this thesis and strain-rate effects are neglected because of this consideration.

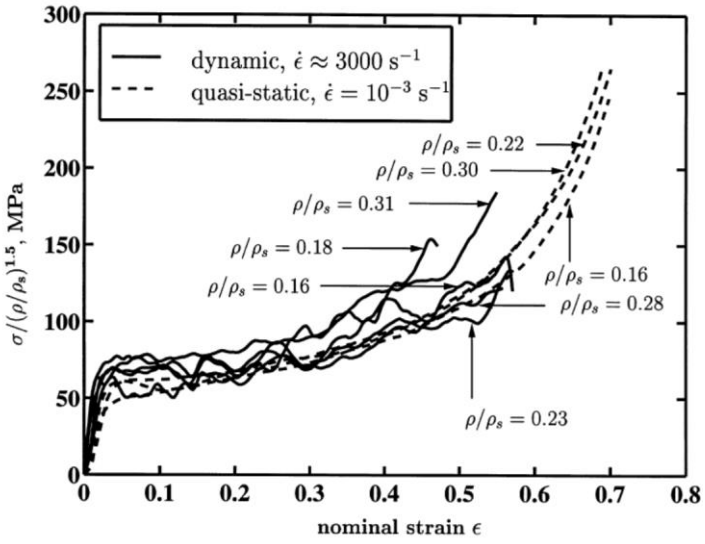

Fig. 18 Comparison between quasi-static and dynamic compressive stress-strain relationship [21]

Density sensitivity

The effect of the relative density of the aluminum foam core is important to consider as the portion of energy absorption by the core is increased by increasing the density of the foam [7]. It is well established that the density sensitivity of aluminum foams are quite large. Therefore, it is important to check the densities of all test specimens accurately in order to obtain the correct material data. Based on calibration tests performed in [19], the coefficients in eq. (7) were correlated with the foam density and a power-law description was applied to take into consideration the dependency on foam density.

$$\left\{\sigma_p, \alpha, \frac{1}{\beta}, \gamma, \right\} = C_0 + C_1 \left(\frac{\rho_f}{\rho_{f0}}\right)^n \tag{9}$$

The calibrated values C_0, C_1 and n are used to describe the material as density dependent.

Density variation

The foam sheets used in this thesis have a variety in the density along the z-direction. The presence of gravity during the continuous casting process gives rise to this effect. A closer look at cell shapes and sizes gives an explanation to the phenomenon. When the cell shape is regarded from the *xy*-plane, the distribution is uniform along both x- and y-direction, but both planes including the z-direction revealed a gradient in cell shape along the z-axis. The cells near the bottom of the manufactured foam sheet is elongated in x- and y-direction compared to the z-direction. Hence, the liquid aluminum has been pushed to the bottom of the sheet by gravity during the casting process and creating a non-uniform density along the z-axis [19].

2.1.3 Constitutive models for aluminum foams

A lot of research has been done in the recent years in order to describe the behavior of aluminum foams. Three material models applicable to aluminum foams are described further.

Miller [23] proposed a yield surface that describes a wide range of materials that exhibits pressure-dependent yield and a large change in volume. Three adjustable parameters are used to fit the model to simple tests without the need of detailed knowledge of the shape of the yield surface. The compaction hardening is taken from the volumetric strain, while the strain hardening of the base material depends on the accumulated plastic strain. Together, these functions are able to represent the stress-strain relationship from a uniaxial compression test. The final set of formulas are quite simple and after uniaxial compression and tension stress-strain responses have been determined from experiments, the calibration of the constitutive model is easily done.

The model proposed by Schreyer et al. [24] is a three-dimensional anisotropic plasticity model. A simple shift in the principal stress space is used to represent the anisotropy of the material and volumetric strain is used as a tool to indicate the initiation of lockup. Initial kinematic hardening is introduced in the yield criterion and a sphere is generated in the principal stress space. A diagonal tensor represents the initial kinematic hardening and for a given reference system, the three diagonal terms are constant during loading and further kinematic hardening is not taken into account. Isotropic hardening as a function of the plastic volumetric strain is considered. No hardening takes place in the plateau region; hence, it is only when the plastic volumetric strain reaches a critical value dependent on the foam density, that hardening starts.

The model proposed by Deshpande and Fleck [25] is a direct extension of the von Mises yield criterion. While the classic yield criterion for isotropic mechanical behavior states that yielding occurs when the elastic shear energy reaches a critical value, the experiments done in [19] clearly indicates that metal foams exhibit plastic flow for pure hydrostatic stress. Therefore, it is necessary to extend the von Mises yield criterion to take into account that the elastic volumetric energy affects the plastic flow of foams.

First, it is assumed that the elastic region of a metallic foam can be described by Young's modulus *E* and Poisson's ratio *v* as for an isotropic solid material. It is further assumed that the yield function Φ depends only on the first two stress invariants σ_m and σ_e. The yield function is defined as

$$\Phi \equiv \hat{\sigma} - Y \leq 0 \tag{10}$$

where the equivalent stress $\hat{\sigma}$ is defined as

$$\hat{\sigma}^2 \equiv \frac{1}{(1 + (\alpha/3)^2)} [\sigma_e^2 + \alpha^2 \sigma_m^2]. \tag{11}$$

Here, σ_e is the von Mises effective stress $\sigma_e \equiv \sqrt{\frac{3}{2}\sigma'_{ij}\sigma'_{ij}}$, σ_m is the mean stress $\sigma_m \equiv \sigma_{kk}/3$ and α is a parameter defining the shape of the yield surface. The prime denotes the deviatoric quantity. Together, eq. (10) and eq. (11) describes an elliptic yield surface in the (σ_m, σ_e) space, with a uniaxial yield strength Y in tension or compression, and a hydrostatic yield strength

$$|\sigma_m| = \frac{\sqrt{(1+(\alpha/3)^2)}}{\alpha} Y. \tag{12}$$

In the limit $\alpha = 0$, $\hat{\sigma}$ is reduced to σ_e and the von Mises yield criterion is recovered. The plastic Poisson's ratio v^p in a uniaxial compression test can be derived from eq. (10) and eq. (11) and written explicitly in terms of the pressure-sensitivity coefficient α as

$$v^P = -\frac{\dot{\epsilon}^P_{11}}{\dot{\epsilon}^P_{33}} = \frac{(1/2)-(\alpha/3)^2}{1+(\alpha/3)^2}. \tag{13}$$

The inverse relation becomes

$$\alpha = 3\left(\frac{(1/2)-v^p}{1+v^p}\right)^{1/2}. \tag{14}$$

In the case of isotropic hardening, the yield surface is assumed to evolve in a geometrically self-similar manner under uniaxial loading. By utilizing the consistency relation for continued plastic flow and the flow rule, the plastic strain rate is obtain as

$$\dot{\varepsilon}^P_{ij} = \dot{\hat{\varepsilon}} \frac{\partial \Phi}{\partial \sigma_{ij}} \tag{15}$$

Where the introduced equivalent strain rate $\dot{\hat{\varepsilon}}$ is the plastic work conjugate to $\hat{\sigma}$,

$$\hat{\sigma}\dot{\hat{\varepsilon}} = \sigma_{ij}\dot{\varepsilon}^P_{ij}. \tag{16}$$

By using the fact that the yield function is homogeneous of degree one in $\boldsymbol{\sigma}$ and substituting eq. (15) into eq. (16), the von Mises effective plastic strain rate $\dot{\epsilon}_e$ and the volumetric plastic strain rate $\dot{\epsilon}_m$ can be expressed as

$$\dot{\epsilon}_e \equiv \sqrt{\frac{2}{3}\dot{\epsilon}'^P_{ij}\dot{\epsilon}'^P_{ij}} = \frac{\dot{\hat{\varepsilon}}}{(1+(\alpha/3)^2)}\frac{\sigma_e}{\hat{\sigma}}, \tag{17}$$

and

$$\dot{\epsilon}_m \equiv \dot{\epsilon}^P_{kk} = \frac{\alpha^2\dot{\hat{\varepsilon}}}{(1+(\alpha/3)^2)}\frac{\sigma_m}{\hat{\sigma}}. \tag{18}$$

By substituting expressions for σ_e and σ_m into eq. (11) and simplifying, an explicit expression for the equivalent strain rate $\dot{\hat{\varepsilon}}$ is obtained as

$$\dot{\hat{\varepsilon}}^2 = \left[1+\left(\frac{\alpha}{3}\right)^2\right]\left(\dot{\epsilon}_e^2 + \frac{1}{\alpha^2}\dot{\epsilon}_m^2\right). \tag{19}$$

The model proposed by Deshpande and Fleck [25] is the model implemented in Abaqus for the crushable foam plasticity model. It is also the model implemented in LS-DYNA by Reyes et al. [26]. The simplicity of this model in terms of its isotropic hardening model and the fact that only uniaxial compression tests is needed to describe the hardening curve makes it the preferred model to describe the foam material.

2.2 Blast loading

2.2.1 Introduction

The theory of blast loading design will be presented here and later the blast loading effects will be compared with the loading effects from the shock tube to validate it as a tool for simulating pressure loads from explosions.

Baker [27] defines an explosion in air as energy released over a sufficiently small time and in a sufficiently small volume that generates a pressure wave of finite amplitude traveling away from its source. Further, Bjerketvedt et al. [28] describes an explosion as an event leading to a rapid increase of pressure. Sources of this increased pressure can be nuclear reactions, loss of containment in high-pressure vessels, high explosives and several other sources.

Most blast load problems can be divided into four phases according to Børvik et al. [29]:

1. The detonation phase - An exploding source produces high-pressure gases propagating outwards as pressure waves through its surrounding medium
2. The propagation phase - Blast waves of high intensity propagates and moves towards a target
3. The interaction phase - The blast wave interacts with the target
4. The response phase - The response of the target due to interaction with the blast wave

2.2.2 Blast wave properties

Principal blast waves

When an explosion occurs, a blast wave develops and propagates out from the source. The blast wave will interact with, and apply impulsive load on a structure. As this happens, rapid variations in pressure, density, temperature and velocity will occur. Blast wave properties are related to measurable observations such as the shock front arrival time, velocities and time histories of overpressures. Density variations and time histories of particle velocities are more difficult to measure, but they also influence the blast wave properties [27].

General blast waves include sonic compression waves, shock waves and rarefaction waves. Fig. 19 graphically describes three different types of blast waves.

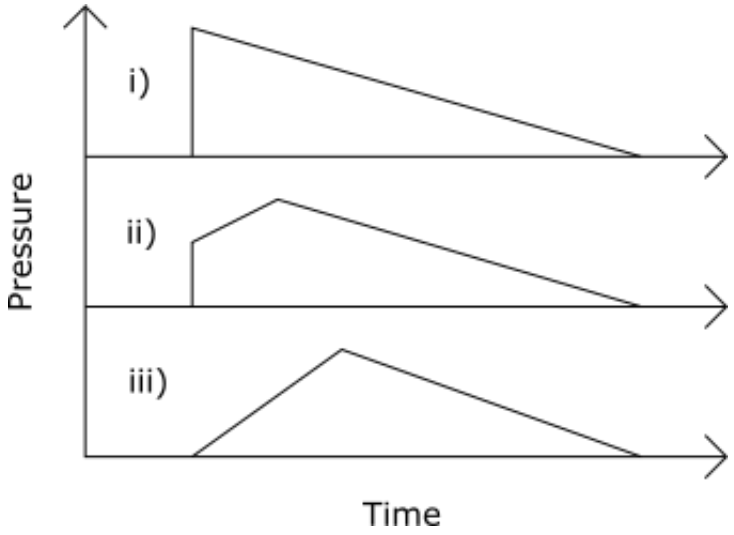

Fig. 19 Principal blast waves [28]

(i) A shock wave followed by a rarefaction wave
(ii) A shock wave followed by a sonic compression wave and then a rarefaction wave
(iii) A sonic compression wave and rarefaction wave

There are primarily two important factors regarding what type of wave that is created from an explosion. Those are the distance from the explosive source and how the energy is released from the explosive. Category (i) waves are typical for detonations and category (iii) waves emerges from a combustion wave moving at a slower speed than that for detonations. This type of wave is called a deflagration. A detonation is defined as a combustion wave moving at supersonic speed relative to the unburnt gas ahead of the flame. A detonation is typically initiated from a high explosive charge, but it can also occur if a deflagration accelerates due to obstacles or confinement. A deflagration is typically what happens if an accidental gas explosion occurs. For strong deflagrations, a shock wave may propagate ahead of the deflagration.

Idealized blast wave

The properties that are usually defined and measured in a blast wave are those of the undisturbed side-on wave as it propagates through air. A graphic representation of a typical ideal blast wave is shown in Fig. 20.

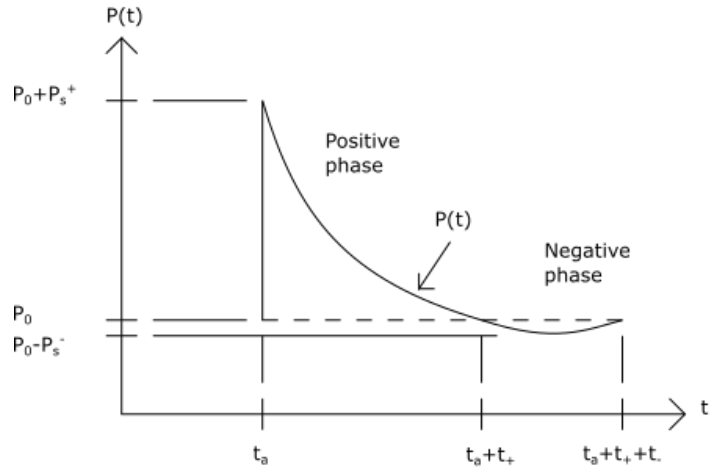

Fig. 20 Typical ideal blast wave

Before the arrival of the shock front, the ambient pressure P_0 is present. When the shock front arrives at t_a, the pressure will rise discontinously in an ideal wave to a peak on-side overpressure P_s. The pressure will then decay to P_0 after the positive phase t_+ has passed, and the negative phase t_- is initiated. The pressure will then return to ambient pressure after a short while.

Pressure

The specific impulses for the positive and negative phases are defined as the area under the blast wave curve

$$i_s^+ = \int_{t_a}^{t_a+t_+} [P(t) - P_0]\, dt \tag{20}$$

and

$$i_s^- = \int_{t_a+t_+}^{t_a+t_++t_-} [P_0 - P(t)]\, dt. \tag{21}$$

When considering blast load effects on structures, the negative phase of the blast wave is normally neglected and only the blast parameters associated with the positive phase are considered. The ideal side-on wave parameters rarely describes the actual pressure loading applied to a structure after an explosion. Therefore, other properties such as reflection must be taken into account in order to get a more accurate approximation of the real blast loading [27].

In fluid dynamic problems, different types of pressures are often referred to. Those are static pressure, dynamic pressure and stagnation pressure. The static pressure is often referred to as the atmospheric pressure present at the blast site and are generally defined as the pressure that

exists in a medium when no sound waves are present. The dynamic pressure can be expressed as

$$P_{Dyn} = \frac{\rho \cdot u^2}{2} \tag{22}$$

where ρ is the density of the medium and u is the flow velocity. Dynamic pressure is defined as the pressure increase that a moving fluid would have if it was brought to rest by isentropic flow against a pressure gradient [28].

The stagnation pressure is the sum of the static pressure and dynamic pressure, i.e.

$$P_{Stag} = P_{Sta} + P_{Dyn} \tag{23}$$

Scaling of the blast wave properties from an explosion is common practice and the most common form of blast scaling is by Hopkinson-Cranz scaling law. The law states that self-similar blast waves are produced at identical scaled distances when two explosive charges of similar geometry and the same explosive, but different sizes, are detonated in the same atmosphere. The scaled distance, Z, is defined as

$$Z = \frac{R}{W^{1/3}} \tag{24}$$

where R is the stand-off distance and W is the equivalent mass of TNT.

The side-on pressure is not always enough to describe the pressure loading from an explosion. For blast waves and shock waves, a reflected pressure is also present. The side-on pressure P_s is measured perpendicular to the propagation direction of the wave, while the reflected pressure P_r is measured when a blast wave hits an object like a wall head-on. The definitions of side-on and reflected pressure are shown in Fig. 21.

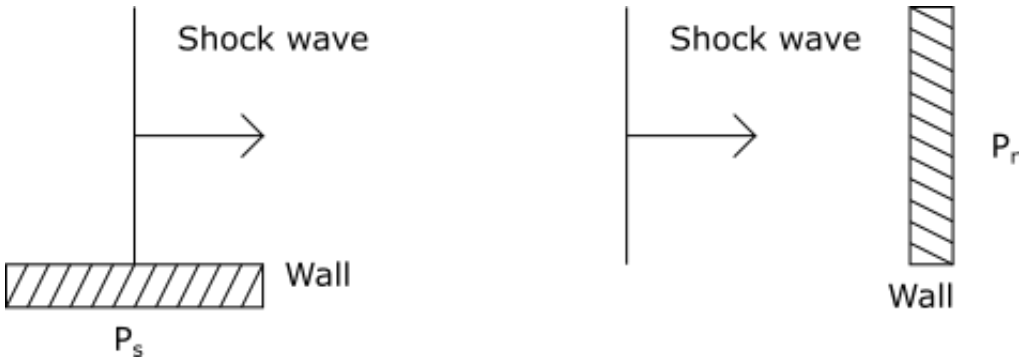

Fig. 21 Illustration of side-on and reflected pressures [30]

An upper limit for the blast load is achieved by putting an infinite rigid wall in front of the shock wave and reflecting the wave normally. This is the reflected overpressure and is defined equally as the side-on overpressure. The Hopkinson-Cranz scaling law applies to both side-on and reflected blast wave parameters. For explosives other than bare spheres of solid high explosives, very little data exists of normally reflected overpressures and specific impulses.

For shock waves weak enough so that ideal gas theory can be applied, there is a well-known relation between the peak reflected overpressure and the side-on overpressure [27]:

$$\bar{P}_r = 2\bar{P}_s + \frac{(\gamma_1 + 1)\bar{P}_s^2}{(\gamma_1 - 1)\bar{P}_s + 2\gamma_1}. \tag{25}$$

Here, $\bar{P}_r = P_r/P_0$ and $\bar{P}_s = P_s/P_0$ and γ_1 is the ratio of heat capacity at constant pressure and the heat capacity at constant volume. At low incident overpressures, the reflected overpressure approaches the acoustic limit of twice the incident overpressure. If one assumes $\gamma_1 = 1.4$ for air, the upper limit for the peak reflected overpressure would appear to be $\bar{P}_r = 8\bar{P}_s$.

The peak reflected overpressure is the most important property of the blast wave because it describes the maximum pressure that the structure subjected to a blast wave experiences. It is important to note that the peak reflected overpressure represent an upper limit where the blast wave hits an infinitely stiff structure head-on. If the blast wave hits the structure at an angle, the structure is not infinitely stiff or a deformation occurs in the structure, the reflected pressure will be between the reflected and side-on peak overpressures.

In order to describe the ideal blast wave curve as seen in Fig. 20, a simple exponential equation is fitted to the measured ideal blast wave. This equation is as follows:

$$P(t) = P_0 + P_r\left(1 - \frac{t}{t_+}\right)exp\left(\frac{-bt}{t_+}\right) \tag{26}$$

and is called the Friedlander equation. Here, the decay coefficient b is determined from iteration using the peak reflected overpressure P_r, reflected impulse I_r and the duration of the positive phase t_+. This equation will be fitted to measured pressures from the shock tube experiments in order to apply similar loading in the numerical analyses as in the shock tube experiments.

2.2.3 Blast load design

Prediction of design blast loads on structures can be done in several ways. There exists three common design methods: the empirical, semi-empirical and computational fluid dynamics (CFD). In general, the most usual methods are the empirical and CFD. It should also be decided whether a coupled or uncoupled method should be used. Fig. 22 illustrates some considerations regarding blast load design on structures.

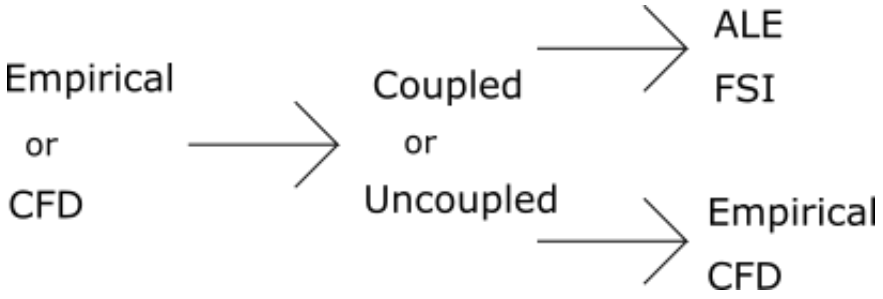

Fig. 22 Considerations regarding blast load design

A coupled method means that the loading is coupled with the structure, but in the case of uncoupled methods, the loading is independent of the structure itself. For coupled methods, an arbitrary Lagrangian-Eulerian (ALE) approach or Fluid-Structure Interaction (FSI) effects should be considered. In the uncoupled case, the empirical method or CFD is used.

Empirical method
The simplest and most common method for quick assessments of blast loads is the empirical method. Kingery and Bulmash [31] analyzed data from controlled explosions in the range of 1 kg to 400 000 kg TNT. By fitting the data with higher order polynomials, they produced a wide range of graphical data on blast load characteristics. The Hopkinson-Cranz scaling law is used and the empirical method is based on these correlations. The blast parameters from a free field spherical TNT explosion can be determined from the figure in Appendix A. For a given peak reflected overpressure, the equivalent mass TNT can be derived when a stand-off distance is specified.

Computational fluid dynamics (CFD)
The empirical method is only valid for simple geometries and involve quite many assumptions. Blast wave propagation is very often a complex process that creates high-pressure gradients. Empirical methods are not capable of taking care of confinements and are weak for small and large distances. CFD, on the other hand, is capable of taking care of complex geometries and confinement is included by the construction. Therefore, CFD is the preferred numerical tool when analyzing explosions inside confined volumes as a submerged floating tunnel.

The CFD-code EUROPLEXUS is a computer program which can perform finite element simulations of FSI problems under dynamic loading. The scope of this thesis, however, is only to investigate the behavior of aluminum foam under blast loading, so a complicated tool as CFD is not necessary for this purpose. But if a global analysis of the submerged floating tunnel were to be investigated, a CFD analysis would have been performed [32].

2.2.4 Blast load propagation in tunnels
If an explosion happens inside a submerged floating tunnel, it is considered an internal explosion because it happens in a closed environment and it is important to know how the blast wave will propagate inside the tunnel.

In [28], the propagation of flammable gases in pipes, channels and tunnels are discussed. If a flame inside a pipe generates a pressure, it is possible that it will propagate away from the combustion front. For long or open-ended pipes, high explosion pressure is only generated if the flame speed is high. When gas burns, it will expand, and push the unburnt gas ahead of the flame front. The flow ahead of the flame will cause a turbulence that will enhance the rate of burning. The main mechanism for accelerating a flame in pipes is turbulence.

The flame may continue to accelerate inside the pipe until it becomes a detonation, but there does not exist a qualitative understanding of the mechanism of transition to detonation. High local pressures characterize the transition to detonation. When transition to detonation has

occurred, pressures of 50 times the initial pressure have been measured and very strong damage were observed at the location of the transition to detonation. Therefore, it is important to recognize that transition to detonation in pipes, channels and tunnels could possibly be an extremely hazardous phenomenon and could be initiated by an accident like a car crash inside the tunnel.

2.3 Computational method

A suitable method for computing blast loading effects on structures is by the finite element code Abaqus/Explicit. Some of the theory used for the numerical analyses are described in this chapter. Mainly, the theory of explicit dynamic analysis is presented and its advantages compared to an implicit method are discussed in some extent.

2.3.1 Explicit dynamic analysis

In Abaqus/Explicit, the central-difference explicit integration rule is applied to solve the equation of motion numerically. The dynamic equilibrium of a Multi Degree of Freedom (MDOF) system is considered at time t_n to calculate the displacements at the next time-step t_{n+1}. Lumped mass is used to obtain a diagonal mass matrix that is constant in time. At time step n the conventional central difference equations is used to approximate velocity $\{\dot{\boldsymbol{D}}\}_n$ and acceleration $\{\ddot{\boldsymbol{D}}\}_n$ as [33]

$$\{\dot{\boldsymbol{D}}\}_n = \frac{1}{2\Delta t}(\{\boldsymbol{D}\}_{n+1} - \{\boldsymbol{D}\}_{n-1}) \tag{27}$$

$$\{\ddot{\boldsymbol{D}}\}_n = \frac{1}{\Delta t^2}(\{\boldsymbol{D}\}_{n+1} - 2\{\boldsymbol{D}\}_n + \{\boldsymbol{D}\}_{n-1}) \tag{28}$$

However, Abaqus/Explicit uses half-step central differences were the velocity is lagging half a time step behind displacements and accelerations. The half-step method uses the equations

$$\{\boldsymbol{D}\}_{n+1} = \{\boldsymbol{D}\}_n + \Delta t\{\dot{\boldsymbol{D}}\}_{n+1/2} \tag{29}$$

$$\{\dot{\boldsymbol{D}}\}_{n+1/2} = \{\dot{\boldsymbol{D}}\}_{n-1/2} + \Delta t\{\ddot{\boldsymbol{D}}\}_n \tag{30}$$

$$[\boldsymbol{M}]\{\ddot{\boldsymbol{D}}\}_n + [\boldsymbol{C}]\{\dot{\boldsymbol{D}}\}_{n-1/2} + \{\boldsymbol{R^{int}}\}_n = \{\boldsymbol{R^{ext}}\}_n \tag{31}$$

Combinations of equations (29), (30) and (31) gives the following expression for $\{\boldsymbol{D}\}_{n+1}$

$$\frac{1}{\Delta t^2}[\boldsymbol{M}]\{\boldsymbol{D}\}_{n+1} = \{\boldsymbol{R^{ext}}\}_n - \{\boldsymbol{R^{int}}\}_n + \frac{1}{\Delta t^2}[\boldsymbol{M}]\left(\{\boldsymbol{D}\}_n + \Delta t\{\dot{\boldsymbol{D}}\}_{n-1/2}\right) - [\boldsymbol{C}]\{\dot{\boldsymbol{D}}\}_{n-1/2} \tag{32}$$

In these equations, $[\boldsymbol{M}]$ is the mass matrix, $[\boldsymbol{C}]$ is the damping matrix, $\{\boldsymbol{R^{int}}\}_n$ is the internal forces including the stiffness of the structure and $\{\boldsymbol{R^{ext}}\}_n$ represents the external forces on the structure.

This method can only guarantee first-order accuracy due to the velocity lagging behind half a time-step, but the same accuracy is obtained compared to the conventional difference method when structures have light damping and require small time steps.

Explicit integration methods are conditionally stable and requires the time step to be smaller than a specified critical value. The critical time increment, Δt_{cr}, required is related to the highest eigenfrequency, ω_{max}, of the system

$$\Delta t \leq \frac{2}{\omega_{max}} = \Delta t_{cr}. \tag{33}$$

The physical interpretation of the stable time increment is that it must be small enough so that information does not propagate more than the distance between adjacent nodes during a single time step. This means that the stable time increment becomes the minimum time it takes for a dilatational wave to travel across any element in the finite element (FE) model. The smallest element in the FE mesh will thus be decisive:

$$\Delta t_{cr} = \frac{L^e}{c_d} \tag{34}$$

where $c_d = \sqrt{E/\rho}$ is the dilatational wave speed or speed of sound in the material and L^e is the characteristic length of the smallest element in the FE mesh.

In order to check the accuracy of a dynamic explicit analysis some considerations should be done regarding the energy outputs. First, the total energy (ETOTAL) should be approximately a constant value. Then, the ''artificial'' energies such as the artificial strain energy (ALLAE), the damping (viscous) dissipation (ALLVD), and the mass scaling work (ALLMW) should be much smaller than ''real'' energies such as the strain energy (ALLSE) and the kinetic energy (ALLKE). It is also good practice to output the constraint penalty work (ALLCW) and the contact penalty work (ALLPW) in analyses involving constraints and contacts [34].

An explicit dynamic analysis is preferred to an implicit method on wave propagation problems where small time increments are required. Each time increment is also calculated with ease due to the absence of equation solving and equilibrium iterations. The main disadvantage is the time increment, which must be small enough. The method is reliable for problems that involve contact, buckling, material failure and other discontinuous nonlinearities. An implicit method requires equation solving at each time step and convergence is an important issue to consider. Though an implicit method is unconditionally stable and is not limited by a critical increment size, the method works best for problems involving long response periods and smooth nonlinearities [35].

When analyzing a structure subjected to impulsive loading from blast events, the time period considered is quite small and requires small time steps to obtain an accurate solution. In addition, to predict failure in the analysis, an explicit method must be used. The explicit integration method is therefore the main method when it comes to this type of problem and will be used here.

2.3.2 Lagrangian approach

In this thesis, the Lagrangian approach is used in the FE simulations. For this type of formulation, the physical quantities are expressed as functions of time and their initial position in a fixed global, Cartesian coordinate system. The nodes are always at the same material point and boundaries will follow element edges as they deform. Lagrangian meshes are widely used in solid mechanics because constitutive equations are evaluated at the same material point during the analysis. A disadvantage of using Lagrangian formulation is that it is not good at handling very large deformations. For cases involving severe distortions of elements, an Eulerian approach should be used.

2.4 Shock tube

2.4.1 The SIMLab Shock Tube Facility (SSTF)

The SIMLab Shock Tube Facility (SSTF) consists of a tube with an internal square cross-section of 0.3 × 0.3 m. In total, the tube has a length of 18.275 m while the overall length of the facility is 20.5 m. At the end of the tube, a 5.1 m^2 tank enables an expansion in volume to decrease the overall pressure in the facility after testing. The facility consists of six parts and is described by Aune et al. [36].

At the initial end of the tube, the driver section is located. This chamber was manufactured with a full length of 2.02 m and internal diameter 0.331 m, but the volume can be modified depending on the desired pressure of the experiment. First, the driver section is filled with compressed air in controlled conditions. The driver section is separated from the driven section by diaphragms. This is called the firing section in Fig. 23 and a picture of the firing section is shown in Fig. 24.

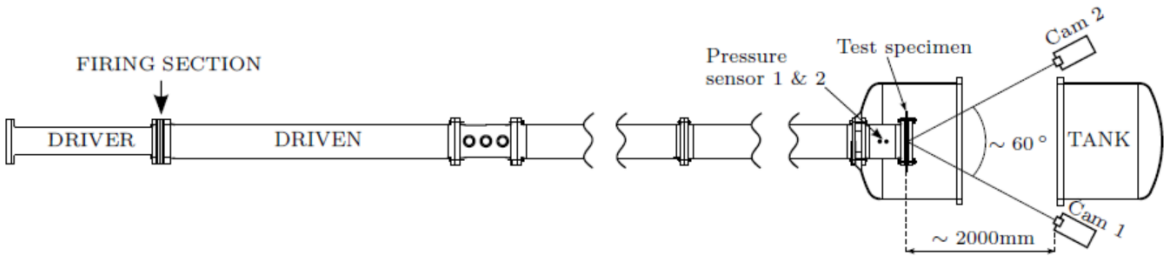

Fig. 23 Overview of the shock tube [36]

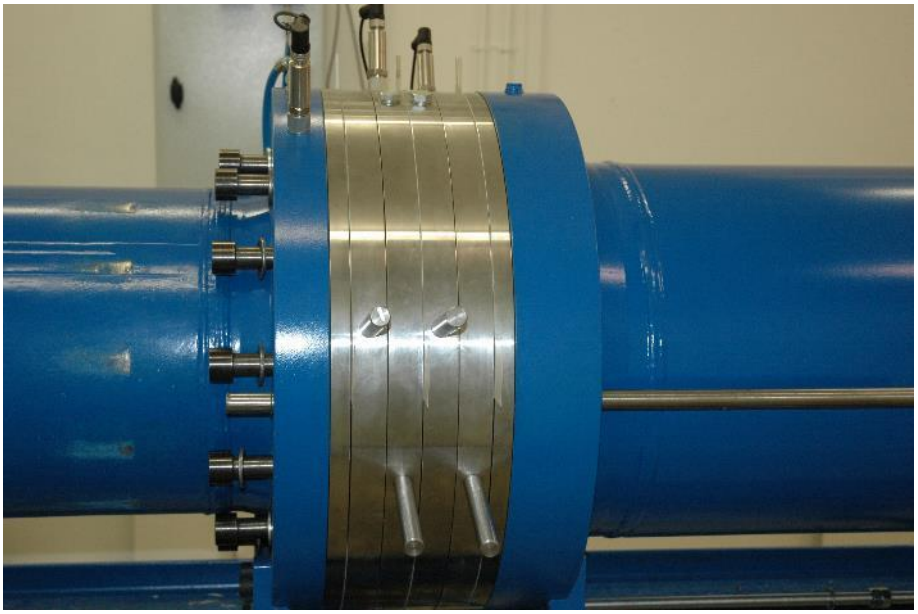

Fig. 24 The firing section

The firing section consists of several intermediate pressure chambers to enable a stepwise increase in the driver gas pressure. When the diaphragms experience rupture, the driver gas will expand into the driven section and generate a shock wave of high intensity towards the test specimen at the far end.

The pressures can be measured at 20 different places downstream the tube, but the pressure sensors closest to the test specimen are the most important. These sensors are called pressure sensor 1 and 2 in Fig. 23 and a picture of the sensors are shown in Fig. 25. Two high-speed cameras are able to measure the response of the test specimen. Fig. 26 shows an example of a test specimen mounted in the shock tube from the view behind camera 1.

Fig. 25 Pressure sensors closest to the test specimen

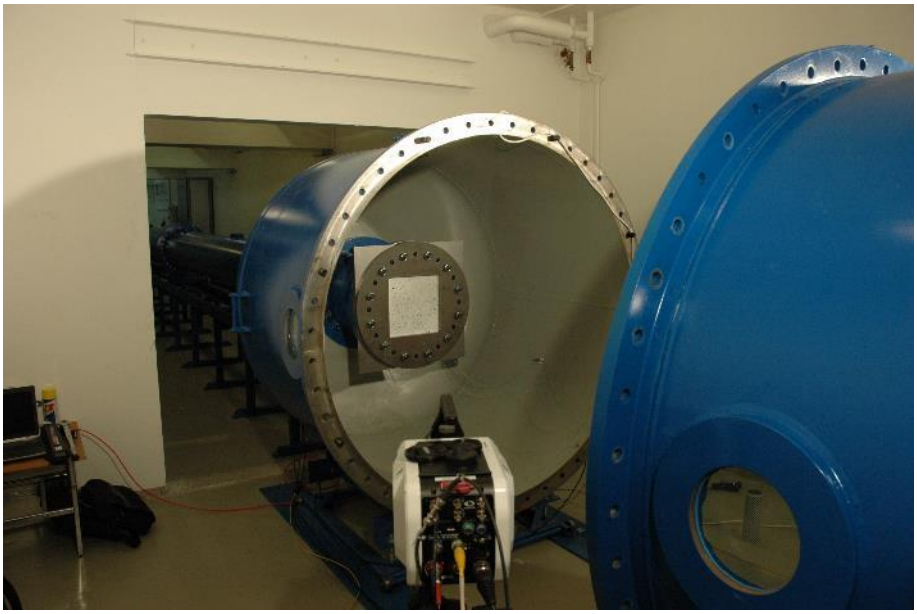

Fig. 26 View of the test specimen from behind camera 1

2.4.2 Shock wave theory

Assumptions

The theory presented for the shock wave produced by the shock tube is only valid when introducing some assumptions that makes ideal gas theory applicable. Some of these effects have been investigated and discussed by Brun [37].

In [37], two effects are discussed concerning disturbing effects on the shock wave. One of these effects are that the opening of the diaphragm will not happen instantaneously and this may influence the shock wave shape, but the effect is likely to decrease with distance from the firing section. This effect was investigated in [37] for different diaphragm materials. It was noted that as long as the diaphragm opens in a relatively short time, the shape of the shock wave should be independent of how it was formed.

The most significant effect according to [37], however, is related to the disturbance due to the presence of a wall boundary layer. The shock wave reaches a maximum velocity and then decelerate so non-uniform gas properties will occur. This is because gas entering a weaker shock is compressed and less heated. In addition, attenuation of the shock wave is caused by loss of energy from the driver gas to the boundary layer.

Ideal gas theory

The ideal gas theory is based on a special case of Navier-Stokes equations. By applying the conservation laws with respect to mass, momentum and energy, the following expressions are obtained [38].

$$\rho_1 v_1 = \rho_2 v_2 \tag{35}$$

$$\rho_1 v_1^1 + P_1 = \rho_2 v_2^2 + P_2 \tag{36}$$

$$h_1 + \frac{v_1^2}{2} = h_2 + \frac{v_2^2}{2} \tag{37}$$

Here, ρ is the density of the gas, v is the velocity, P is the pressure and h is the enthalpy of the gas. Index 1 refers to the initial driver gas and index 2 refers to the gas behind the incident shock wave. These equations are transformed into the shock tube coordinate system by applying two relations. The first one is that the velocity of the initial driver gas v_1 equals the velocity of the shock wave U_S. The second is that the velocity of the gas behind the incident shock wave v_2 equals the difference between the velocity of the shock wave, U_S, and the velocity of the gas particles behind the shock wave U_2.

Now, the thermodynamic properties of the gas behind the shock wave are expressed as functions of the shock wave velocity since this is a readily measured quantity. By utilizing the equation of state for a perfect gas, the incident overpressure p_2 is calculated from p_1, γ_1 (the ratio of specific heat at constant pressure to that at constant volume for the driven gas), and the Mach number M_S of the advancing shock wave [38, 39]:

$$p_2 = p_1\left(1 + \frac{2\gamma_1}{\gamma_1 + 1}(M_S^2 - 1)\right) \tag{38}$$

The Mach number, M_S, is defined as the ratio of the speed of the shock wave, U_S, to the speed of sound, $a_1 = \sqrt{\gamma_1 R T_1/m_1}$, in the undisturbed gas. T_1 is the initial temperature of the driven gas, m_1 is its molecular weight and R is the gas constant. Two pressure sensors with known distance between them are used to calculate the speed of the shock wave by measuring the time that the wave passes. The following expression is taken from [39] for the pressure ratio across the diaphragm in the tube where the driver and driven section areas are constant:

$$\frac{p_4}{p_1} = \frac{1}{\alpha_1}\left(\frac{2\gamma_1 M_S^2}{\gamma_1 - 1} - 1\right)\left(1 - \frac{(1/\alpha_4)(a_1/a_4)(M_S^2 - 1)}{M_S}\right)^{-2\gamma_4/(\gamma_4 - 1)} \tag{39}$$

where p_1 is the initial pressure in the driven section and p_4 is the initial pressure in the driver section before the shock wave has been fired.

After the shock wave is released, an expression for the peak reflected overpressure p_r can be obtained from p_1, p_2 and $\alpha_1 = (\gamma_1 + 1)(\gamma_1 - 1)$ as follows:

$$p_r = p_2\left(\frac{(\alpha_1 + 2)(p_2/p_1) - 1}{(p_2/p_1) + \alpha_1}\right) \tag{40}$$

More information regarding validation and analysis of the SSTF as a tool for describing a pressure wave from air-blast explosions are given in [36] and [39].

2.5 Digital Image Correlation (DIC)

Digital Image Correlation (DIC) is a technique used to obtain outputs from mechanical experiments. A series of digital images is utilized and points in a random pattern on the test specimen is tracked. A computer program is used to create a mesh on the random pattern that

enable us to follow it through the experiment. Displacements in and out of plane and strain fields may be measured. Due to better computational hardware and camera technology in the last decade, DIC has become a well-established tool for measuring strains and displacements from mechanical tests.

In this thesis, DIC is used as the tool for measuring output in the shock tube experiments and the uniaxial compression tests of aluminum foam. A detailed description of how DIC works is not given because it is not the main topic of this thesis. More details about DIC is found in the work done by Fagerholt [40].

3 Calibration of pressure in the shock tube

It was necessary to conduct calibration tests in the shock tube to achieve correct information about the pressure-time histories and the actual incident and peak reflected overpressures at the test specimens. For obvious reasons, there will be no sensors at the plates when testing, so a relationship between sensors closest to the end and the calibration plate is needed. Tests were performed with pressures in the range of 5-40 bar in the driver section and ten sensors were mounted as in Fig. 27 and Fig. 28 that should measure uniform values. To obtain the wanted pressures in the driver section, different configurations of diaphragms were used. The different configurations are tabulated and can be seen in Appendix B.

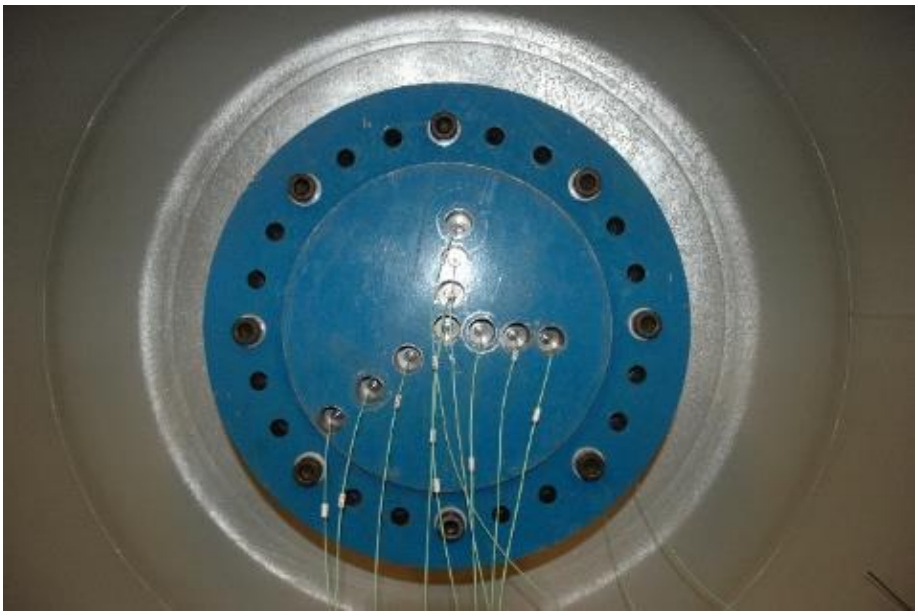

Fig. 27 Sensors for calibration of pressures in the shock tube

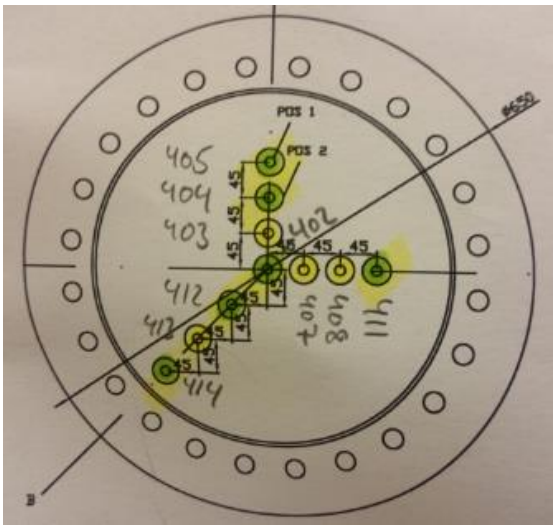

Fig. 28 Sensors with numbering for calibration

In the driver section, the pressure was increased in steps. The first chamber was filled with pressure before the other chambers were filled gradually so that the difference in pressures between chambers did not exceed the diaphragm capacities. An illustration of pressures in the different chambers are shown in Fig. 29.

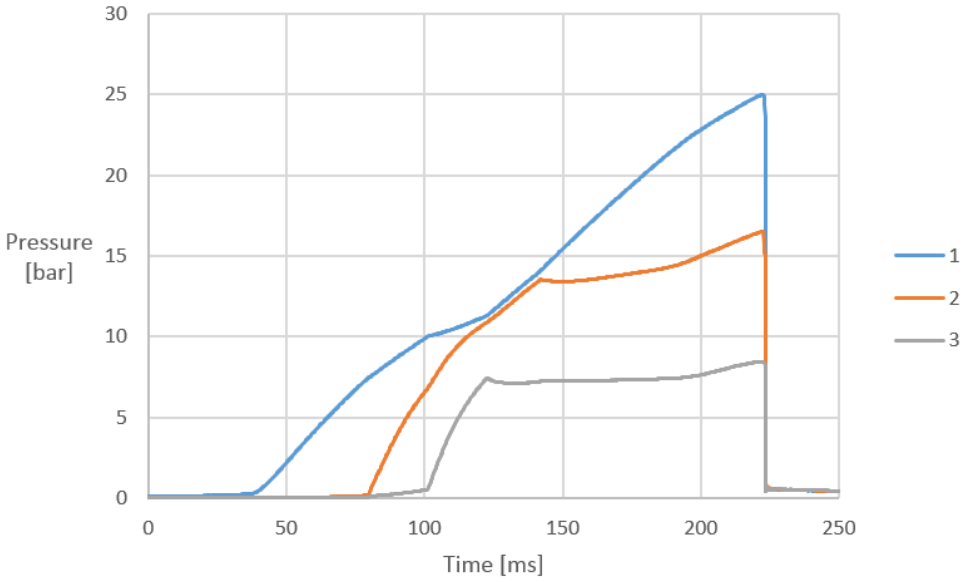

Fig. 29 Pressure build-up in the driver section before releasing the shock wave

Here, the first chamber is called ''1'' and the pressure starts building at time t=40 ms. Chamber ''2'' in Fig. 29 is an intermediate chamber with diaphragms on both sides. Pressure starts building in this chamber before the capacity of the diaphragm configuration is reached at time t=80 ms. Chamber ''3'' is also an intermediate chamber and starts building pressure at time t=100 ms. When the pressure in chamber ''1'' reaches its desired value, the shock wave is fired towards the test specimen.

There were also mounted sensors at 0.295 m and 0.395 m from the test plate. These sensors are called 409 and 410 and are present when performing actual experiments in the shock tube and are used to calculate the actual pressure at test specimen. Fig. 30 shows the pressure-time history from all the sensors for a driver pressure of 25 bar.

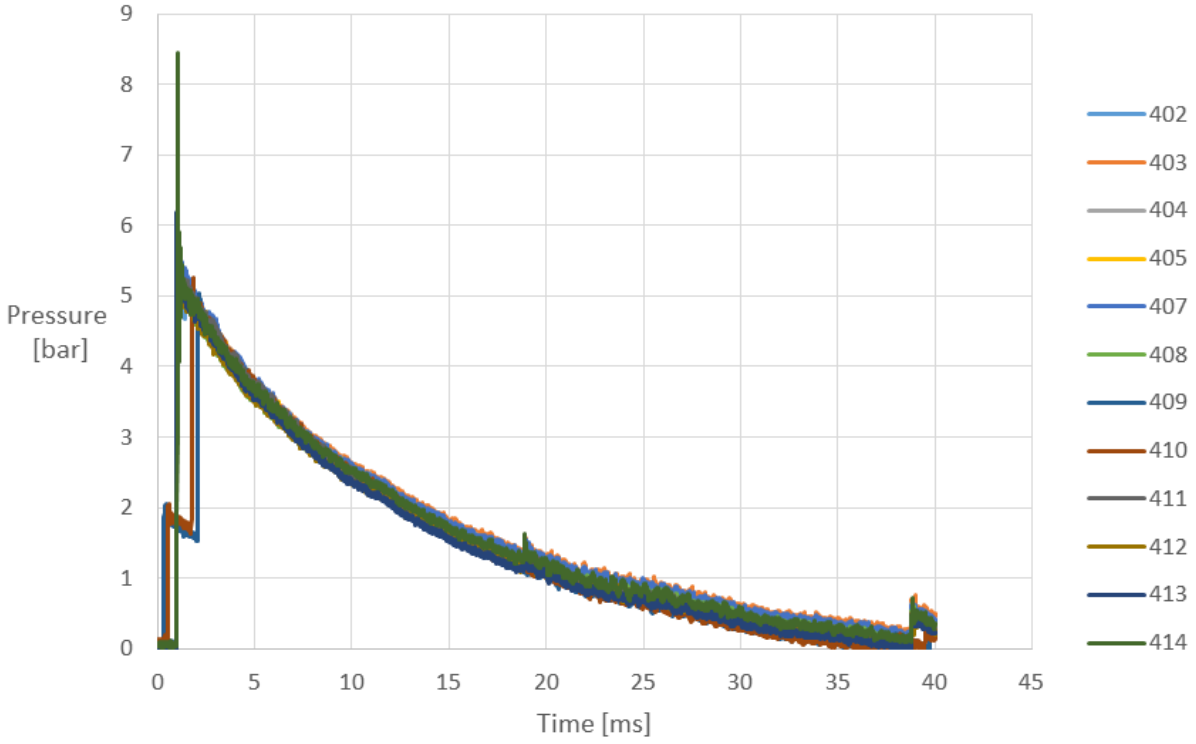

Fig. 30 Pressure-time history from a calibration test with a driver pressure of 25 bar

Measurements from the sensors on the plate lies approximately in the middle of the incident and peak overpressure measured by sensors 409 and 410. By calculating the speed of the shock wave between 409 and 410 and assuming constant velocity of the shock wave until it hits the test specimen, the peak reflected overpressure at the plate is obtained. Here, a small approximation is done and the loading curve is fitted to the curves from the pressure sensors. Notice that the sensors 413 and 414 measured larger peak overpressures than the rest of the sensors. These sensors are located towards the lower left corner of the plate and the reason for the strange values could be that the wave reflects in an unknown manner and gives larger peak values than it should.

An example of the fitting of the Friedlander curve to the pressure-time history from the shock tube are shown in Fig. 31. It is seen that the curve is similar to that from a typical ideal blast wave from Fig. 20 and it can be assumed that the SSTF can be used to simulate blast effects on structures.

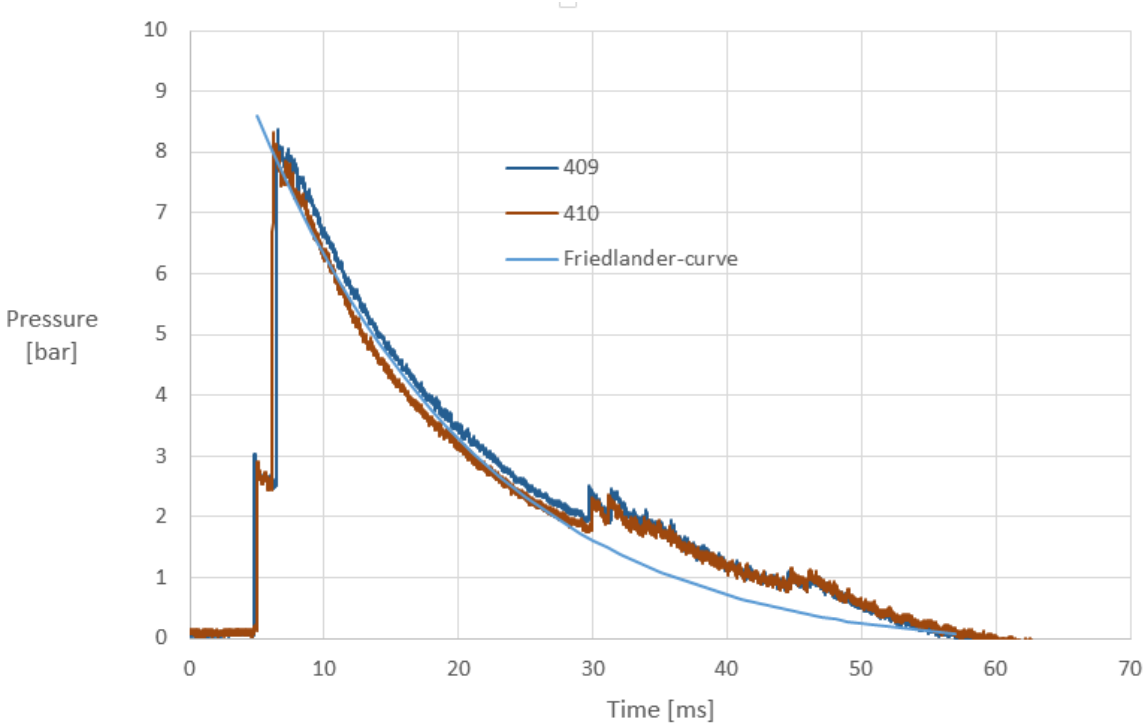

Fig. 31 Fitting of Friedlander-curve to the pressure measurements

4 Material tests

In order to achieve a best possible description of the behavior of the materials used in the component tests i.e. aluminum foam and concrete, material tests of different kinds were performed and are presented in this chapter. For the aluminum foam, uniaxial compression tests were performed, while for concrete there were performed uniaxial compression tests and splitting tension tests. The material properties for aluminum sheets were obtained from information presented by the manufacturer and can be seen in Appendix C.

4.1 Uniaxial compression tests of aluminum foam

4.1.1 Procedure

The aluminum foam used in this thesis is the same foam produced by Hydro Aluminum AS which [19] and [26] used when they validated different constitutive models for aluminum foams. In those papers, the average densities of the foam specimens were 0.17, 0.34 and 0.51 g/cm^3. Since aluminum foams have some uncertainties regarding the density, it was desirable to perform additional material tests. The plateau stress is an important property of aluminum foam, and is dependent on the density. The uniaxial compression test is a simple, yet effective way to determine the plateau stress.

For simplicity, and the knowledge of strain-rate insensitivity for aluminum foams described in chapter 2.1.2 , there were only performed uniaxial compression tests to verify material data in this case. The dimensions of the test specimens were 70 x 70 x 70 mm. Beforehand, the test specimens were weighed and measured as precisely as possible to obtain the individual densities. Because of the characteristic pore structure of foams, the measuring of the specimens were a bit demanding. The foam specimens were carved from three different foam sheets that were thought to have different densities, but it turned out that two of the sheets had roughly the same density. The measured densities for the test specimens are shown in Table 3 and Fig. 32 shows a picture of the test specimens before testing.

Table 3 Densities of the test specimens

Specimen name	Density [g/cm^3]
1-1	0.254
1-2	0.270
1-3	0.293
2-1	0.120
2-2	0.131
2-3	0.127
3-1	0.271
3-2	0.268
3-3	0.278

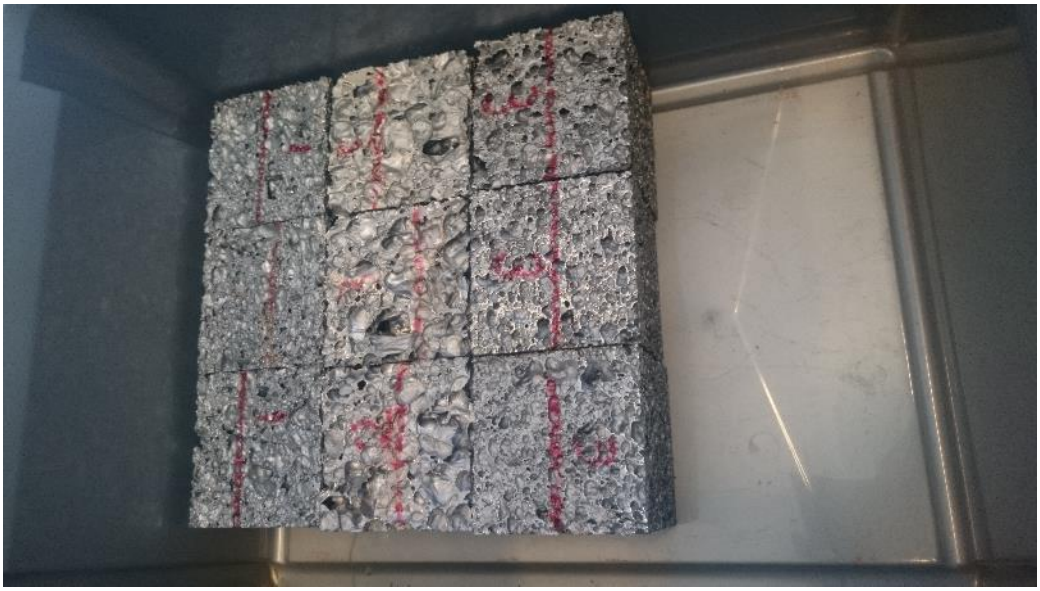

Fig. 32 Aluminum foam test specimens for uniaxial compression test

The measured densities of the test specimens are significantly smaller than expected from the densities used in [19]. The test specimens were all taken from the same place in the sheet plate. Therefore it is likely that the local density is different from where the test specimens in [19] were taken from. From this observation, it could mean that the density varies in the foam sheets, and illustrates the importance of identifying the density and plateau stress for the tested material.

Uniaxial compression tests were performed in an Instron 1332 machine with a capacity of 250 kN and Bluehill 2 software. The stress-strain curves of the foam were obtained from the uniaxial compression tests. The test specimens were loaded quasi-statically at 20 mm/min and deformed approximately 55 mm in the thickness direction. The loading direction was chosen to be in the z-direction and DIC-camera was placed perpendicular to the test specimen on two sides as shown in Fig. 33 to measure the displacement of the foam. The pictures were taken with a frequency of 4 Hz and Fig. 34 shows pictures taken by the DIC-camera for a typical uniaxial compression test.

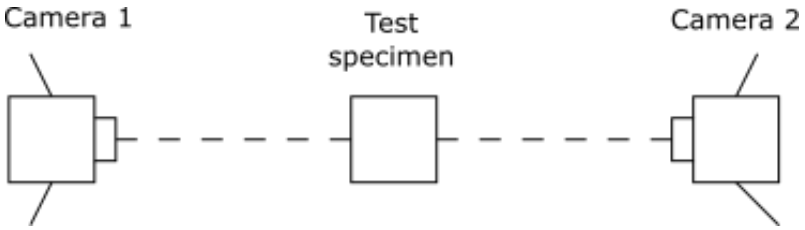

Fig. 33 Set-up of the DIC-cameras

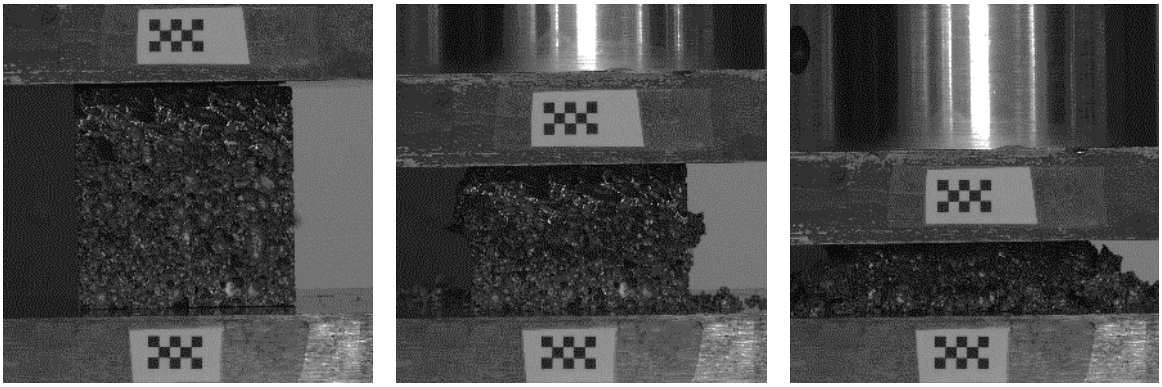

Fig. 34 Uniaxial compression test of aluminum foam

The experimental setup for the uniaxial compression test is shown in Fig. 35. The loading on the specimen was measured by a computer and synchronized with the pictures taken by the cameras to obtain the force-displacement curves. Fig. 36 shows how much the test specimen has been displaced after the test.

Fig. 35 Experimental set-up of uniaxial compression test of aluminum foam

Fig. 36 A test specimen compressed at the end of a test

4.1.2 Data analysis

The stresses and strains were obtained by processing the results from uniaxial compression tests in Excel. The displacement values are given from the two cameras on each side of the test specimens denoted C1 and C2. The average values from C1 and C2 were calculated and used for further analyses. The forces were taken from the Instron 1332 machine and a plot of the force-displacement relationship from test ''3-1'' are shown in Fig. 37.

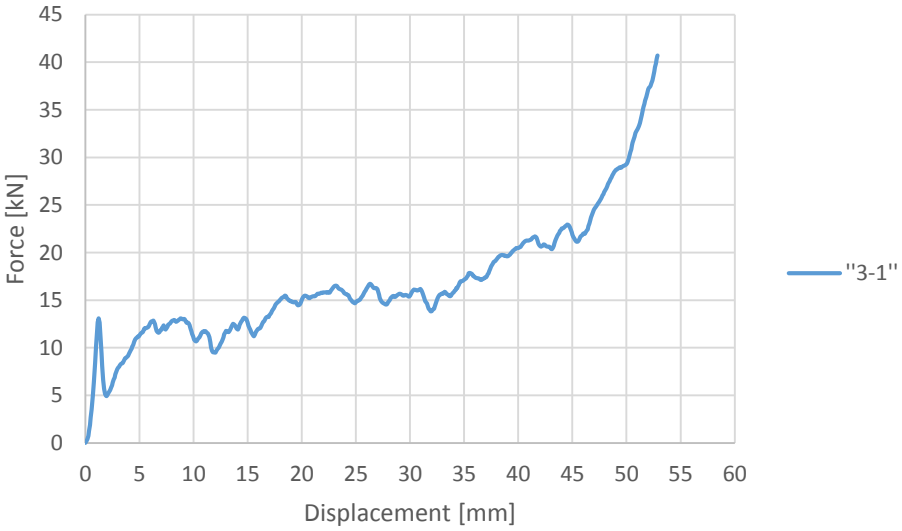

Fig. 37 Force-displacement curve from the uniaxial compression test

From the force-displacement relationship, the engineering strain e and engineering stress σ_e are calculated based on the relations

$$e = \frac{L - L_0}{L_0} = \frac{\Delta L}{L_0} \tag{41}$$

and

$$\sigma_e = \frac{F}{A_0}. \tag{42}$$

The engineering stress-strain relations does not give a true indication of the deformation of the material since it is based on the initial length of the specimens. A relationship between engineering strain and logarithmic (true) strain and between engineering stress and Cauchy (true) stress is therefore established and the true stress-strain curve is obtained as follows:

$$\varepsilon = -\ln(1 - e) \tag{43}$$

$$\sigma_t = \sigma_e(1 + e) \tag{44}$$

4.1.3 Results

The results from uniaxial compression tests shows that there are always some variations when it comes to the material properties of aluminum foam. The properties for the tested aluminum foam is given in Table 4. Here, the plateau stress is taken as the initial peak value were the stress-strain curve reaches a top and then drops before increasing slowly until densification strain is reached.

Table 4 Results from uniaxial compression tests of aluminum foam

Specimen name	Mass [g]	Density [g/cm^3]	Plateau stress [MPa]
1-1	87	0.254	1.89
1-2	92	0.270	2.33
1-3	99	0.293	2.95
2-1	43	0.120	0.34
2-2	46	0.131	0.39
2-3	44	0.127	0.29
3-1	94	0.271	2.32
3-2	95	0.268	2.25
3-3	96	0.278	2.68

Observation of how the test specimens deformed gave knowledge of how the crushing of the cell walls give rise to good energy absorption properties. The crushing started at the top of the test specimen and propagated downwards as the deformation increased. When the stress-strain curve began to increase exponentially, the tests stopped. Fig. 38 shows how the test specimens looked like after the uniaxial compression tests.

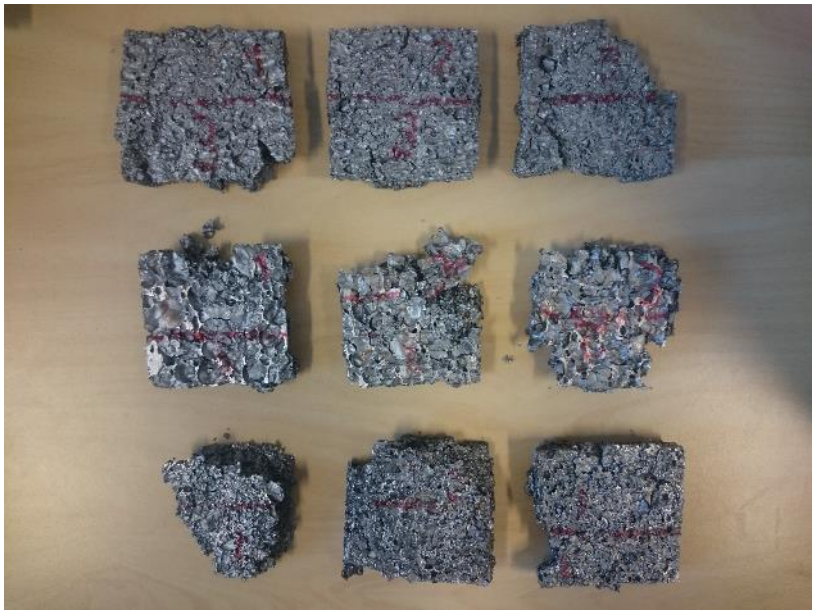

Fig. 38 Test specimens after the uniaxial compression tests

The dimensions of the test specimens were measured after the tests to find the approximate Poisson's ratio for the foam. Some of the test specimens were almost completely destroyed so the measuring became troublesome. The average Poisson's ratios for the three test groups were 0.09 for the first group, 0.04 for the second and 0.09 for the third test group. The measuring were not very accurate because it was hard to measure some of the test specimens. Based on these measurements, the Poisson's ratio have been assumed equal to zero in this thesis.

True stress-strain curves were obtained for every uniaxial compression test. The strain-hardening model in eq. (7) were fitted to each stress-strain curve. By using the problem solver in Excel, the material parameters σ_p, α_2, $1/\beta$ and γ were obtained for each test. The material parameters for each foam specimen are shown in Table 5.

Table 5 Material parameters for the analyses from uniaxial compression tests

Specimen name	ρ [g/cm^3]	σ_p [MPa]	α_2 [MPa]	$1/\beta$	γ [MPa]
1-1	0.254	1.89	11.12	0.57	5.36
1-2	0.270	2.33	13.29	0.56	6.70
1-3	0.293	2.95	16.65	0.57	5.70
2-1	0.120	0.34	5.52	0.46	1.15
2-2	0.131	0.39	9.01	0.43	1.53
2-3	0.127	0.29	11.08	0.39	1.40
3-1	0.271	2.32	12.56	0.59	4.32
3-2	0.268	2.25	20.24	0.48	5.51
3-3	0.278	2.68	19.73	0.57	3.98

Each material parameter were plotted against density as dots and by introducing the power-law function in eq. (9) the density dependency for the material parameters were obtained. The calibration of the material parameters for the strain hardening function from uniaxial loading are shown in Fig. 39.

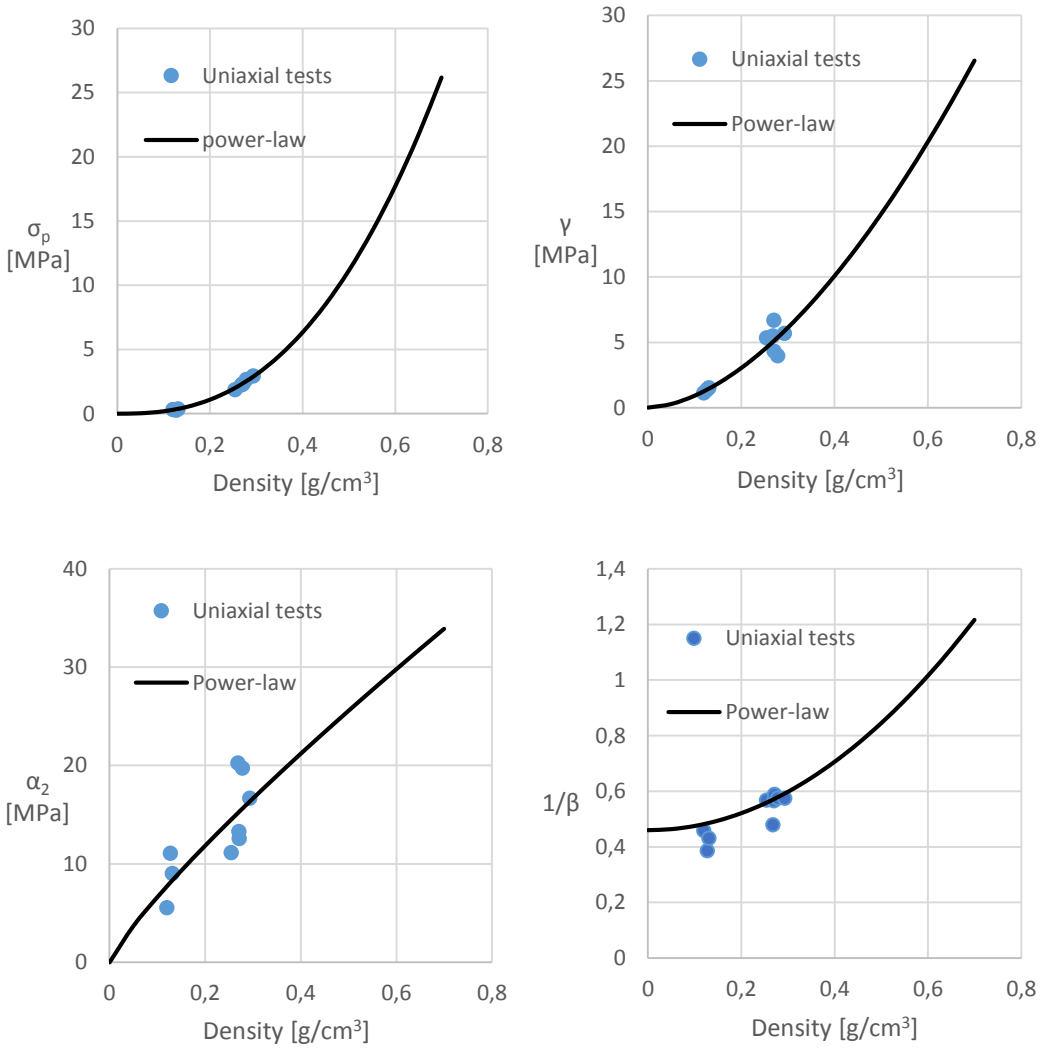

Fig. 39 Calibration of material parameters for the strain hardening function

The results from calibration of the constants C_0, C_1 and n for each material parameter are summarized in Table 6. These values are adopted in the numerical model and all analyses are performed with this dependency on the density of the aluminum foam.

Table 6 Calibrated values from uniaxial compression tests

	σ_p	γ	α_2	$1/\beta$
C_0	0	0	0	0.46
C_1	803	275	105	11.4
n	2.54	1.73	0.84	2.01

In the end, the calibrated stress-strain relationship from the power-law relation in eq. (9) are compared to the results from the uniaxial compression tests. Fig. 40, Fig. 41 and Fig. 42 shows the stress-strain curves for every test.

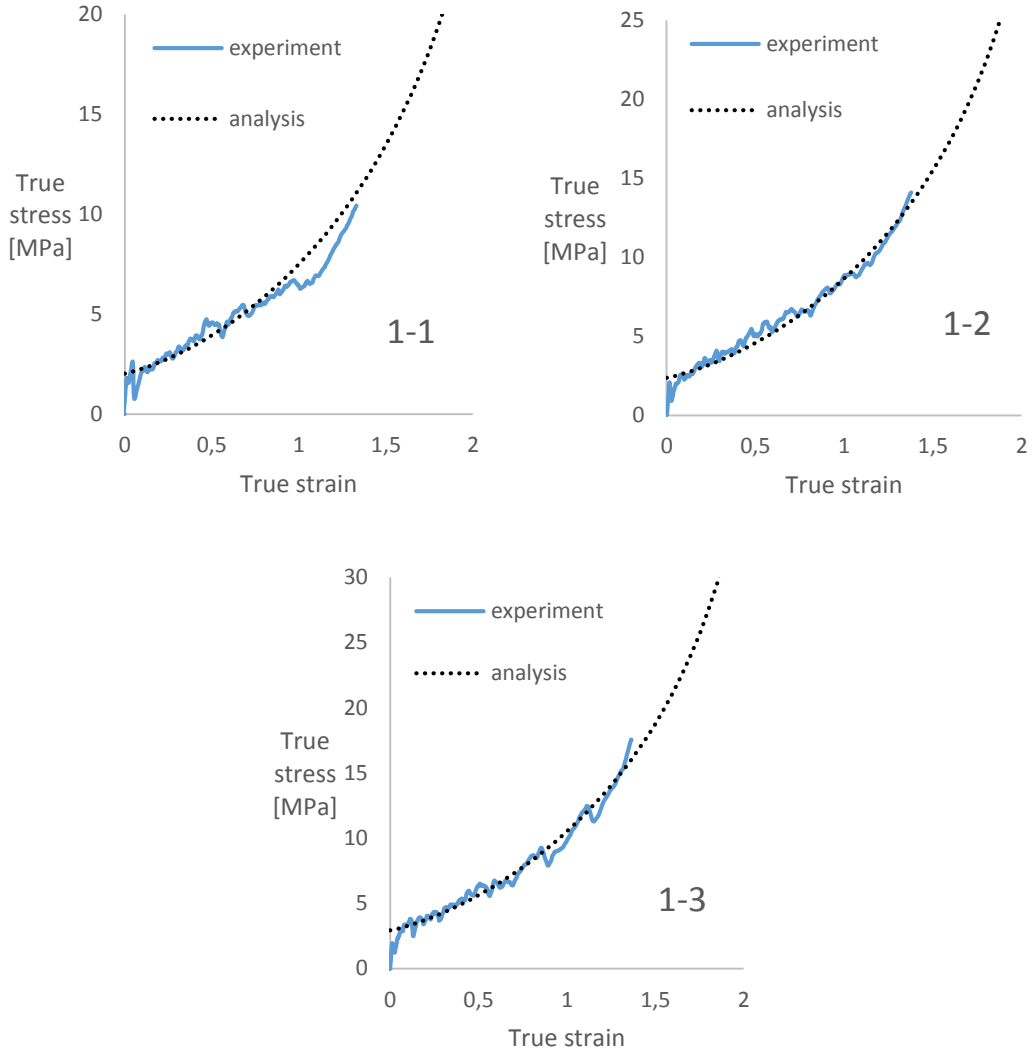

Fig. 40 Stress-strain plots for uniaxial compression for test group ''1''

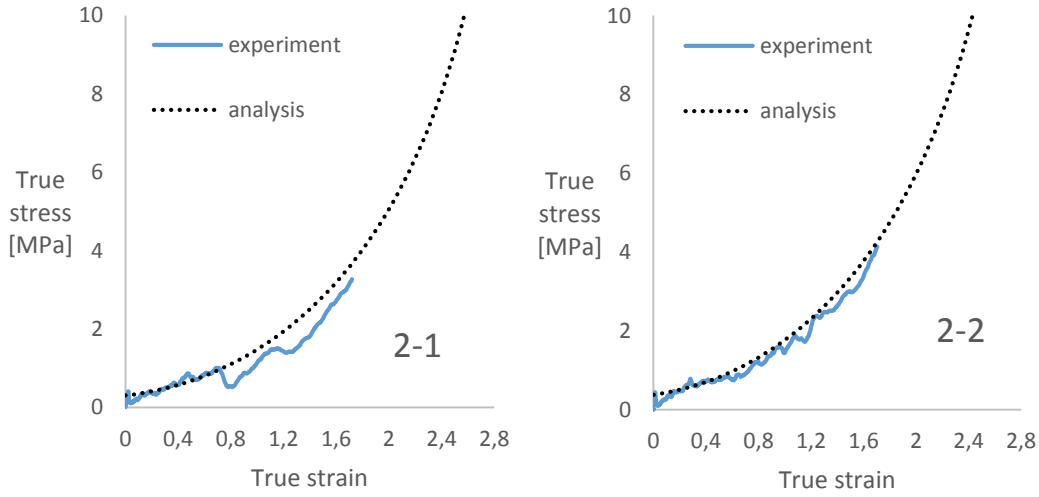

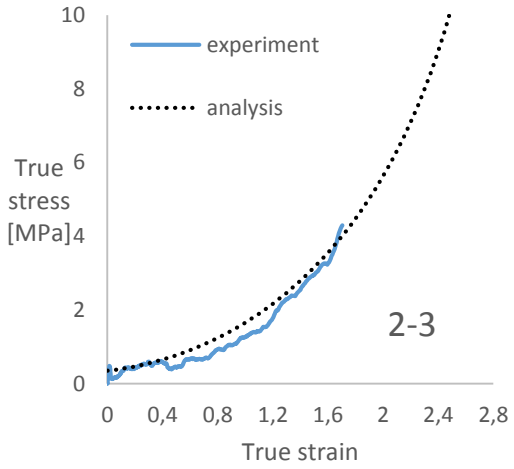

Fig. 41 Stress-strain plots for uniaxial compression for test group ''2''

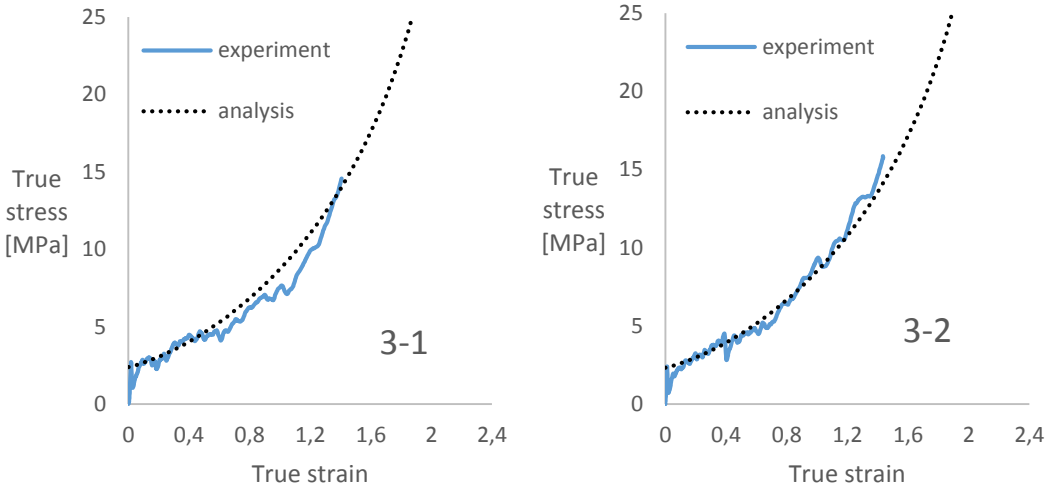

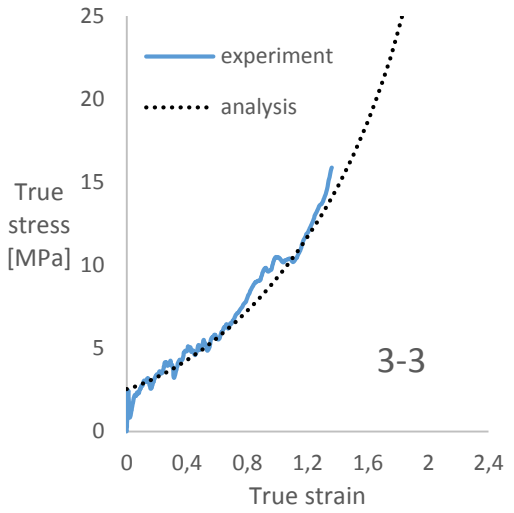

Fig. 42 Stress-strain plots for uniaxial compression for test group ''3''

4.2 Concrete tests

4.2.1 Preparation

Due to the initial idea of investigating the effect of aluminum foam panels on concrete plates, time were spent in the concrete laboratory to make the concrete plates. This was done in cooperation with fellow master students Karoline Osnes and Sondre Haug who were investigating the behavior of concrete when subjected to blast loading.

It was necessary to construct formwork for the concrete plates. The formwork consisted of timber plates with Ø25 boltholes and polystyrene tubes were threaded through the holes. Some shape reinforcement were inserted to take care of trouble with cracks at the boundary and increase adhesiveness. In total, fifteen plates were made with dimensions 625x625mm^2 and thicknesses 50 mm, 100 mm and 200 mm. Pictures of the formwork construction are shown in Fig. 43 and Fig. 44.

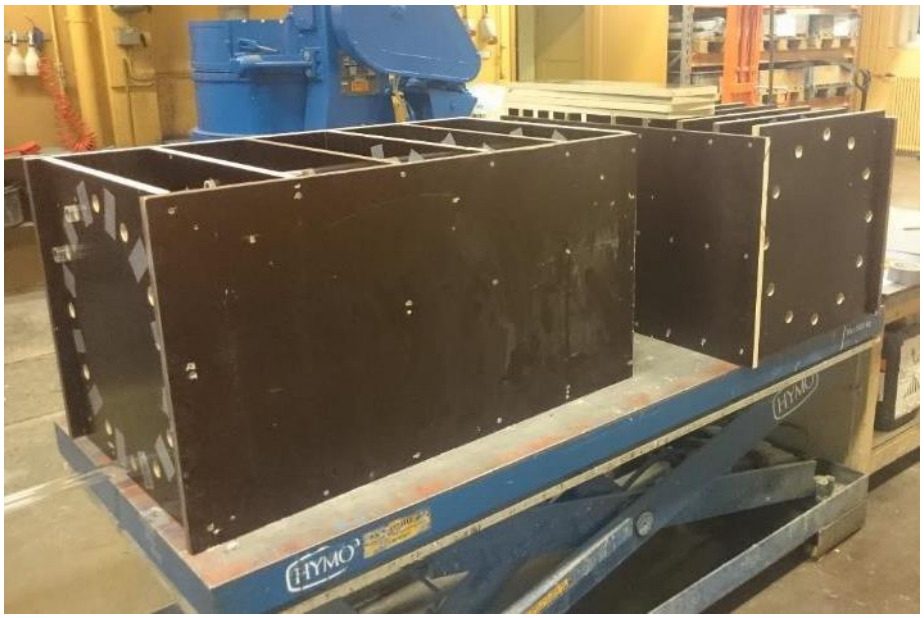

Fig. 43 Formwork for the concrete plates

Fig. 44 Reinforcement bars inserted

The concrete plates were casted and surrounded by a wet climate for 28 days. It was expected to reach 95 % of final strength after this period. Test specimens for material tests were casted at the same time. The test specimens consisted of 15 cubes with standard dimension 1 dm^3 and 15 cylinders with a diameter of 100 mm and 200 mm length. The cubes were used for compression tests, while the cylinders were used in splitting tension tests. All procedures were done according to NS-EN 12390 [41].

4.2.2 Compression test

Standard uniaxial compression tests were performed on cubes in order to find the material properties of the concrete according to NS-EN 12390-3:2009 [41]. In this test, the compressive strength of the material was determined. The test method consists of applying an axial compressive load at a prescribed rate until failure occurs. The rate of load application were chosen to be 0.8 MPa/s. The compressive strength of the material was calculated by taking the maximum applied load and dividing it by the cross-sectional area of the test specimen. Fig. 45 shows a test specimen inserted in the testing machine.

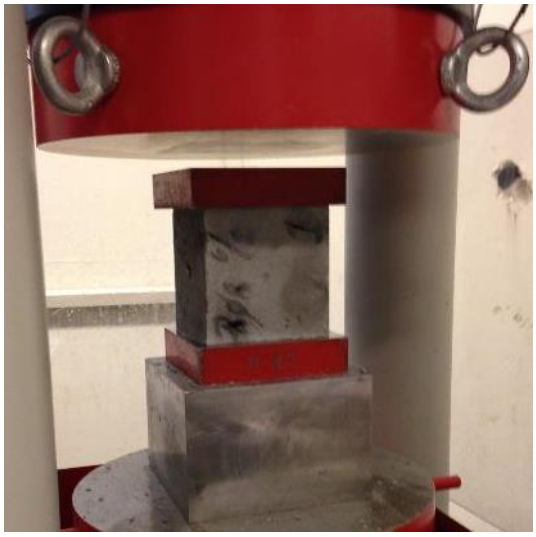

Fig. 45 Experimental set-up for uniaxial compression test

The test specimens were first weighed in water and then with dry surfaces to measure the water to cement ratio. Results from measurements and testing are shown in Table 7.

Table 7 Results from uniaxial compression tests

	Weight in water (g)	Weight in air (g)	Compression strength f_{ck} (MPa)
1	1364.3	2357.0	65.95
2	1337.6	2322.7	64.50
3	1324.0	2306.5	64.12

4.2.3 Splitting tension test

Standard splitting tension tests were performed to check the splitting tensile strength according to NS-EN 12390-6 [41]. A compressive force was applied along the length of a cylindrical concrete specimen until failure occurred. In order to distribute the load applied along the cylinder, thin, plywood-bearing strips were placed on both sides of the test specimen. The bearing strips can be seen on the top and bottom of the cylinder in Fig. 46.

Fig. 46 Experimental set-up of splitting tension test

This way of applying the load induced tensile stresses along the plane containing the applied load and high compressive stresses in the area around the applied load. Tensile failure occurs rather than compressive failure because the areas of load application are in a state of triaxial compression. The maximum load sustained by the specimen was divided by appropriate factors to obtain the splitting tensile strength. The following expression calculates the capacity

$$f_{ct} = \frac{2 \times F}{\pi \times L \times d} \tag{45}$$

Where F is the maximum load, L is the length of the line of contact of the specimen, and d is the designated cross-sectional dimension. The results from the splitting tensile tests are shown in Table 8.

Table 8 Results from splitting tension tests

Test specimen	Height (mm)	Diameter (mm)	Load (ton)	Splitting tensile strength f_{ct} (MPa)
1	197,3	99,45/100,04/101,93	14	4.5
2	196,21	100,41/100,31/100,02	13,3	4.3
3	194,75	100,23/100,12/100,3	11,9	3.9

5 Analytical calculations

In order to get some knowledge about the response of an aluminum foam plate with clamped boundary conditions, some analytical calculations were done based on thin-plate theory. Some assumptions and restrictions are introduced when using thin-plate theory. The plate thickness *t* should be small in comparison with the span wise dimensions of the plate. A typical assumption is that *t* should be no more than about *1/10* of the smallest plate dimension in the *xy*-plane. For our case *t/a= 38/300=0.13* which is slightly larger than *0.10.* However, we will use the solution just as a rough estimate. The material is assumed homogeneous, isotropic and linearly elastic even though it is known that this is not exactly the case for aluminum foam.

For rectangular plates with clamped edges the expressions needed to calculate displacement at the midpoint, w_C, and edge and central bending moment $(M_x)_{B,C}$ respectively is taken from Cook and Young [42]

$$w_C = 0.00126\frac{qa^4}{D} \tag{46}$$

$$(M_x)_B = -0.0513qa^2 \tag{47}$$

$$(M_x)_C = 0.0231qa^2 \tag{48}$$

Subscripts *B* and *C* represents edge and center of the plate respectively and $D = \frac{Et^3}{12(1-\nu^2)}$ is the flexural rigidity of the plate. For the purpose of these calculations, it is assumed that the blast loading can be applied as a uniform static pressure. In reality, the pressure would be dynamic, but the purpose of the analytical calculation is to get a rough estimate of the stresses in the foam at given pressures. Three different pressures are considered that are expected to be close to the pressures used in the experiments.

The stresses can be calculated from the bending moment as $\bar{\sigma}_x = \mp\frac{6M_x}{t^2}$. For our case, we use the dimensions from our experiments: length *a=300 mm*, thickness *t=38 mm*. Poisson's ratio is assumed zero for the aluminum foam. The calculations are based on a foam density of 0.42 g/cm^3 with elastic modulus 2919.2 N/mm^2. The results from the analytical solution are shown in Table 9 for three different pressures.

Table 9 Analytical solution to a clamped foam plate with uniform static loading

q [MPa]	$\bar{\sigma}_{x,B}$ [MPa]	$\bar{\sigma}_{x,C}$ [MPa]	w_C [mm]
0.5	9.59	4.32	0.38
0.8	15.35	6.91	0.61
1.1	21.10	9.50	0.84

6 Experimental tests

6.1 Concrete plates

An investigation on how aluminum foam plates could protect concrete structures were initially the main objective in this thesis, but as it turned out that the pressures needed to get cracks in the concrete were larger than expected, the focus in this thesis changed to sandwich structures with an aluminum foam core. The blast loading of concrete plates without any protection was done by Sondre Haug and Karoline Osnes and reported in their master's thesis. The results from those tests are not reported here. However, aluminum foam on a concrete plate is investigated numerically in Abaqus/Explicit to investigate if the response in the concrete changes when adding aluminum foam.

6.2 Sandwich structures

The sandwich structure consisted of an aluminum foam core and thin aluminum plates on each side of the core. The aluminum plates had a thickness of 0.8 mm, and were made of AA1050 – H14 aluminum alloy with chemical composition 99.592 %Al, 0.1 %Si, 0.28 %Fe, 0.01 %Mn, 0.002 %Mg, 0.003 %Cu, 0.002 %Zn, 0.002 %Cr, 0.009 %Ti. Twelve bolts in a circular pattern as shown in Fig. 47 bolted the aluminum foam core and the aluminum sheet plates together.

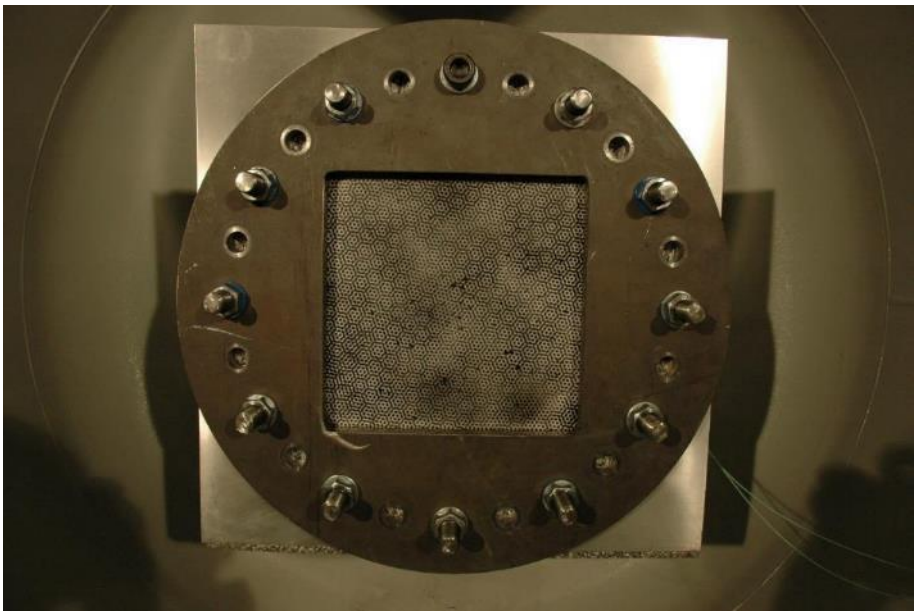

Fig. 47 Test specimen before experiment ''210-1''

Fig. 48 shows a description of the different parts of the experimental setup in the shock tube. The front plate is the plate towards the shock wave, while the back plate is the plate behind

the aluminum foam core. The boundary conditions are assumed to be fully clamped when the bolts are tightened.

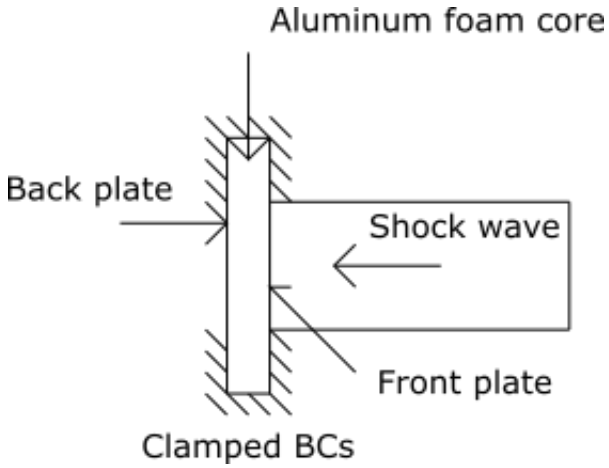

Fig. 48 Description of the experimental set-up in the shock tube

6.2.1 Preliminary experiment

In the preliminary experiment, two foam plates were cut from the foam sheet. The foam sheets had a thickness of approximately 100 mm and were cut in half as close to the middle as possible to create the plates. The density of the foam plates were measured as exactly as possible. This was done by measuring the plate dimensions, giving the volume, and then weighing the plate. The density of the material tests from the same sheet was $\rho=0.27\ g/cm^3$, but individual measurements of each foam plate were done because the aluminum foam is known to have a variable density.

The plates were weighed after the holes for the bolts were drilled. Lengths, widths and thicknesses were measured at five different spots along the test specimens and the area were calculated based on the average values for length and width. The area of the holes were subtracted to achieve the total volume of the plate by multiplying with the average thickness of the test specimen. The thickness was measured using a caliper with 0.01 mm accuracy. However, because of the irregular structure of the foam, it was difficult to get an exact measurement. In Table 10, the properties of the foam plates for the preliminary experiments are shown. The test specimen cut out from the top layer of the foam sheet had a significantly lower density than the test specimen cut out from the bottom layer did. This phenomenon regarding the density variation were explained in chapter 2.1.2.

Table 10 Properties of the foam plates for the preliminary tests

Test specimen	210-1	420-1
Weight [g]	3672.7	6222.4
Length [cm]	62.66	62.76
Width [cm]	62.20	62.12
Area [cm^2]	3838.53	3839.73
Avg. thickness [cm]	4.550	3.836
Volume [cm^3]	17465.3	14729.2
Density [g/cm^3]	**0.21**	**0.42**

Test ''210-1''

It was decided to test the sandwich structure with the low-density foam first. The foam core had a density of 0.21 g/cm^3 and an average thickness of 45 mm. It was attempted to reach a peak reflected overpressure of 1000 kPa on the plate. DIC cameras were mounted to measure displacements of the back plate during the test.

Due to some difficulties regarding cutting straight plates of the aluminum cores, the thickness of the core for this experiment were a bit irregular. It was therefore hard to achieve full contact between the aluminum sheet plates and the aluminum foam core. The effects of this irregularity in the foam plate were assumed small, but a further investigation on the issue was not performed. Fig. 47 shows the test specimen after the back plate were mounted and the bolts tightened to apply the clamped boundary conditions. Fig. 49 shows the aluminum foam core mounted in the shock tube before the back plate were inserted.

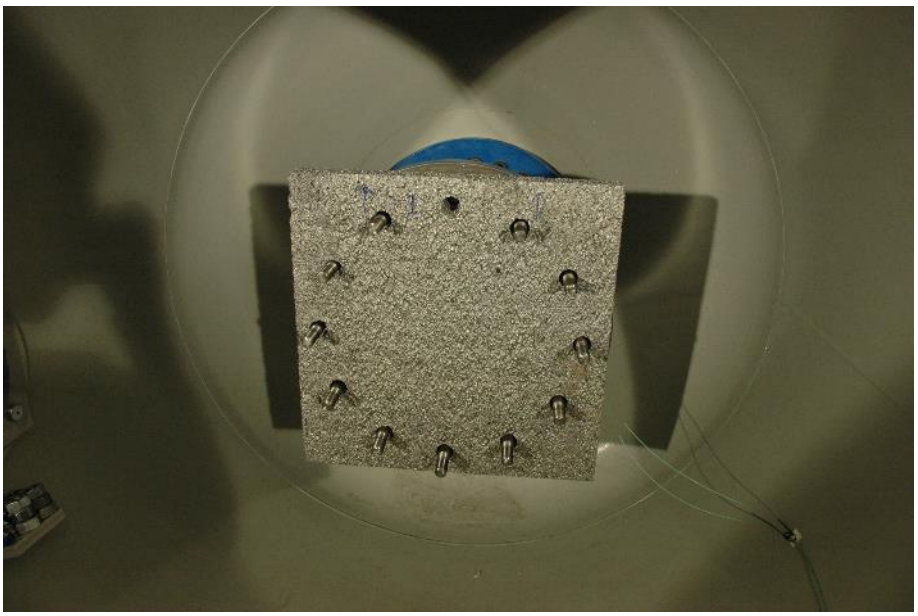

Fig. 49 Foam core mounted in the shock tube

The peak reflected overpressure achieved on the plate were approximately 1000 kPa. Pictures of the sandwich structure ''210-1'' are shown in Fig. 50 to Fig. 54 and it can be seen that the sandwich structure ruptured severely. Fig. 50 displays the test specimen after the test, while Fig. 51 illustrates failure of the different parts of the sandwich structure. The aluminum foam core fractured into several fragments of various sizes as shown in Fig. 52. Additionally, part of the foam core pulverized and a lot of dust was observed around the shock tube.

The aluminum sheet plates experienced different failure modes. The front plate of the test specimen ruptured along the boundaries as shown in Fig. 53. When the shock wave hits the test specimen, the front plate is backed by the aluminum foam core and the back plate. When observing the failure of the back plate in Fig. 54 it is clear that the failure is different from the front plate. The back plate were ripped open from right to left and what remained of the plate was crumbled at the left side after the test. This may be because the back plate was not backed by anything and the fact that the failure started at the upper right corner of the test specimen.

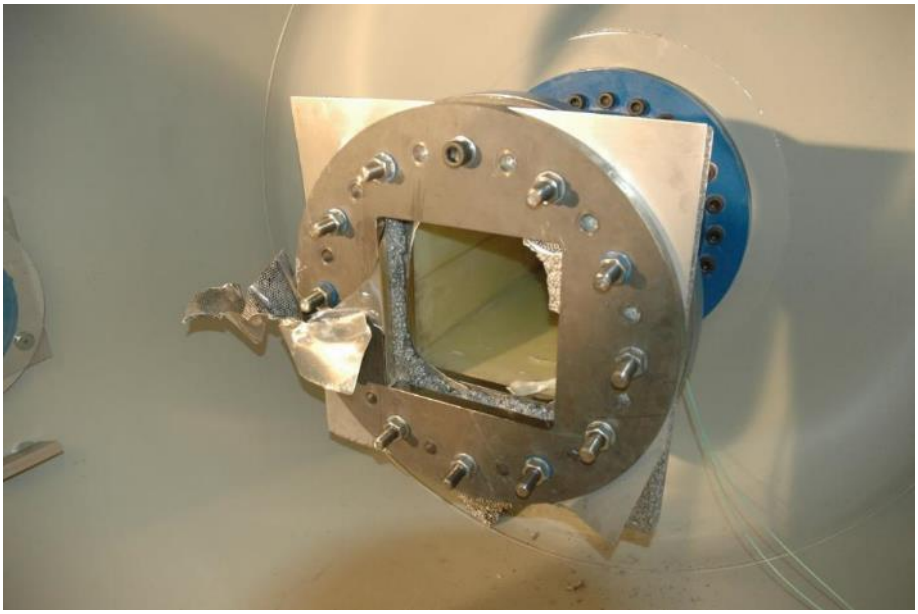

Fig. 50 Test specimen after experiment ''210-1''

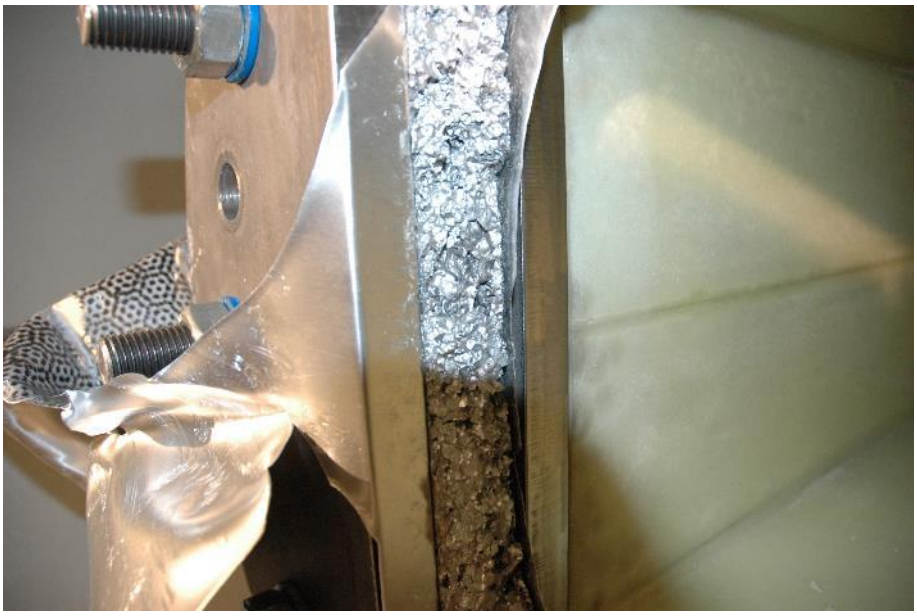

Fig. 51 Failure in the test specimen after experiment ''210-1''

Fig. 52 Fragments of the aluminum foam after experiment ''210-1''

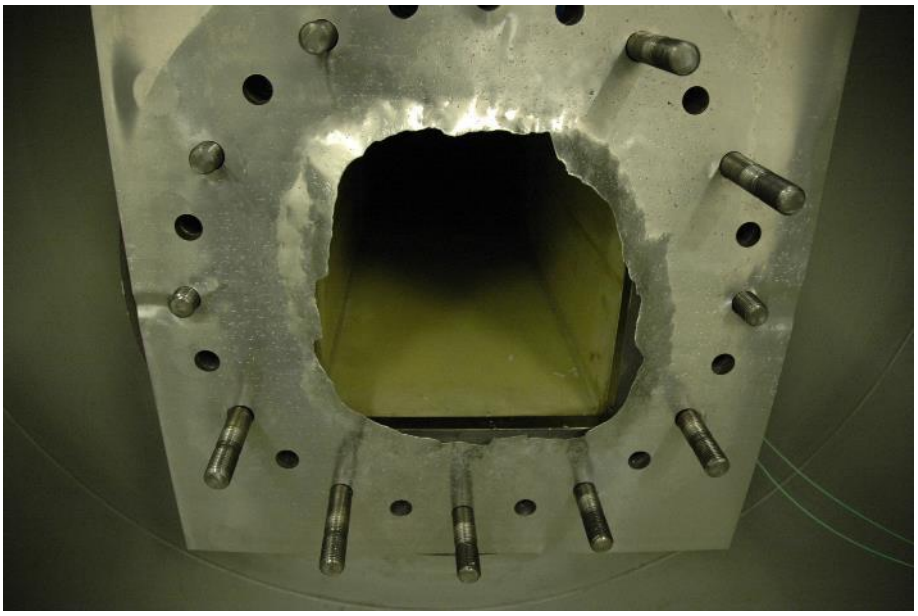

Fig. 53 Failure of the front plate of the test specimen after experiment ''210-1''

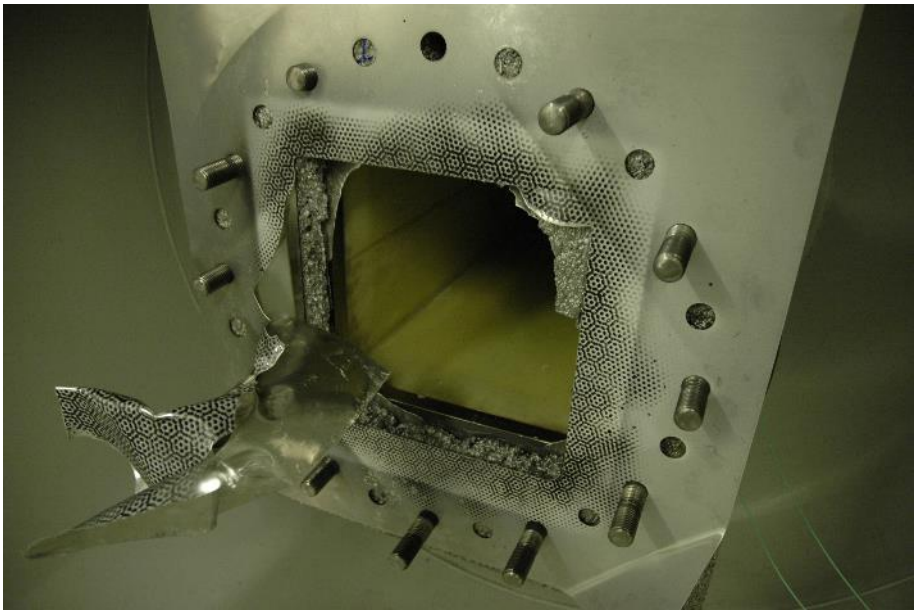

Fig. 54 Failure of the back plate of the test specimen after experiment ''210-1''

It seems as when the front plate and the foam fractured, they acted as a projectile causing also the back plate to fracture.

It is evident that the pressure chosen in this experiment was too large to obtain the desired response in the test specimen. Further experiments were put on hold until detailed investigation into the behavior of the aluminum foam in the shock tube were done.

6.2.2 Main experiments

Before more testing was done, some considerations regarding the structure and selection of pressure-time histories were done. The sandwich structures with aluminum foam core and 0.8 mm aluminum plates on each side were the same. Now, two additional foam plates were cut from the same foam sheet and different densities were obtained: 0.22 and 0.35 g/cm^3. In addition, the remaining foam plate from the preliminary experiment with density 0.42 g/cm^3 was tested. An ideal situation would have been to use plates with equal density in order to reduce the number of variables in the experiment, but because of the variation in density due to the production process and gravity, it proved difficult to obtain equal plate densities.

An investigation regarding the equivalent thickness for the sandwich structures so that the mass of the sandwich structure became equal to that of one aluminum plate were carried out. For the 0.22 g/cm^3 foam, an equivalent thickness of a foam/aluminum plate sandwich compared to a 2 mm aluminum plate equals a foam core thickness of 4.9 mm, and for higher densities, even thinner. Such small thicknesses for aluminum foams might be difficult to produce because this would lead to a small amount of cells over the thickness and the efficiency of the foam would be poor. As a result, the thickness of the aluminum foam cores were chosen to be approximately 40 mm for all the densities to reduce variables in the experiments. The properties of the test specimens used in the main experiments are shown in Table 11.

Table 11 Properties of test specimens in the main experiments

Experiment no	*Density (g/cm^3)*	*Thickness (mm)*	*Al. Plate (mm)*	*Total mass (g/cm^2)*
220-1	0.22	40.9	2 x 0.8	1.33
350-1a	0.35	40.2	2 x 0.8	1.84
350-1b	0.35	40.2	2 x 0.8	1.84
350-1c	0.35	40.2	2 x 0.8	1.84
420-1	0.42	38.4	2 x 0.8	2.04

An important consideration is the mass of the structures tested. The mass of a 2 mm aluminum plate were compared because there existed results from tests in the shock tube for these plates. Aluminum plates with a thickness of 2 mm has a mass of 0.54 g/cm^2. For experiment ''220-1'', the mass relationship compared to aluminum plates are 2.46. For ''350-1a, b, c'' and ''420-1'', it is 3.41 and 3.78, respectively. Note that it is not expected that the sandwich structures tested should withstand peak overpressures as large as 3 times as one 2 mm aluminum plate. Unknown interaction between the plates and aluminum core could occur and since there is little knowledge of how a clamped sandwich structure of this type behaves in a shock tube facility, driver pressures and peak overpressures were chosen with care.

Fellow master students Cecilie Baglo and Therese Myrstad Dybvik had already done experiments on aluminum plates alone and found that one 0.8 mm aluminum plate experienced failure at a peak overpressure of 240 kPa. For aluminum plates with 2 mm thickness, failure began at a peak overpressure of 640 kPa. Another aspect regarding the foam cores is the difference in front and back surfaces. An illustration of the difference in the foam surfaces are shown in Fig. 55 and Fig. 56. After production, the aluminum foam sheets have a ''skin'' on the surface. In this thesis, the skin was kept, and the plate was mounted so the skin faced the front plate for all experiments.

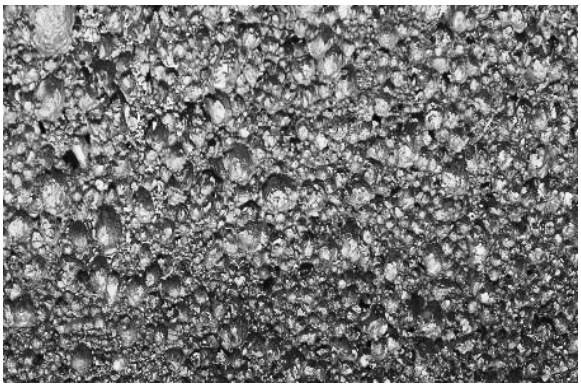

Fig. 55 Surface facing the back plate

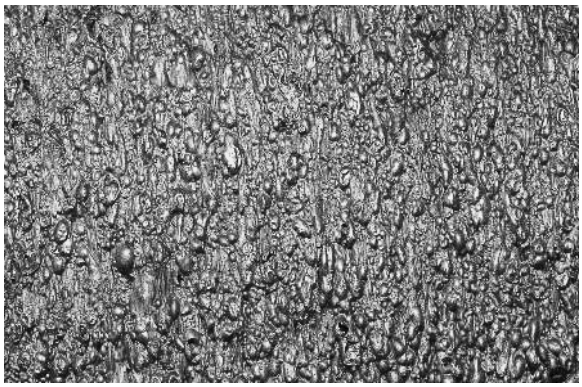

Fig. 56 Surface facing the front plate

Experiment ''220-1''

The driver pressure in the shock tube was chosen to be 15 bar, which gave a peak reflected overpressure of 3.6 bar or 360 kPa on the plate. DIC measurements were performed with a frequency of 20 s^{-1}. Pressure sensors measured the pressure down the tube and measured a peak reflected overpressure of 360 kPa as expected.

Inspection of the specimen after the experiment showed that failure probably had begun at the tension-loaded part of the foam. Clearly visible yield lines was present on both sides of the aluminum foam core in addition to some deformation at the middle of the plate. Fig. 57 shows the failure pattern at the front surface of the foam core. The yield lines follows the boundaries, but cuts the corners in some extent. This corner effect could be due to the clamped boundary conditions. In Fig. 58, the failure pattern at the back surface is shown. Here, the failure begins in the middle of the plate and propagates towards the corners.

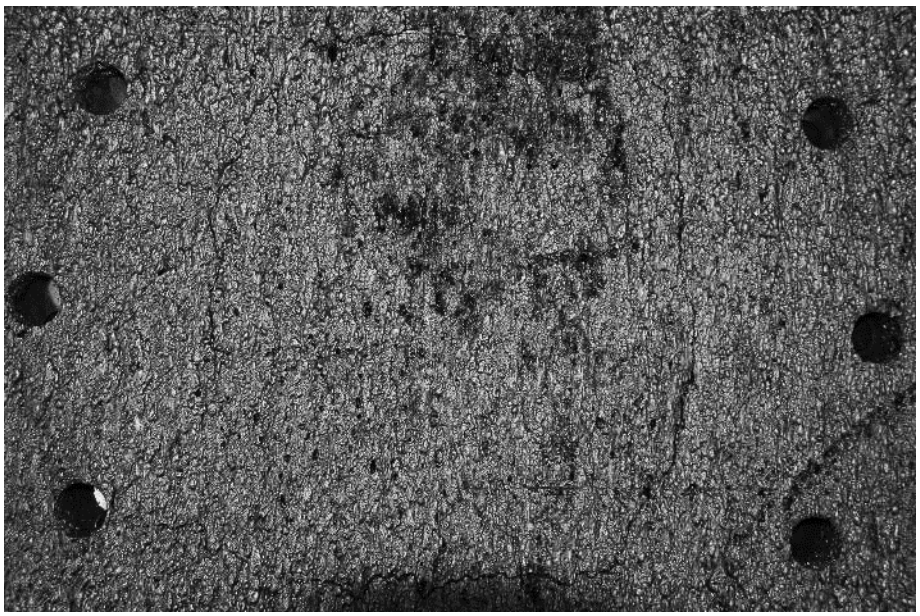

Fig. 57 Failure pattern at the front surface of the foam for experiment "220-1"

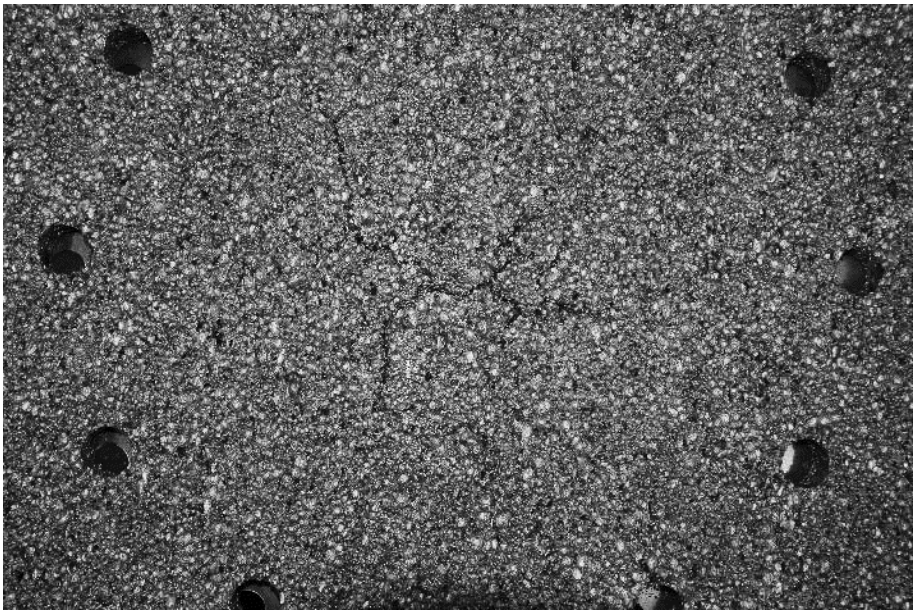

Fig. 58 Failure pattern at the back surface of the foam for experiment "220-1"

Experiments by Hanssen et al. [19] has shown that the aluminum foam experience failure in tension approximately when the initial plateau stress is reached in compression. Aluminum

foam behaves well in pure compression, but experience a brittle failure mode in tension. When bending occurs in a plate, it is known from basic mechanics that there will be tension forces on one side of the neutral axis and compression forces on the other side. Clearly, the tension forces present from the bending of the plate at a peak overpressure of 360 kPa are so high that the material have started to crack, but exactly how far from complete failure is difficult to assume.

Experiments ''350-1a'' and 350-1b''

A driver pressure of 20 bar was chosen for the sandwich structure with a foam core density of 0.35 g/cm^3. In the first attempt to build pressure, a rupture or irregularity in one of the diaphragms caused a misfire of the pressure wave when the driver pressure reached 10 bar. The pressures were not measured, but the peak overpressure were assumed to reach approximately 200 kPa. There were no damage seen in the plates, so it was decided to make another attempt on the same structure.

Experiments were performed at both 20 bar and 25 bar in the driver section, giving peak reflected overpressures at respectively 460 kPa and 530 kPa, but it turned out that these pressures did not cause any damage to the sandwich structure.

Experiment ''350-1c''

In order to obtain similar failure pattern as in experiment "220-1", a peak reflected overpressure of 590 kPa were chosen. The tank behind the test specimen was closed, so accurate DIC measurements was not possible in this experiment. A camera was placed outside the tank to take pictures of the deformation history of the plate. Again, no visible deformation of the plate was seen, but the failure pattern at the back surface was visible and shown in Fig. 59. No failure was observed on the front surface of the foam core, which was strange, as we would expect higher stresses from the boundary moments than in the fields. The analytical calculations in chapter 5 also shows the same distribution of stresses. However, the reason could be the skin-like surface on this side, which might be stronger than the rest of the foam core. The deformations of the back plate were measured along a horizontal line close to the middle of the test specimen while the structure was still mounted in the shock tube. Approximately 2 mm deformation was measured at the middle of the plate.

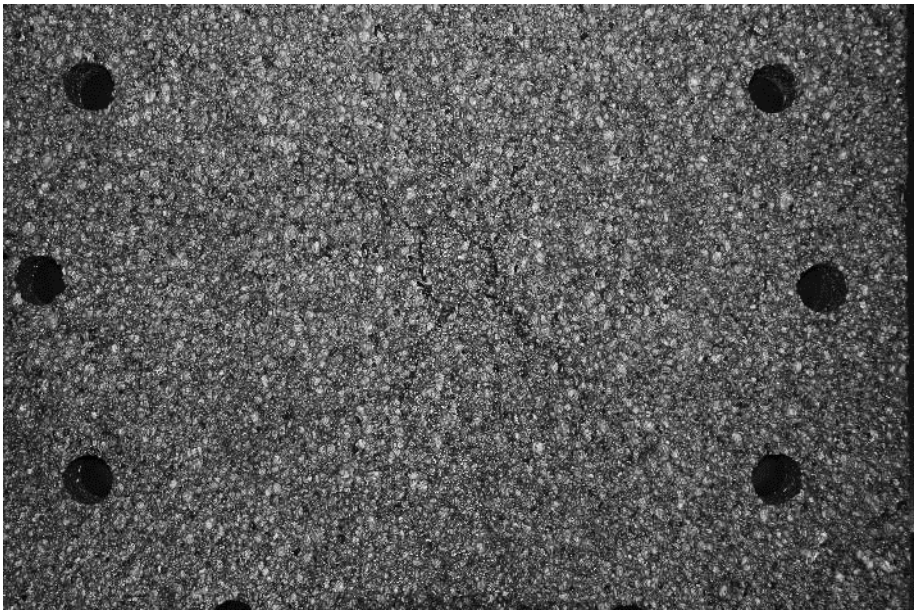

Fig. 59 Failure pattern at the back plate for experiment ''350-1c''

Experiment "420-1"

For the last experiment, the reflected peak overpressure were chosen to be 1000 kPa to obtain approximately the same amount of failure as in "220-1". Because the length of the driver section were changed, a driver pressure of 25 bar were chosen. After the test, the actual pressure on the test specimen were measured to be 860 kPa. Displacements of the back plate were again measured manually and the maximum displacement were approximately 16 mm. A 3D plot of the measured deformation was made in Matlab and shown in Fig. 60.

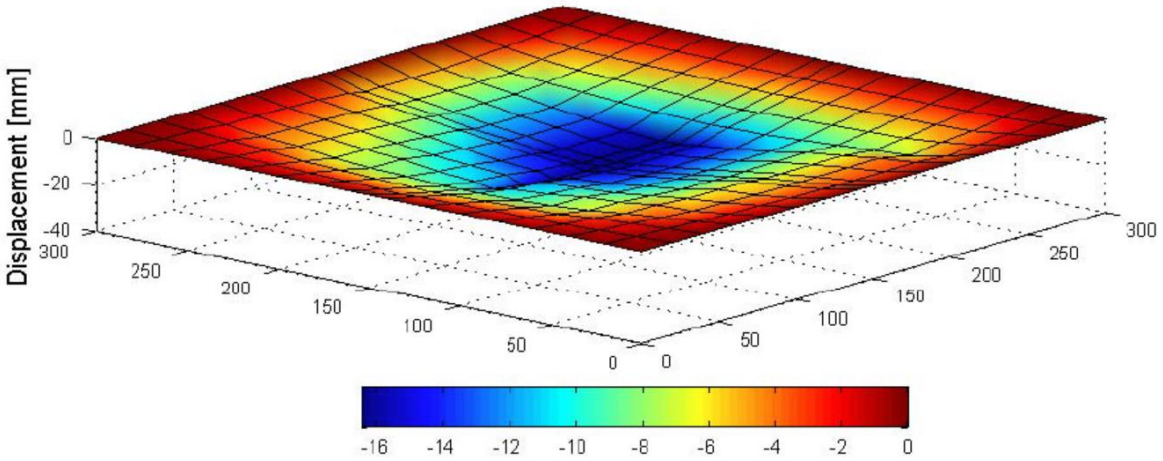

Fig. 60 Deformation of the back plate for "420-1"

The foam core experienced severe failure with similar pattern as earlier experiments. The widths of the cracks were larger than for experiment "220-1" and "350-1c". Fig. 61 shows the failure pattern at the back surface of the foam and Fig. 62 shows the failure pattern at the front surface. There is clearly visible deformation in the foam, indicating that the stresses in the

foam are well into the plateau region of the stress-strain curve. The foam cracks along the weakest cell walls and this may be why the pattern looks somewhat irregular in shape. It can seem like the cracks initiate in the middle of the back surface of the plate and propagates towards the corners of the quadratic plate.

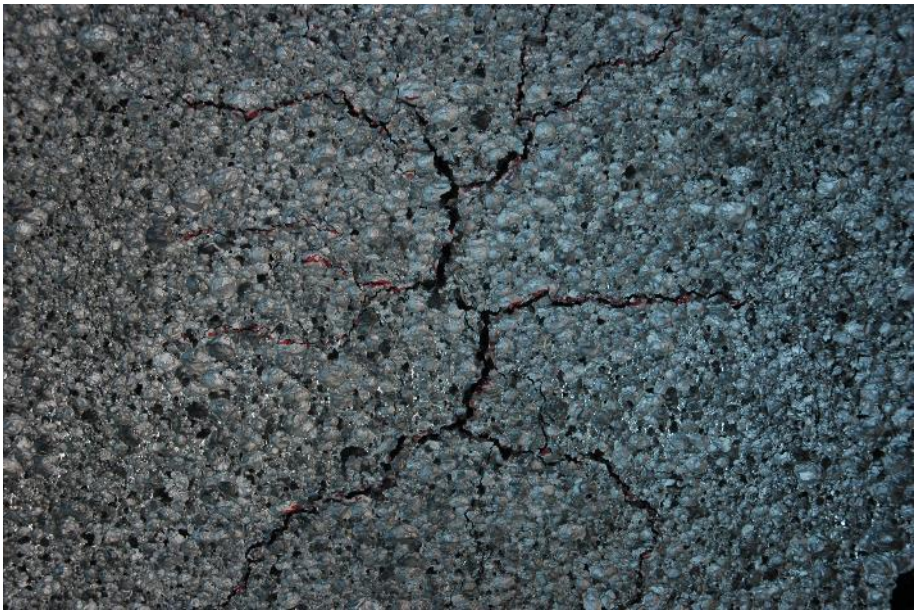

Fig. 61 Failure pattern at the back surface of the foam for experiment "420-1"

Fig. 62 Failure pattern at the front surface of the foam for experiment "420-1"

Fig. 64 shows the loading history for the time period inside the box from Fig. 63 for experiment ''420-1''. In Fig. 65, the DIC-images are shown at times according to Fig. 64.

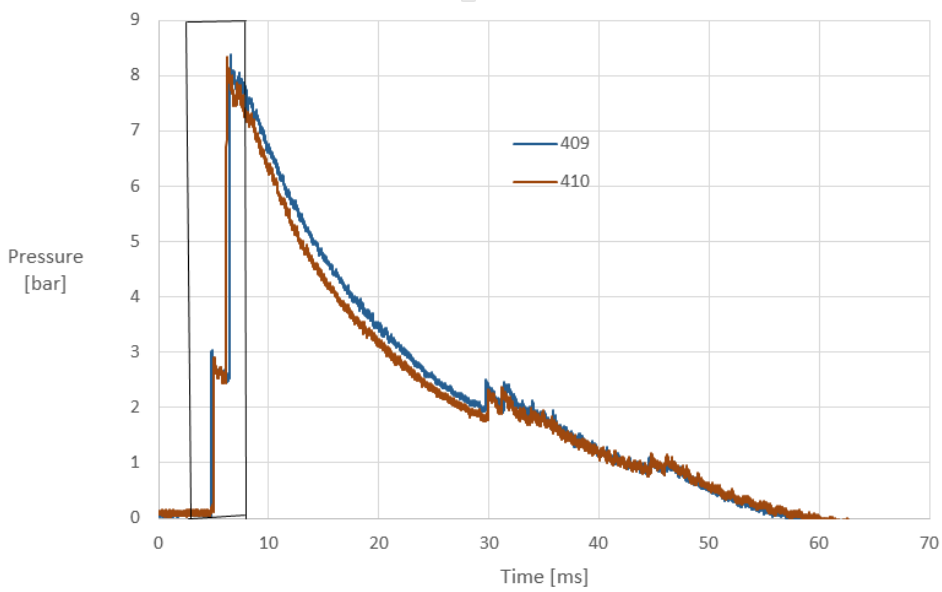

Fig. 63 Pressure-time history

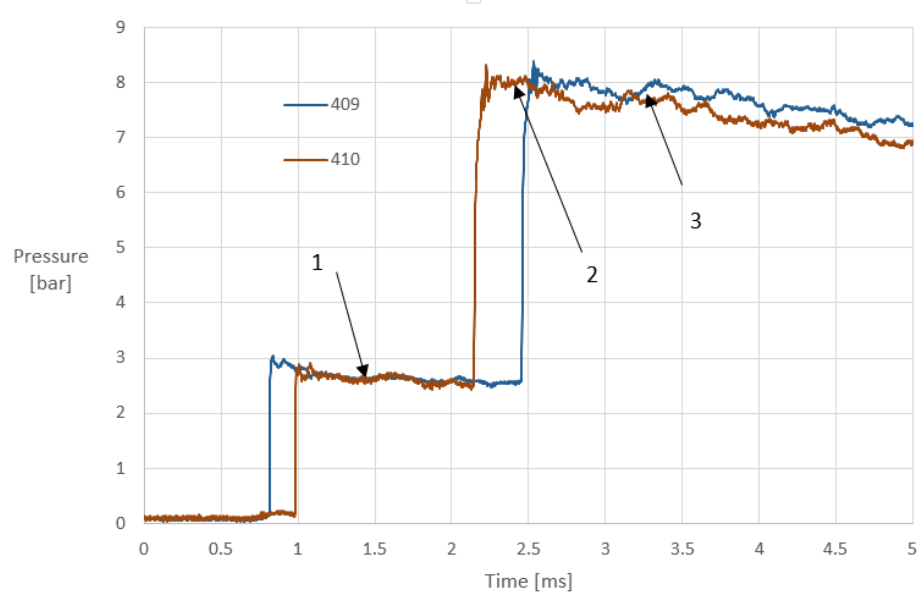

Fig. 64 Pressure-time history from the first part of the loading

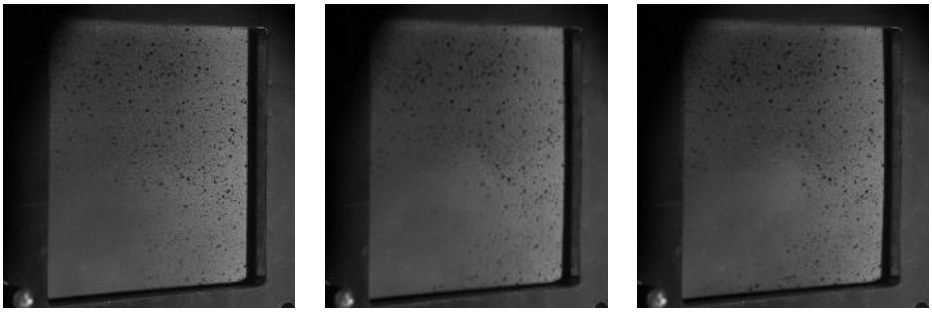

1, t=1.4595 ms 2, t=2.4603 ms 3, t=3.2943 ms

Fig. 65 DIC of the back plate at specific times for experiment ''420-1''

6.2.3 Summary

The experimental results are summarized in Table 12. The displacements of the back plate were measured manually with a caliper across a line through the middle of the plate.

Table 12 Results from the shock tube experiments

Test	Pressure [kPa]	Foam failure	Displacement at the back plate [mm]
210-1	1000	Complete failure	Failure
220-1	360	Small cracks	6
350-1a	440	No failure	--
350-1b	530	No failure	--
350-1c	590	Back surface cracks	2
420-1	860	Large cracks on both surfaces	16

When comparing the failure patterns of the different foam densities it is easy to conclude that for bending of clamped, plated foam structures, failure occurs almost at the same time as displacements initiate. It is known from the literature that tensile stresses in the foam will cause brittle failure of the material and these experiments supports these observations. Bending of the clamped foam plates causes tension in the front face along the boundaries and in the center of the back face. It is here that fracture in the foam occurs.

7 Numerical analyses

In order to evaluate a numerical model of the sandwich structure, analyses of the shock tube experiments have been performed in Abaqus/Explicit. It is performed analyses to check if the material model of foam is able to predict the behavior seen from the experiments. After the material model is evaluated, some parametric studies have been performed. First, a study on sandwich structures with equal mass compared to monolithic plates is performed. Then, concrete plates with an aluminum foam plate as a protective layer are analyzed.

7.1 Numerical model

In this part, the properties of the numerical model is described including geometry, boundary conditions, failure criterion and mesh configurations.

7.1.1 Geometry and boundary conditions

The numerical model consists of three parts. An aluminum foam core layer and aluminum sheet plates on the front and back surface of the core. The front is referred to as the surface/layer that is loaded in Fig. 66 and the back layer/surface is on the opposite side. The core is a three-dimensional deformable and homogeneous solid while the sheet plates are three-dimensional homogeneous shells. Clamped boundary conditions are applied along all edges. In the shock tube, the boundary conditions are assumed to be clamped, but in reality, a fully clamped structure is hard to obtain.

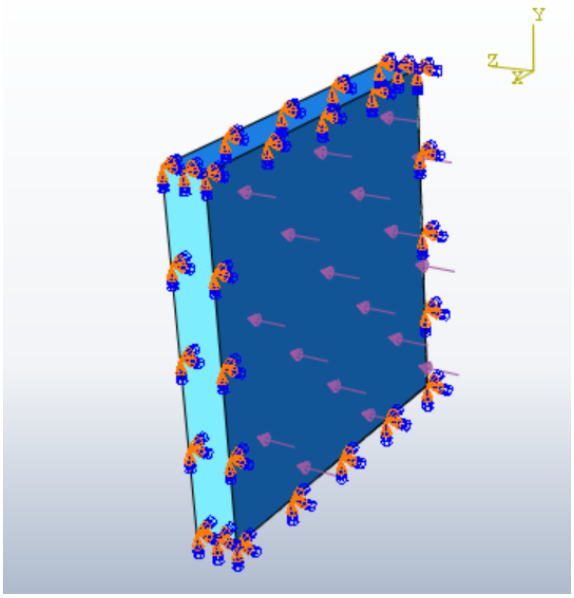

Fig. 66 Geometry of the model

7.1.2 Contact

In Abaqus/Explicit, the general contact algorithm is used for modelling the contact between the aluminum sheet plates and the aluminum foam core. This algorithm allows interaction between all bodies in the model. A single interaction defines contact between the regions in the model. The contact constraints are enforced through the Penalty method. This method is always used in Abaqus when general contact is applied and it is well suited for very general contact formulations. The penalty method adds some stiffness into the model, which can influence the stable time increment. The effect is usually small, but Abaqus/Explicit considers the effect automatically in the automatic time increment. A ''softened'' contact formulation is used with a linear pressure-overclosure relationship, frictional coefficient equal to 0.1 and contact stiffness equal to one.

7.1.3 Failure criterion

A failure criterion have been introduced in an attempt to model the failure mode of the foam in tension. In the analyses, a ductile damage criterion was introduced. This criterion requires a critical equivalent plastic strain to be specified and for the aluminum foam it was here assumed to be 0.2, which has been used previously by Reyes et al. [26].

7.1.4 Meshing

The numerical accuracy of the model was checked by refining the mesh and controlling the energy outputs. The different mesh configurations are shown in Table 13 together with the computational times. The total time of the analyses was set to 0.03 s with automatic time increments applied. The aluminum foam core was meshed with C3D8R elements while the sheet plates were modelled with shell elements of type S4R.

Table 13 Mesh sizes and CPU time

Seed	Elements in core	Elements in one sheet	CPU time
10	3600	900	10 min 56 sec
6	15000	2500	29 min 50 sec
4	56250	5625	1 t 45 min 30 sec

Because the density in the foam plates varies across the thickness, it was decided to introduce a grading of the density across the thickness in the model. A Matlab script created a graded density by specifying a maximum and minimum density and their coordinates. The Matlab script is found in Appendix D.

An example of how the density varies linearly across the thickness of the foam core is shown in Fig. 67 for the test specimen with average density 0.42 g/cm^3. A minimum value of the foam density was chosen as 0.30 and the maximum 0.52, giving an average value of 0.42. Due to the presence of the skin-type surface, the density at the front surface was uncertain.

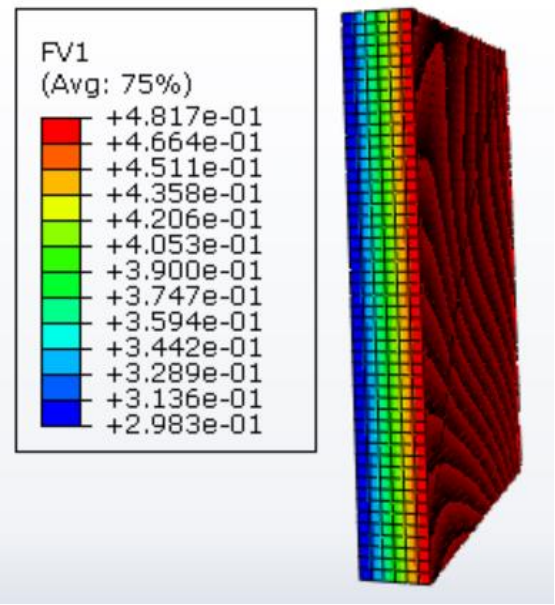

Fig. 67 Grading of the density through the thickness

In order to check the accuracy of the model and to choose the appropriate mesh configuration for the analyses, the amount of artificial strain energy were controlled to be much lower than the ''real'' strain energy. It is seen from Fig. 68 that the strain energy is almost the same for every mesh, while the amount of artificial strain energy is reduced when the mesh is refined.

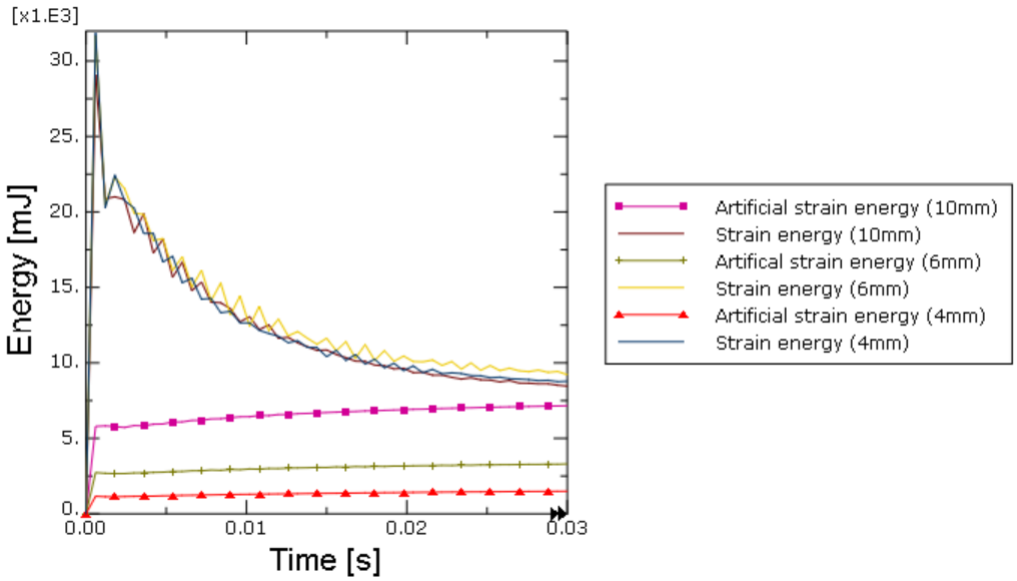

Fig. 68 Artificial strain energy vs strain energy for different meshes

The central displacement history of the back plate for the different meshes are shown in Fig. 69. It is seen that the displacement does not change much when changing the mesh. Based on these observations, the parts in the numerical model are seeded with 6 mm elements.

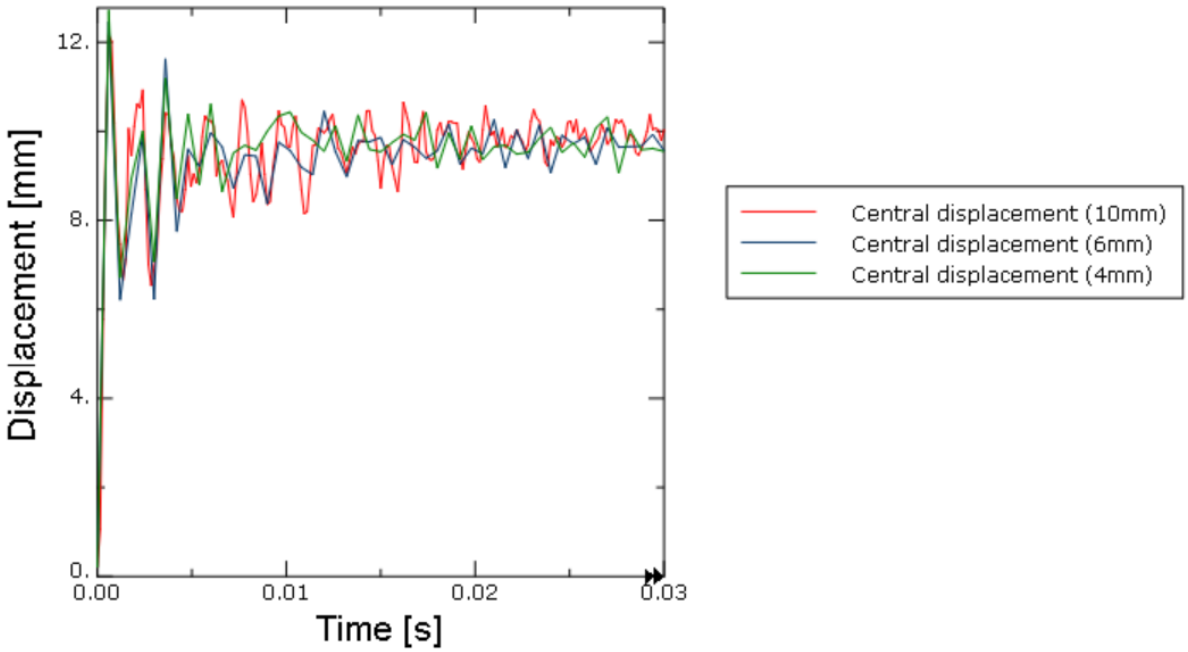

Fig. 69 Central displacement of the back plates for the different meshes

7.2 Analysis of the Shock Tube experiment

The shock tube experiments were analyzed numerically in Abaqus/Explicit. The results of these analyses are stated in this chapter and discussed later. The analyses were performed with graded core density and the results are compared against the experimental data. The ductile failure strain is chosen to be 0.2. First, the goal is to perform analyses similar to the shock tube experiment. The density is highest towards the front plate for experiments ''350-1a,b,c'' and ''420-1'' and opposite for experiments ''210-1'' and ''220-1''. The density is varying linearly through the aluminum foam core. This is an assumption and in reality, the grading is probably not linear, but will be somewhat nonlinear towards the surface. We can see this by looking at the surface of the foam.

The parts are seeded with 6 mm elements, which gives 15000 C3D8R elements in the core and 2500 S4R elements in the aluminum sheets. The total time of the analysis were 0.03 s although the duration of the positive phase of the shock waves were in the range of 0.04-0.06 s. This simplification is done to reduce computational time of the analyses and is justified by the fact that the results are mostly dependent on the peak reflected overpressure.

The analyses are presented in the same succession as the experiments were performed. Table 14 gives an overview of the densities and detailed description of the loading curves based on the Friedlander function in eq. (26). The experiment ''420-1'' is studied in more detail because quite large displacements of the aluminum back plate and clearly visible failure pattern in foam were observed in this experiment.

Table 14 Densities and loading histories for the experiments

Experiment	Min density [g/cm^3]	Max density [g/cm^3]	P_r [kPa]	t_+ [ms]	b
210-1	0.18	0.24	1000	60	2.6
220-1	0.18	0.26	360	34	1.6
350-1a	0.28	0.42	460	38	1.8
350-1b	0.28	0.42	530	40	1.8
350-1c	0.28	0.42	590	42	1.8
420-1	0.30	0.52	860	57	2.5

7.2.1 Experiment ''210-1''

The results from the numerical analysis of experiment ''210-1'' are shown in Fig. 70 and displays failure in both the foam and aluminum plates. The failure initiates at the boundary of the foam and the aluminum plates are punched out with a failure pattern as in increment 956 in the figure.

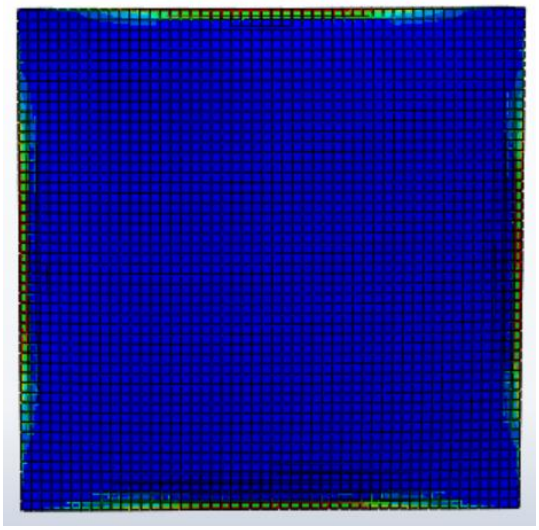

Increment 318, t=0.00030072 s

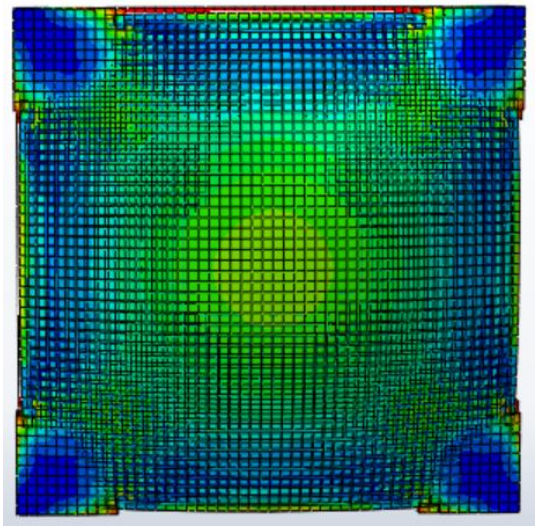

Increment 635, t=0.00060028 s

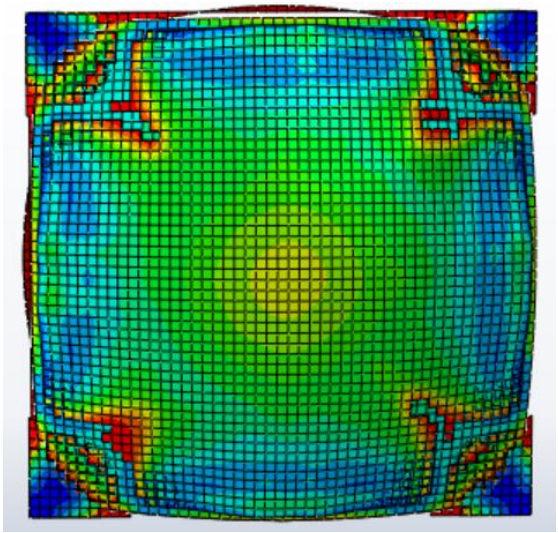

Increment 956, t=0.00090022 s

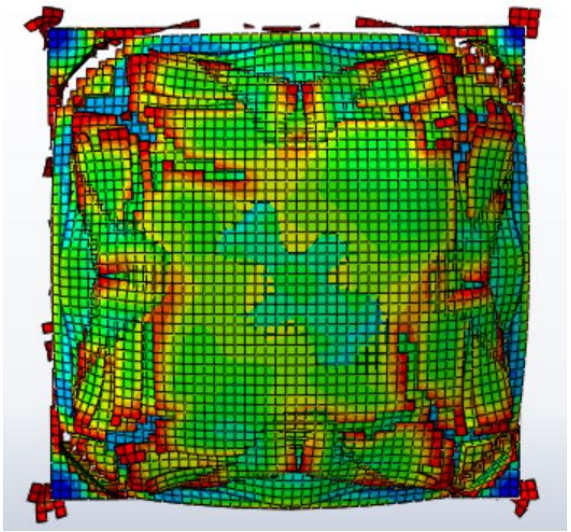

Increment 1279, t=0.0012002 s

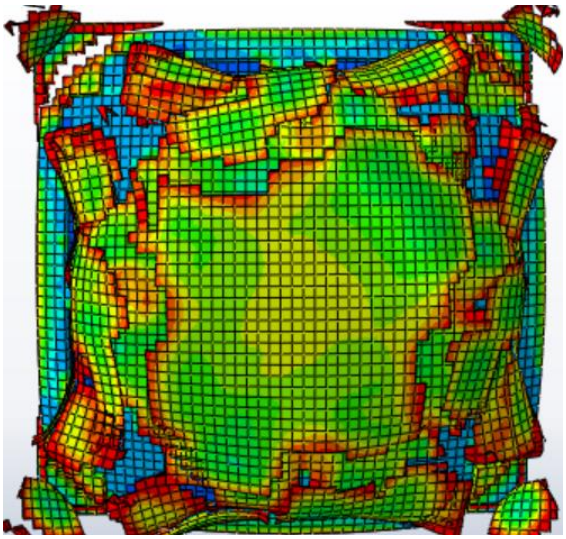

Increment 1610, t=0.0015007

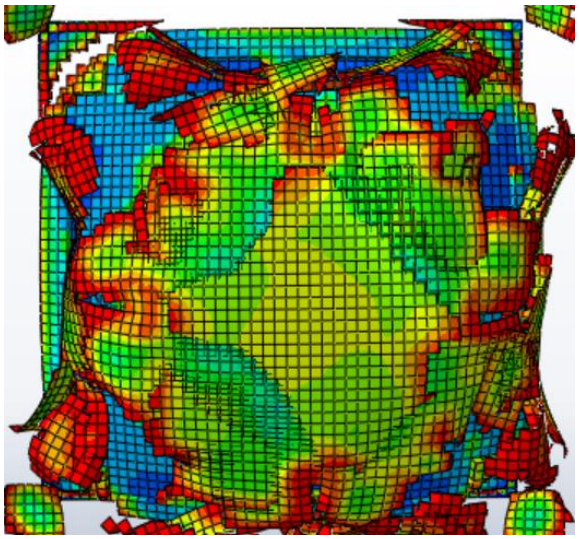

Increment 1936, t=0.0018003 s

Fig. 70 Failure of experiment ''210-1''

7.2.2 Experiment ''220-1''

Fig. 71 shows the distribution of displacements at the back plate for experiment ''220-1''. The displacement at the midpoint was 13.7 mm after 0.03 s.

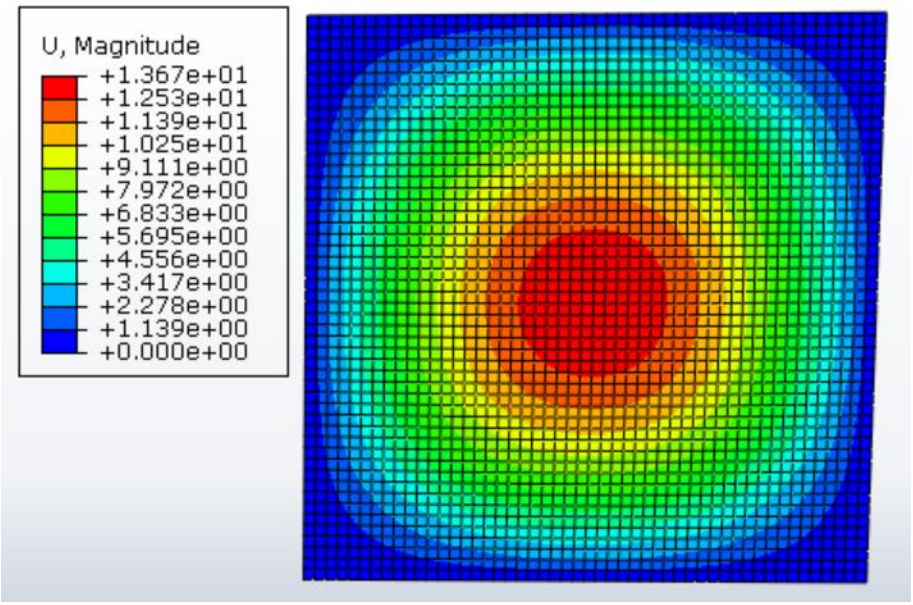

Fig. 71 Displacement of the back plate after 0.03 s

Fig. 72 shows how the equivalent plastic strain is distributed in the aluminum foam after 0.03 s. The failure criterion has been reached at the middle of the boundary on both sides and thus elements has been deleted from the mesh.

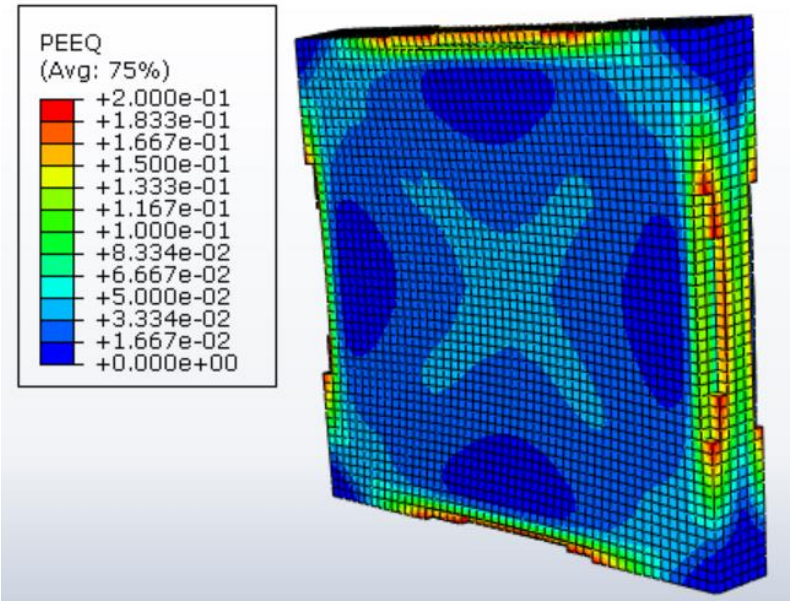

Fig. 72 Equivalent plastic strain for experiment ''220-1''

7.2.3 Experiment ''350-1a, b, c''

The loading history for experiments ''350-1a, b, c'' differs from the other experiments in some extent because there were performed three experiments on the same plate with different pressures. This is because the plate seemed unaffected by the applied loads. Plots of the equivalent plastic strain in the aluminum foam core for the first and last load case are included in Fig. 73 and Fig. 74. The failure criterion is not exceeded in any of the load cases. For the load case with peak reflected overpressure P_r*=440 kPa*, the equivalent plastic strain is equal to 0.049 and when P_r is increased to *590 kPa*, it increases to 0.104.

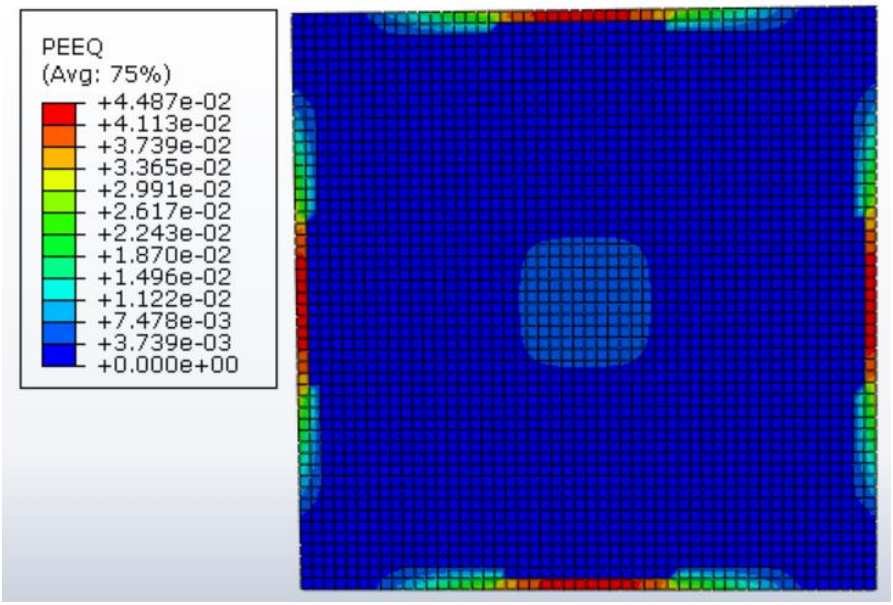

Fig. 73 Equivalent plastic strain in the foam core for experiment ''350-1a'' with Pr=440 kPa

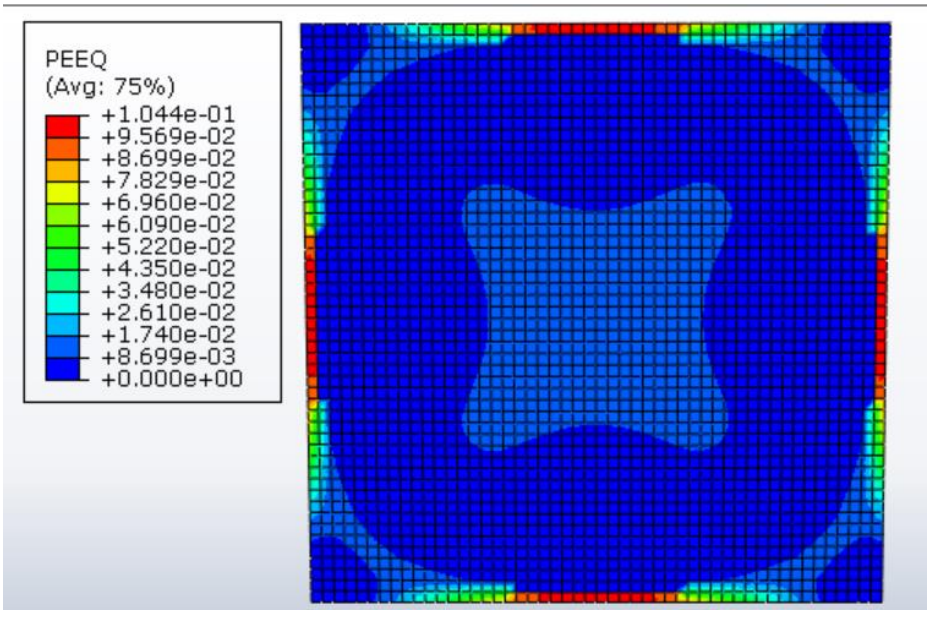

Fig. 74 Equivalent plastic strain in the foam core for experiment ''350-1c'' with Pr=590 kPa

7.2.4 Experiment ''420-1''

The loading curve for experiment ''420-1'' is shown in Fig. 75. The measured pressure-time histories from pressure sensors 409 and 410 are compared with the curve from the Friedlander equation.

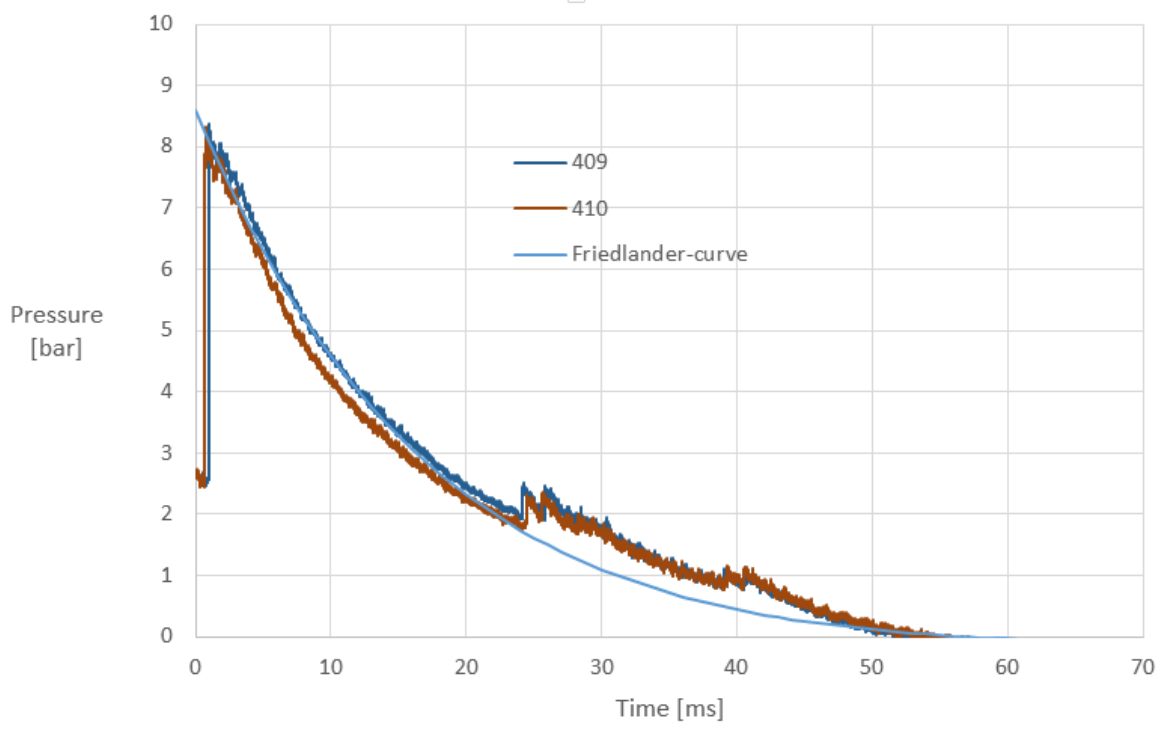

Fig. 75 Pressure-time history for experiment ''420-1''

In Fig. 76, the displacement history from the midpoint of the back plate is shown. The plot indicates a permanent displacement at the back plate of approximately 10 mm.

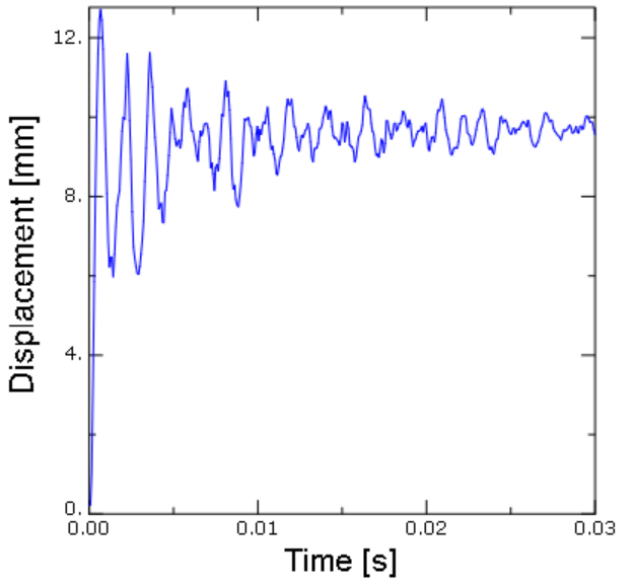

Fig. 76 Displacement history at the midpoint of the back plate

Fig. 77 shows the back plate displacements in a contour plot. The displacement pattern looks like it is a merge between a rectangular and circular one.

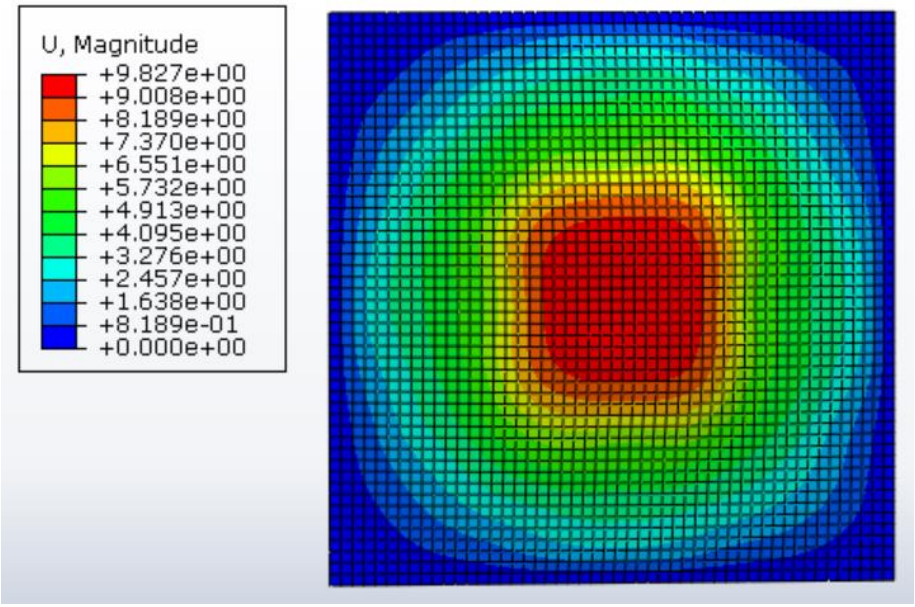

Fig. 77 Distribution of the displacement at the back plate for experiment ''420-1''

The equivalent plastic strain for experiment ''420-1'' is shown in Fig. 78 and indicates a maximum value of 0.141 at the boundary with lowest density as previously observed.

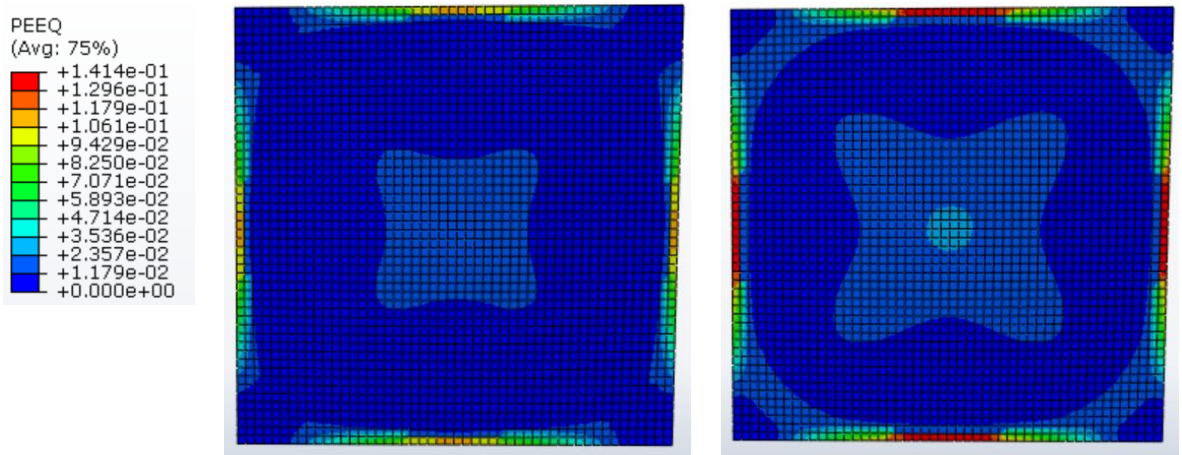

Increment 688, t=0.0003754 s Increment 55518, t=0.03 s

Fig. 78 Equivalent plastic strain of foam core for experiment ''420-1''

Fig. 79 shows the von Mises stresses at the front surface of the foam, while Fig. 80 shows the stresses at the back surface. The von Mises stresses at the front surface and back surfaces are compared with the initial plateau stresses for the aluminum foam densities at the respected

surface. The densities at the surfaces are 0.30 g/cm^3 and 0.52 g/cm^3 and initial plateau stresses are 3.027 MPa and 12.238 MPa for these foam densities. From Fig. 79 it is seen that the maximum stress is a bit lower than the plateau stress in the front surface, while the stress is larger than the initial plateau stress at the back surface in Fig. 80.

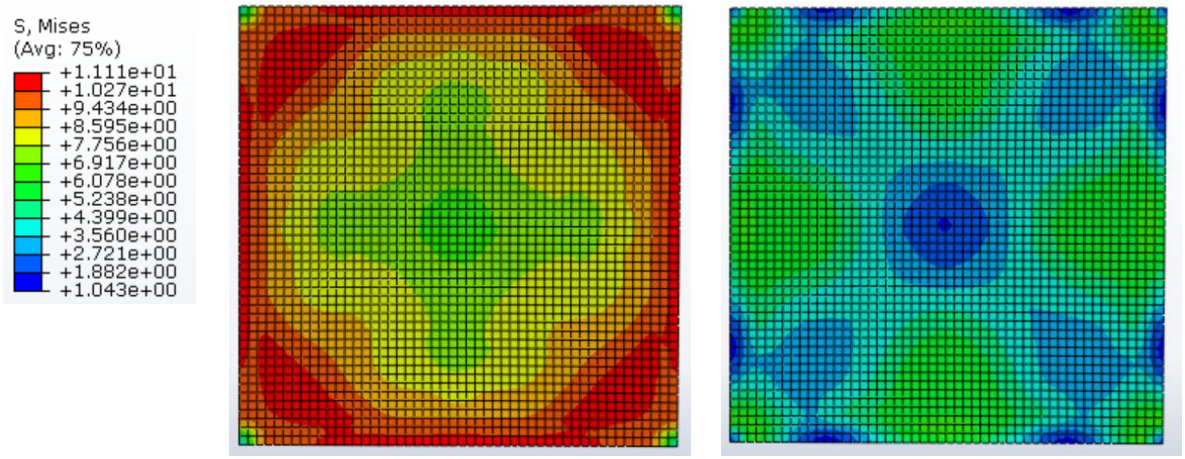

Increment 1381, t=0.000750 s Increment 55518, t=0.03 s

Fig. 79 Von Mises stresses at the front surface of the foam core

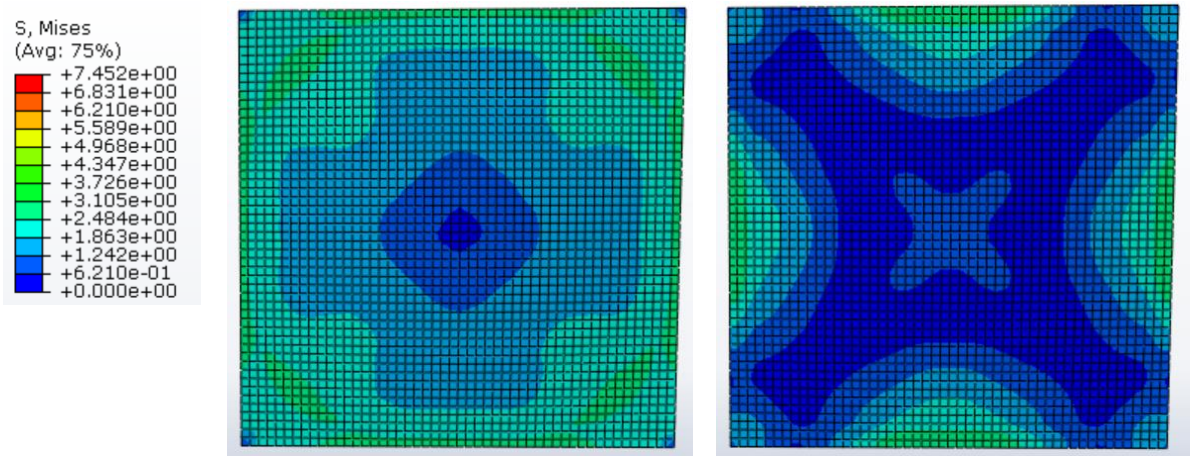

Increment 1382, t=0.000750 s Increment 55518, t=0.03 s

Fig. 80 Von Mises stresses at the back surface of the foam core

To investigate when failure occurs in the model the loading were increased gradually on the sandwich structure from experiment ''420-1''. The loading curves were approximated because no calibration tests were done with such high pressures. A typical blast loading curve were used with larger values for the peak reflected overpressures and duration times. The load cases are shown in Table 15 and the equivalent plastic strains for each load case are compared in Fig. 81. It is observed that failure initiates in the model when the pressure is increased to 1000 kPa, but total failure does not occur until the peak reflected overpressure reaches 1200 kPa.

Table 15 Peak reflected overpressures and positive phase duration

P_r [kPa]	t_+ [ms]
860	55
1000	60
1100	65
1200	70

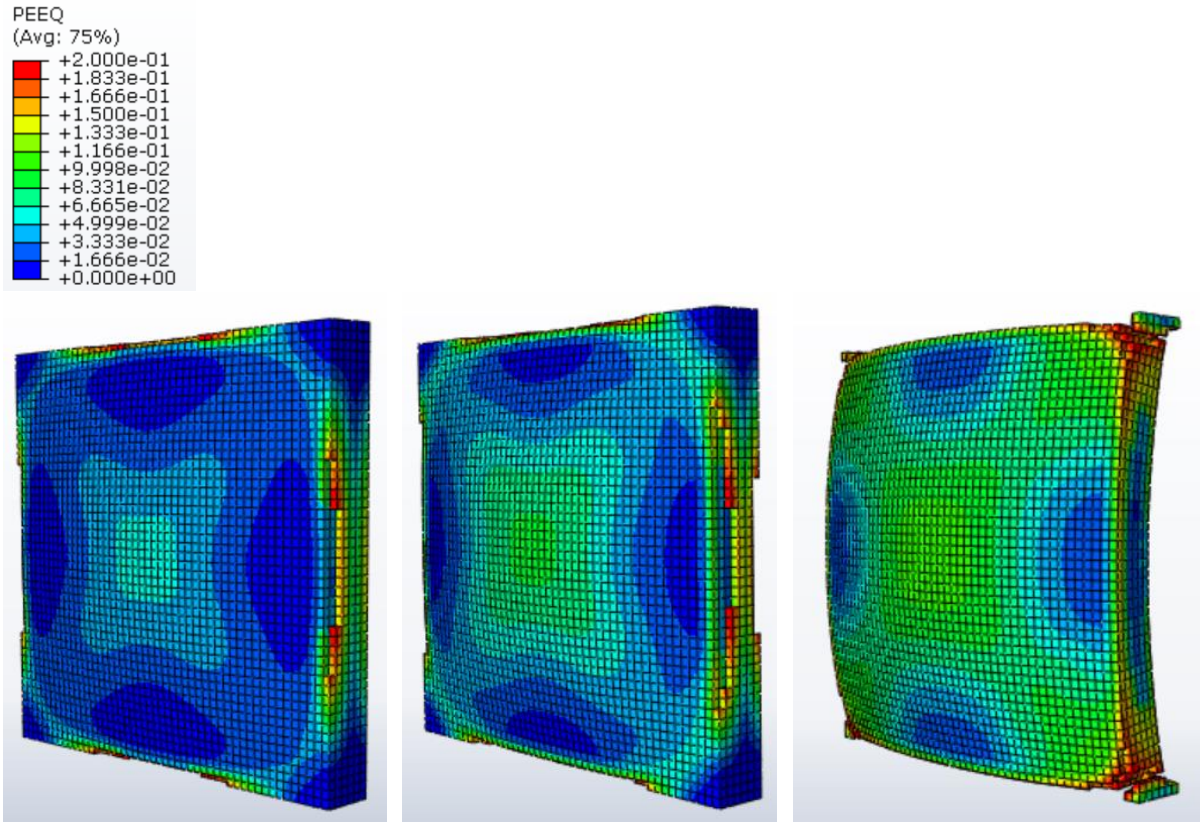

P_r = 1000 kPa P_r = 1100 kPa P_r = 1200 kPa

Fig. 81 Equivalent plastic strains of foam core for different pressure-time histories

7.2.5 Summary

Table 16 summarizes the results from the numerical analyses of the shock tube experiments and it is seen that the numerical model is able to simulate the experiments in some extent. The displacements shown here are the values at the end of the analyses at 0.03 s. The displacements were not measured after experiment ''350-1a'' and ''350-1b'' because no failure in the foam was observed. For test ''420-1'', some failure was observed from the experiments, but not in the numerical analysis.

Table 16 Results from the numerical analyses of the shock tube experiments

Test	Pressure [kPa]	Numerically [mm]	Experimentally [mm]	Failure Y/N
210-1	1000	F	F	Yes
220-1	360	13.7	6	No
350-1a	440	3.3	--	No
350-1b	530	5.4	--	No
350-1c	590	7.5	2	No
420-1	860	9.8	16	Some

7.3 Parameter studies

7.3.1 Equivalent thickness study

A numerical investigation on sandwich plates with equivalent thickness of the aluminum foam core to compare with monolithic aluminum plates were done. For comparison, a monolithic aluminum plate with 4 mm thickness were chosen. Then, in order to achieve a sandwich structure with equivalent mass, the aluminum sheet plates were 0.8 mm and the density of the aluminum foam core was chosen to be 0.35 g/cm^3. Now, the thickness of the aluminum foam core were the only variable to change to make the masses equal. The thickness of the foam core then became 18.5 mm. The material properties of the 4 mm monolithic plate were assumed the same as that for a 2 mm monolithic plate. The foam density varied linearly across the thickness and the effect of the position of the maximum density were also investigated by changing the direction of the grading.

Since the foam density chosen were 0.35 g/cm^3, the load cases were chosen to be the same as when testing in the shock tube for the same density. In addition, two more load cases were considered to achieve a clearer view of the effect of the foam for a wider range of pressures. No failure criterion were used when comparing the structures because of the uncertainties regarding the accuracy of the criterion experienced from analyzing the shock tube experiments. A softened linear pressure-overclosure contact relationship was used. For reference, a 2 mm monolithic aluminum plate were also analyzed for because experimental data from shock tube experiments existed for this plate. In Table 17, the results from the analyses are collected to show the difference in displacement for each load case. The relation between the pressure and maximum displacement in the plates is shown in Fig. 82.

Table 17 Results from analyzing equivalent thickness sandwich structures in [mm]

P_r [kPa]	Equivalent sandwich plate	Equivalent sandwich plate with inverted density grading	Monolithic 4 mm aluminum plate	Monolithic 2 mm aluminum plate for reference
300	13	12.5	9.5	19.5
440 (350-1a)	20	20	13	27
530 (350-1b)	24	24	16	34
590 (350-1c)	27	27	17	38
700	33	33	20.5	46

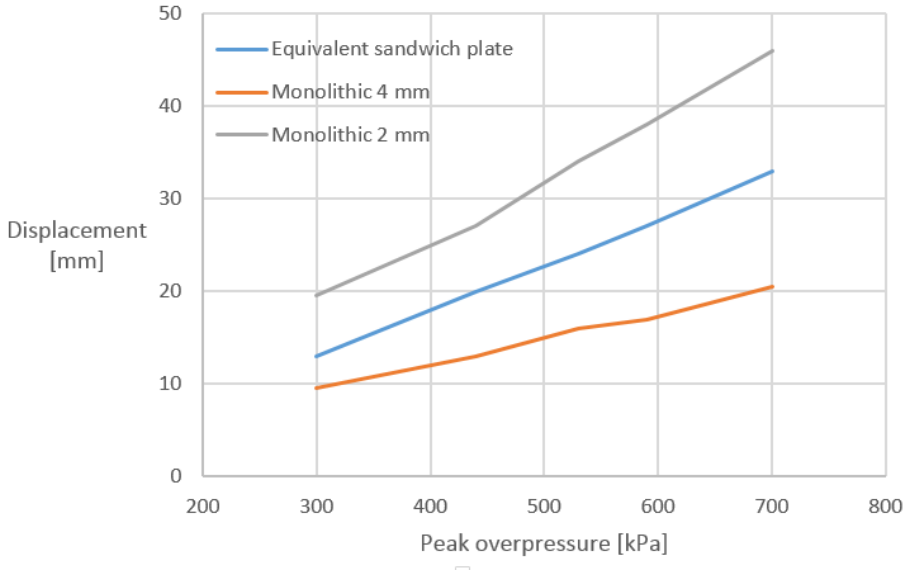

Fig. 82 Maximum midpoint displacement against peak overpressure for each model

The results shows that the relationship between the midpoint displacement in the plate and the peak overpressure is almost linear for all the structures analyzed, but with different slopes. In the research performed by Wadley et al. [16] on sandwich structures with triangular corrugated core, it was observed that the central displacement increased exponentially when reducing the stand-off distances. Such a phenomenon is not observed here, but only one density have been tested. In order to get a full understanding of the effect of the sandwich structure with aluminum foam core, more analyses should be performed including a wider range of densities, core thicknesses and sheet plate thicknesses.

Another important note is that there is no failure criterion in the model and this might lead to uncertainties when increasing the peak overpressure to values close to and above the capacities of the structures analyzed. When comparing the displacement in the plates, it is seen that a 4 mm monolithic aluminum plate performs better than the equivalent sandwich structure with aluminum foam core. The sandwich structure behaves better than a 2 mm monolithic aluminum plate, but the mass of the aluminum plate is half the mass of the foam structure.

7.3.2 Isotropic concrete plate with an aluminum foam layer

A numerical analysis of an aluminum foam plate as a cladding on a concrete plate were done to investigate the effect. The model was made as a shock tube experiment with the same geometry and boundary conditions as in the shock tube. The thickness of the concrete part were chosen to be 100 mm. The concrete were for simplicity modelled as an isotropic, elastic material because the behavior of the concrete itself were not important. The contact between the concrete part and the aluminum foam part were done with both ''hard'' contact and a softened linear pressure-overclosure relationship with contact stiffness equal to 1. The peak reflected overpressure chosen for this analysis were 2000 kPa and the positive time duration were 0.1 s.

The results from the analysis shows that the effect of adding aluminum foam on concrete is questionable. In Fig. 83, the maximum logarithmic strain is plotted against time for the three models. It is seen that when considering a concrete plate alone the maximum strain reached is the same as when adding an aluminum foam layer and using a hard contact formulation. When a softened linear pressure-overclosure relationship is used, the strains increases when adding an aluminum foam layer.

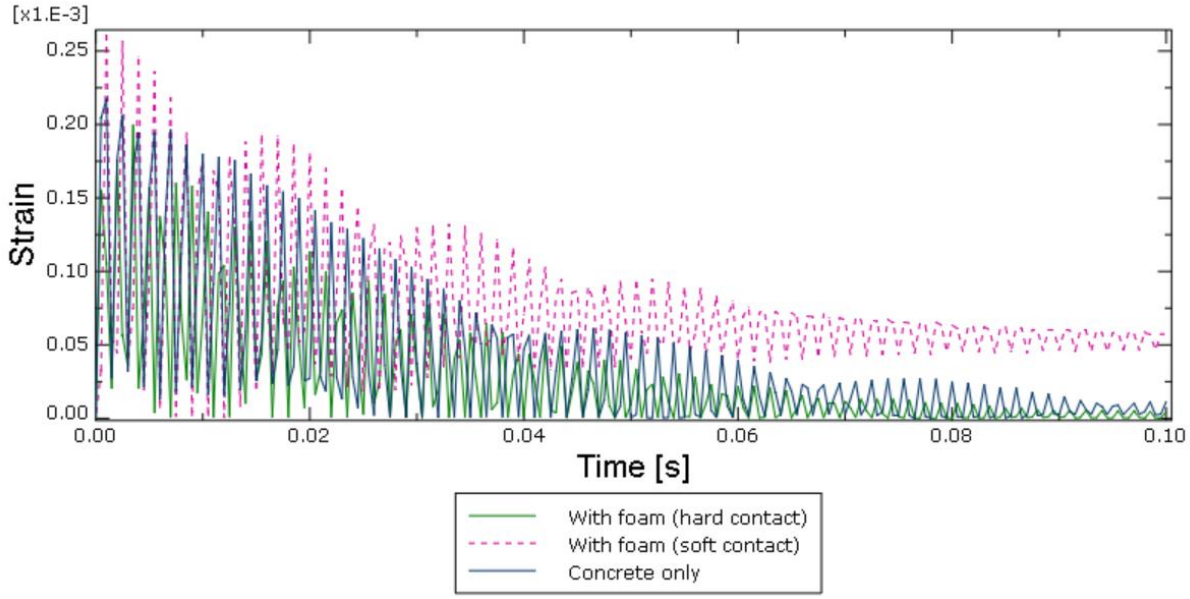

Fig. 83 Maximum logarithmic strains in the concrete

8 Discussion

The stiffness of the test specimens in the shock tube experiments became large because of the clamped boundary conditions. Consequently, it was difficult to determine a suitable pressure on the test specimens. In addition, since the shock tube is a quite new facility at SIMLab, there were not enough knowledge about the response on clamped plates from a shock loading. As a result, it was decided to do experiments on sandwich plates with aluminum foam core instead of aluminum foam plates in front of concrete plates.

When testing the sandwich structures with aluminum foam core, it was observed failure in the foam simultaneously as displacements were initiated. The experiments were successful because they showed how aluminum foam plates behaves in a shock tube. Clearly visible failure patterns on both sides of the foam core illustrated the propagation of failure in the foam for clamped boundary conditions.

The behavior of aluminum foam with clamped boundary conditions proved to introduce this type of failure. This may be due to the tension forces from the bending of the plate. If simply supported boundary conditions were used instead, different results would be expected. However, we would still get bending and tensile stresses in the foam. A method for applying simply supported boundary conditions do not exist in the shock tube facility at the time, but for investigating the behavior of aluminum foam further, simply supported conditions would be an interesting investigation.

Another aspect of the shock tube experiments that should be discussed is the type of structure used in the experiments. It might be that changing the thickness of both the aluminum foam core and the sheet plates would influence the results somehow. In addition, the density of the aluminum foam core may influence the results in one way or another.

It was assumed that the crushable foam model in Abaqus/Explicit could describe the behavior of the aluminum foam in a preferable manner by utilizing uniaxial compression tests of the foam. The modelling of the foam as a solid material may introduce some errors in the solution. The use of a simple ductile damage failure criterion might not be able to simulate the failure of the aluminum foam exactly because of the uncertainty in the actual failure strain of the foam in tension.

In addition, the simple approach of modelling the behavior of the aluminum sheet plates with a simple bilinear curve may lead to some unwanted effects in the transition to the plastic region. This may lead to uncertainties regarding how and when failure in the material appears. The contact formulation used may have introduced some errors due to the uncertainty regarding the contact between the aluminum sheet plates and foam core.

The comparison between the experimental analyses in the shock tube and the numerical analyses done in Abaqus/Explicit shows that there are some uncertainties regarding the accuracy of the numerical model. First, the failure pattern of the aluminum foam core observed from the shock tube experiments was not obtained in the numerical model. It was clear that the ductile damage criterion used did not exactly represent the real failure in the foam. In the numerical analysis of experiment ''210-1'' it was observed failure at the boundary before elements were removed at the middle of the back surface as well, but the failure pattern from experiments ''220-1'', ''350-1c'' and ''420-1'' were not obtained in the numerical calculations of these experiments.

The measured displacements at the back plate are shown in Table 16 in chapter 7.2.5. The results for experiment ''220-1'' showed larger displacements in the numerical model compared to the experiment, while for experiment ''420-1'' the displacement were smaller in the numerical analysis. In experiments ''350-1a, b, c'', the displacements were quite small for both the numerical analysis and the experiment. This observation indicates that for low densities, the numerical model is conservative, but when the foam density increases, the numerical solution tends to become non-conservative. An important note is that only one experiment on each foam density have been done and since the variations in the foam are quite large, this might simply be because of natural variation in the materials. Another reason for this strange relationship between the density and accuracy of the numerical model could be that there are some small inaccuracies in the calibrated material model that makes the material weaker for low densities and stronger as the density increases. More uniaxial compression tests with a wider range of densities could be performed in order to achieve a more accurate dependency on the foam density. There have not been performed uniaxial compression tests for densities larger than 0.27 g/cm^3, so the material properties for densities larger than this is only assumed based on uniaxial tests on low-density test specimens.

From the analytical calculation, the displacements did not even reach 1 mm for a static pressure of 1100 kPa and compared with the experimental and numerical calculations, the calculated displacements based on the analytical estimate is not correct. The reason for this is probably that the assumption of thin-plate theory on the foam plate is not well suited for calculating displacements. In addition, the applied pressure were static and not dynamic, so there is probably some dynamic effects that makes the solution inaccurate. However, the stresses from the analytical calculations are comparable with experimental tests and numerical analyzes. It is assumed that the stresses calculated analytically represent a rough estimation of the stresses present in the aluminum foam during experimental tests in the shock tube.

From the parameter studies, it was observed that an equivalent sandwich structure did not perform better than a monolithic plate of equal mass. The same inaccuracies in the numerical model as for the numerical analyses of the shock tube experiments may be present for the parameter study. Another possible source of error is that the material properties of the 4 mm monolithic plate is assumed equal to the properties of a 2 mm aluminum plate.

The numerical analyses of concrete plates with an aluminum foam layer is rather simplified. The material properties of the concrete material itself is modelled as an elastic, isotropic material, but the foam material is the same as for the other analyses.

9 Conclusion

Experimental and numerical analyses of sandwich structures with aluminum foam core subjected to shock loading have been performed. Uniaxial compression tests were used to obtain the material properties for the aluminum foam. The numerical analyses were compared to the experimental results and differences were discussed. Additional numerical analyses were performed to investigate equivalent sandwich plates to monolithic plates. Finally, numerical analyses with an aluminum foam layer on a concrete plate were performed.

Increased knowledge about the failure patterns of aluminum foam for the boundary conditions applied and loading conditions as in the shock tube has been obtained. The numerical analyses were able to simulate the shock tube experiments with limited accuracy, but, not too far off for some of the experiments. There was observed failure in the numerical model, but at slightly different pressures than in the experiments.

From the equivalent thickness study, an equivalent sandwich structure did not perform better than a monolithic plate of the same mass for the parameters chosen in this study. For the chosen properties in the numerical model with concrete and aluminum foam, adding an aluminum foam layer did not reduce the response in the plate.

Aluminum foam is a lightweight material that should be possible to utilize in some sort, but for the configurations considered in this thesis, the effect of the foam was limited.

10 Further work

This thesis investigates the behavior of aluminum foam in the shock tube facility in some extent, but further investigation is needed to increase the knowledge of aluminum foam properties for a wider range of densities and thicknesses. Some of the topics that could be interesting to investigate further are:

- Changing the boundary conditions in the shock tube from clamped to simple supports to investigate the effect. Also, perform numerical analysis with different geometries and boundary conditions.
- Perform tests in the shock tube with an aluminum foam layer on concrete plates at a pressure that makes the concrete crack to investigate the effect experimentally.
- Improve the failure criterion in the numerical model so that it is more similar to the real experiments.
- Improve the accuracy of the numerical model both for the aluminum foam and using a plastic material model for the concrete.
- An interesting study would be to model the cell structure of the foam more precisely by either taking close-up pictures of the cell structures and converting it into a computer program, or by creating a Voronoi diagram to make an irregular cell sized mesh. The effect of modelling the cell walls as shell elements could also have been interesting.
- Investigate different core configurations of the core layer in the sandwich structures such as honeycombs in the shock tube to compare with a sandwich structure with aluminum foam core.

References

1. Norwegian Public Roads Administration *Project Overview Coastal Highway Route E39*. 2012.
2. Norwegian Public Roads Administration *Component: Fjord Crossings*. 2012.
3. Goup, R.O.O., *Possibility Study of crossing the Sognefjord, Submerged Floating Tunnel (in Norwegian)*. 2013.
4. Hanssen, A.G., L. Enstock, and M. Langseth, *Close-range blast loading of aluminium foam panels.* International Journal of Impact Engineering, 2002. **27**(6): p. 593-618.
5. Schenker, A., et al., *Full-scale field tests of concrete slabs subjected to blast loads.* International Journal of Impact Engineering, 2008. **35**(3): p. 184-198.
6. Wu, C., L. Huang, and D.J. Oehlers, *Blast testing of aluminum foam-protected reinforced concrete slabs.* Journal of Performance of Constructed Facilities, 2011. **25**(5): p. 464-474.
7. Zhu, F., et al., *Structural response and energy absorption of sandwich panels with an aluminium foam core under blast loading.* Advances in Structural Engineering, 2008. **11**(5): p. 525-536.
8. Liu, H., et al., *Performance of aluminum foam-steel panel sandwich composites subjected to blast loading.* Materials and Design, 2013. **47**: p. 483-488.
9. Zhang, L., et al., *Dynamic response of corrugated sandwich steel plates with graded cores.* International Journal of Impact Engineering, 2014. **65**: p. 185-194.
10. Yazici, M., et al., *Experimental and numerical study of foam filled corrugated core steel sandwich structures subjected to blast loading.* Composite Structures, 2014. **110**(1): p. 98-109.
11. Wadley, H.N.G., et al., *An active concept for limiting injuries caused by air blasts.* International Journal of Impact Engineering, 2010. **37**(3): p. 317-323.
12. Wadley, H.N.G., et al., *Impact response of aluminum corrugated core sandwich panels.* International Journal of Impact Engineering, 2013. **62**(0): p. 114-128.
13. Liu, T., H.N.G. Wadley, and V.S. Deshpande, *Dynamic compression of foam supported plates impacted by high velocity soil.* International Journal of Impact Engineering, 2014. **63**(0): p. 88-105.
14. Park, S., et al., *Dynamic compressive response of composite square honeycombs.* Composites Part A: Applied Science and Manufacturing, 2012. **43**(3): p. 527-536.
15. St-Pierre, L., N.A. Fleck, and V.S. Deshpande, *The dynamic indentation response of sandwich panels with a corrugated or Y-frame core.* International Journal of Mechanical Sciences, 2015. **92**(0): p. 279-289.
16. Wadley, H.N.G., et al., *Deformation and fracture of impulsively loaded sandwich panels.* Journal of the Mechanics and Physics of Solids, 2013. **61**(2): p. 674-699.
17. Lubliner, J., *Plasticity theory*. 2006, University of California at Berkeley.
18. Chen, Y., et al., *Stress-strain behaviour of aluminium alloys at a wide range of strain rates.* International Journal of Solids and Structures, 2009. **46**(21): p. 3825-3835.
19. Hanssen, A.G., et al., *Validation of constitutive models applicable to aluminium foams.* International Journal of Mechanical Sciences, 2002. **44**(2): p. 359-406.
20. Olurin, O.B., N.A. Fleck, and M.F. Ashby, *Deformation and fracture of aluminium foams.* Materials Science and Engineering A, 2000. **291**(1-2): p. 136-146.
21. Deshpande, V.S. and N.A. Fleck, *High strain rate compressive behaviour of aluminum alloy foams.* International Journal of Impact Engineering, 2000. **24**(3): p. 277-298.
22. Reid, S.R. and C. Peng, *Dynamic uniaxial crushing of wood.* International Journal of Impact Engineering, 1997. **19**(5–6): p. 531-570.
23. Miller, R.E., *Continuum plasticity model for the constitutive and indentation behaviour of foamed metals.* International Journal of Mechanical Sciences, 2000. **42**(4): p. 729-754.
24. Schreyer, H.L., Q.H. Zuo, and A.K. Maji, *Anisotropic plasticity model for foams and honeycombs.* Journal of Engineering Mechanics, 1994. **120**(9): p. 1913-1930.

25. Deshpande, V.S. and N.A. Fleck, *Isotropic constitutive models for metallic foams.* Journal of the Mechanics and Physics of Solids, 2000. **48**(6): p. 1253-1283.
26. Reyes, A., et al., *Constitutive modeling of aluminum foam including fracture and statistical variation of density.* European Journal of Mechanics, 2003. **22 (2003)**.
27. Baker, W.E., *Explosion hazards and evaluation*. 1983, Amsterdam: Elsevier.
28. Bjerketvedt, D., J.R. Bakke, and K. Van Wingerden, *Gas explosion handbook.* Journal of Hazardous Materials, 1997. **52**(1): p. 1-150.
29. Børvik, T., et al., *Response of structures to planar blast loads - A finite element engineering approach.* Computers and Structures, 2009. **87**(9-10): p. 507-520.
30. Baker, W.E., *Explosions in Air*. 1983, San Antonio: Wilfred Baker Engineering.
31. Kingery, C.N. and G. Bulmash, *Airblast parameters from TNT spherical air bursts and hemispherical surface bursts*, A. US Army Ballistic Research Laboratory, Aberdeen Proving Ground, Editor. 1984, Defence Technical Information Center: Maryland.
32. Aune, V. and T. Børvik, *Submerged Floating Tunnel E39, Vulnerability Assessment - Explosion inside tunnel*, SIMLab, Editor. 2014, Department of structural engineering, NTNU: Trondheim.
33. Cook, R.D., et al., *Concepts and applications of finite element analysis*. 4 ed. 2002, United States: John Wiley & Sons, INC.
34. *Abaqus Manual 6.13*.
35. Mathisen, K.M., *Lectures in Nonlinear Finite Element Analysis at NTNU, Autumn 2014*.
36. Aune, V., T. Børvik, and M. Langseth, *Behaviour of plated structures subjected to blast loading.* 2015.
37. Brun, R., *Shock tubes and shock tunnels: design and experiments*. 2009, DTIC Document.
38. H. J. Davis, H.D.C., *Shock Tube Techniques and Instrumentation*. 1969, U.S. Army Materiel Command. Harry Diamond Laboratories: Washington D. C.
39. Downes, S., A. Knott, and I. Robinson, *Towards a shock tube method for the dynamic calibration of pressure sensors*. Vol. 372. 2014.
40. Fagerholt, E., *Field Measurements in Mechanical Testing Using Close-Range Photogrammery and Digital Image Analysis*. 2012, NTNU.
41. Standard Norge, *NS-EN 12390*. 2009.
42. Cook, R.D. and W.C. Young, *Advanced Mechanics of Materials*. 1999, Prentice-Hall, Inc.

Appendix A

Air blast parameters with scaled distance.

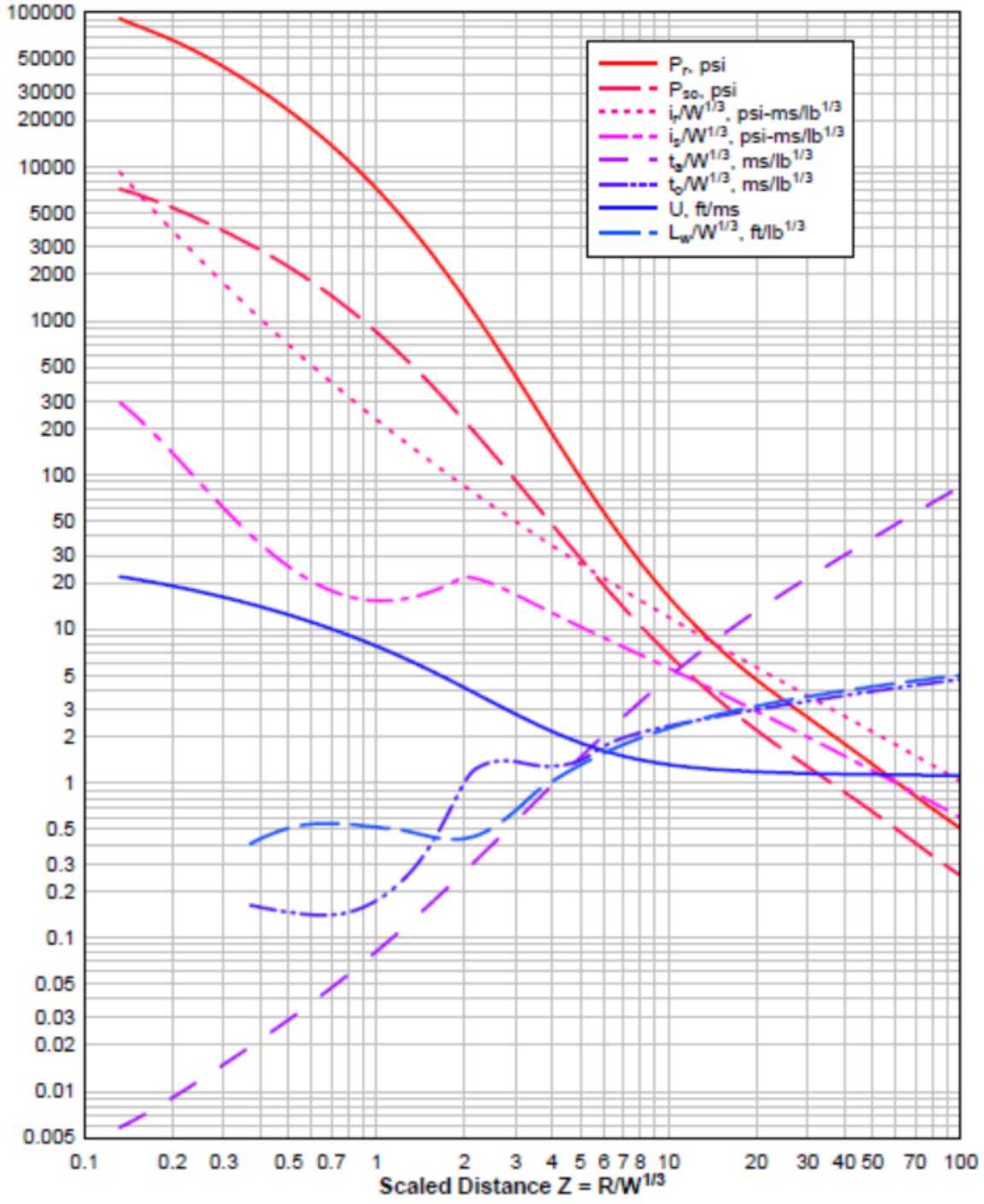

Appendix B

Configurations of diaphragms in the shock tube.

Thickness[mm]	1	2	3	4	5	Comments
0,125	1,562	1,583	1,605	1,587	1,605	Single
0,19	2,136	2,1	2,094	2,072	2,078	Single
0,25	3,01	2,936	2,969	2,905	2,921	Single
0,25	3,143	3,03	3,15	3,037	3,116	0,125+0,125
0,315	3,64	3,638	3,623	3,629	3,641	0,125+0,19
0,38	4,116	4,132	4,117	4,11	4,117	0,19+0,19
0,44	4,92	4,999	5,046	4,984	4,956	0,19+0,25
0,5	4,397	4,315	4,343	4,282	4,343	Single
0,5	6,067	5,899	5,914	5,85	5,933	0,25+0,25
0,69	6,485	6,546	6,525	6,381	6,696	0,19+0,5
0,75	7,193	7,056	7,205	7,208	7,178	0,25+0,5
1	8,88	8,652	8,667	8,615	8,637	0,5+0,5

Appendix C

Hydro Aluminium
Rolled Products

NO 10476I
ASTRUP A.S
HAAVARD MARTINSENS VEI 34
0978 OSLO
Norway

Inspection Certificate no: KRM 101575 - 6

According to EN 10204 - 3.1.

Date : 06/02/2014 Page : 1

Customer order no	: 1166695
Our order no	: 531420-6
Invoice no	:
Packing list no	: KRM101575
Product	: 2.000 x 1250 x 2500
Gross weight	: 5947 Kg
Net weight	: 5767 Kg
Customer part no	:
Alloy/temper	: 105025 14
Customer Spec.	:

	Si	Fe	Cu	Mn	Mg	Zn	Ti	Al
Min								99.50
Max	0.25	0.40	0.05	0.05	0.05	0.07	0.05	
410855	0.06	0.32	0.001	0.002	0.001	0.006	0.009	99.61

Mechanical properties

	Rp0.2	Rm	Elong A50				Thick-ness					
Cust. Min	85	105	4				1.890					
Max		145					2.110					
Coil no. 410855	110	117	9				1.990					

Material Specification and Test Results
Standard EN 485/515/573

Kristian Stray (sign.)
Plant Metallurgist

Astrup AS 10/02/14 GTG
1166695/6 182
AL PL 1050A-H14 2X1250X2500MM
410855

Hydro Aluminium
Rolled Products AS
Karmøy Rolling Mill
N-4265 HAVIK

Vat no: 975 934 578 MVA
Tel: +47 52 85 40 00
Fax: +47 52 85 43 50

CE 1071

ADITYA BIRLA
HINDALCO

HINDALCO INDUSTRIES LIMITED
Ahura Centre, 1st Floor, 82-Mahakali Caves Road, Andheri (East)
Mumbai-400 093.INDIA. Tel:91-22-66917000/26/45
Fax: 91-22-66917056, E-mail: export.hil@adityabirla.com
Regd. Office: Century Bhavan, Dr. Annie Besant Road, Worli,
Mumbai - 400 025, INDIA.

Date : 05-JUN-14
Page 1 of 1

CERT.3.1 B DIN EN 10204

NAME OF THE PARTY :- ASTRUP AS,POSTBOKS 8 HAUGENSTUA,0915 OSLO,NORWAY.,
PRODUCT :- AL.UM.INI.UM PLAIN SHEET IN 1050 H14 TEMPER MILL FINISHCONFORMING TO EN-AW STANDARDS
QTY (MT) :- 24.398
LC / NO. 4869 RIR1457097 P.O NO. 1195833
INVOICE NO:- RFG/R/2015/332

THE TEST RESULTS OF THE SAMPLES DRAWN FROM THE ABOVE LOT AND TESTED IN OUR LABORATORY ARE AS FOLLOWS :

Package Nos./ Batch Nos.	Alloy Temper	Size (MM)	Qty (MT)	Coil Nos.	Cast No./Heat No	Chemical Composition										Mechanical Properties			
						%Si	%Fe	%Mn	%Mg	%Cu	%Zn	%Cr	%Zr	%Ti	%Pb	%Al	%Elong	Bend Test	UTS (ksi)	PS (ksi)
2S140203960	AA1050 , H14	3000 X 1500 X 1.50	1.100	AC11194/3	AC11194	.1	.3	.005	.002	.004	.002	.002		.025	0	99.55	12	0 T Satisfactory	15.34	13.92
2S140204527	AA1050 , H14	2500 X 1250 X 0.80	1.083	B82781/5	14S1050-42-01/4	.1	.28	.01	.002	.003	.002	.002		.009	0	99.592	7	0 T Satisfactory	16.9	16.05
2S140203958	AA1050 , H14	3000 X 1500 X 1.50	1.059	AC11194/2	AC11194	.1	.3	.005	.002	.004	.002	.002		.025	0	99.56	12	0 T Satisfactory	15.34	13.92
2S140204525	AA1050 , H14	2500 X 1250 X 0.80	1.074	B82781/1	14S1050-42-01/4	.1	.28	.01	.002	.003	.002	.002		.009	0	99.592	7	0 T Satisfactory	16.9	16.05
2S140204541	AA1050 , H14	3000 X 1500 X 1.25	1.058	AC11191/1/1	AC11191	.1	.28	.015	.002	.005	.002	.002		.02	0	99.574	12	.5 T Satisfactory	15.34	13.49
2S140204446	AA1050 , H14	2500 X 1250 X 1.00	1.057	B82098/2	14S1050-38-05/1	.08	.24	.002	.002	.003	.002	.002		.01	0	99.659	7	0 T Satisfactory	15.34	14.48
2S140205895	AA1050 , H14	2000 X 1000 X 3.00	1.054	B83134/3	14S1050-48-1/8	.08	.25	.002	.002	.003	.002	.001		.008	.001	99.651	10	.5 T Satisfactory	15.9	14.77
2S140204441	AA1050 , H14	2500 X 1250 X 1.00	1.053	B82098/1	14S1050-38-04/2	.09	.26	.002	.002	.004	.003	.002		.01	0	99.627	7	0 T Satisfactory	15.9	15.05
2S140203919	AA1050 , H14	2500 X 1500 X 1.25	1.088	AC11190/2/1	AC11190	.1	.3	.02	.002	.005	0	0		.03	0	99.543	12	0 T Satisfactory	15.40	14.63
2S140203958	AA1050 , H14	3000 X 1500 X 1.50	1.057	AC11194/1	AC11194	.1	.3	.005	.002	.004	.002	.002		.025	0	99.56	12	0 T Satisfactory	15.34	13.92
2S140204526	AA1050 , H14	2500 X 1250 X 0.80	1.078	B82781/2	14S1050-42-01/4	.1	.28	.01	.002	.003	.002	.002		.009	0	99.592	7	0 T Satisfactory	16.9	16.05
2S140204461	AA1050 , H14	2500 X 1250 X 1.00	1.044	B82098/2	14S1050-38-04/2	.09	.26	.002	.002	.004	.003	.002		.01	0	99.627	7	0 T Satisfactory	15.9	15.05
2S140205897	AA1050 , H14	2000 X 1000 X 3.00	1.057	B83134/1	14S1050-48-1/8	.08	.25	.002	.002	.003	.002	.001		.008	.001	99.651	10	.5 T Satisfactory	15.9	14.77
2S140203562	AA1050 , H14	2500 X 1500 X 1.25	1.078	AC11191/2/1	AC11191	.1	.28	.015	.002	.005	.002	.002		.02	0	99.574	11	0 T Satisfactory	15.34	14.2
2S140204542	AA1050 , H14	3000 X 1500 X 1.25	1.058	AC11191/1/2	AC11191	.1	.28	.015	.002	.005	.002	.002		.02	0	99.574	12	.5 T Satisfactory	15.34	13.49
2S140203955	AA1050 , H14	2500 X 1500 X 1.25	1.088	AC11191/2/4	AC11191	.1	.28	.015	.002	.005	.002	.002		.02	0	99.574	11	0 T Satisfactory	15.34	14.2
2S140205898	AA1050 , H14	2000 X 1000 X 3.00	1.058	B83134/2	14S1050-48-1/8	.08	.25	.002	.002	.003	.002	.001		.008	.001	99.651	10	.5 T Satisfactory	15.9	14.77
2S140204543	AA1050 , H14	3000 X 1500 X 1.25	1.058	AC11191/1/3	AC11191	.1	.28	.015	.002	.005	.002	.002		.02	0	99.574	12	.5 T Satisfactory	15.34	13.49
2S140204447	AA1050 , H14	2500 X 1250 X 1.00	0.961	B82098/3	14S1050-38-05/1	.08	.24	.002	.002	.003	.002	.002		.01	0	99.659	7	0 T Satisfactory	15.34	14.48
2S140204445	AA1050 , H14	2500 X 1250 X 1.00	1.057	B82098/1	14S1050-38-05/1	.08	.24	.002	.002	.003	.002	.002		.01	0	99.659	7	0 T Satisfactory	15.34	14.48
2S140203954	AA1050 , H14	2500 X 1500 X 1.25	1.089	AC11191/2/3	AC11191	.1	.28	.015	.002	.005	.002	.002		.02	0	99.574	11	0 T Satisfactory	15.34	14.2
2S140203953	AA1050 , H14	2500 X 1500 X 1.25	1.078	AC11191/2/2	AC11191	.1	.28	.015	.002	.005	.002	.002		.02	0	99.574	11	0 T Satisfactory	15.34	14.2
2S140204482	AA1050 , H14	2500 X 1250 X 1.00	1.054	B82098/3	14S1050-38-04/2	.09	.26	.002	.002	.004	.003	.002		.01	0	99.627	7	0 T Satisfactory	15.9	15.05
		TOTAL:-	24.398																

EMAIL : hindalco@adityabirla.com CIN - L27020MH1958PLC011238 PH. No. OFFICE, O.P. - 022-66917000 WEBSITE - www.hindalco.com

FOR HINDALCO INDUSTRIES LIMITED

Astrup AS 30/07/14 kim
1195833/1 101
AL PL 1050A – H14 0,8X1250X2500MM
B82791

Appendix D

```
clc
clear all
%%%%%%%%%%%%%%%%%%%%%%%%%%%%%%%%%%%%%%%%%%%%%%%%%%%%%%%%%%%%%%%%%%%%%%%%%%%%%%%
%  Define foam density parameters
%%%%%%%%%%%%%%%%%%%%%%%%%%%%%%%%%%%%%%%%%%%%%%%%%%%%%%%%%%%%%%%%%%%%%%%%%%%%%%%
rho0     =     2.7;% Base material density
minrho   =    0.30;% minimum density
maxrho   =    0.52;% maximum density
minpos   =    38.0;% minimum density position
maxpos   =     0.0;% maximum density position
%%%%%%%%%%%%%%%%%%%%%%%%%%%%%%%%%%%%%%%%%%%%%%%%%%%%%%%%%%%%%%%%%%%%%%%%%%%%%%%
%  Define some parameters for the mesh related quantities
%%%%%%%%%%%%%%%%%%%%%%%%%%%%%%%%%%%%%%%%%%%%%%%%%%%%%%%%%%%%%%%%%%%%%%%%%%%%%%%
node     = csvread('node_foam40.csv'); % read nodes from foam part
stackup  =       3;% direction for foam density gradient (1=x,2=y,3=z)
partname = 'Aluminum foam Core-1';
%%%%%%%%%%%%%%%%%%%%%%%%%%%%%%%%%%%%%%%%%%%%%%%%%%%%%%%%%%%%%%%%%%%%%%%%%%%%%%%
%  Define material properties parameters
%%%%%%%%%%%%%%%%%%%%%%%%%%%%%%%%%%%%%%%%%%%%%%%%%%%%%%%%%%%%%%%%%%%%%%%%%%%%%%%
nu    = 0.0;
nup   = 0.0;
kuchc = 1.0;
alpha = sqrt(9.0*(1.0-2*nup)/(2*(1+nup)));
%
%  All material parameter are defined as X = C1+C2*(rhof/rho0)^n
%
% Young's modulus dependency
C0_E =      272.3;
C1_E =  2.031e+06;
n_E  =       3.57;
% Yield stress dependency (sigmap)
C0_sigmap =      0.0;
C1_sigmap =      803;
n_sigmap  =     2.54;
% hardening parameters dependency (alpha2)
C0_alpha2 =      0.0;
C1_alpha2 =      105;
n_alpha2  =     0.84;
% hardening parameters dependency (1/beta)
C0_beta =       0.46;
C1_beta =       11.4;
n_beta  =       2.01;
% hardening parameters dependency (gamma)
C0_gamma =       0.0;
C1_gamma =       275;
n_gamma  =      1.73;
% fracture parameters dependency (W)
C0_W =       0.0;
C1_W =      41.3;
n_W  =      2.21;
%%%%%%%%%%%%%%%%%%%%%%%%%%%%%%%%%%%%%%%%%%%%%%%%%%%%%%%%%%%%%%%%%%%%%%%%%%%%%%%
%  Generate material card
%%%%%%%%%%%%%%%%%%%%%%%%%%%%%%%%%%%%%%%%%%%%%%%%%%%%%%%%%%%%%%%%%%%%%%%%%%%%%%%
rhodis    =   0.05; % step for tabulated foam density dependency
```

```
rhof      =   (minrho:rhodis:maxrho);
maxstrain =                    1.86; % maximum plastic strain
straininc =           maxstrain/1000;
p         = (0:straininc:maxstrain)';
%%%%%%%%%%%%%%%%%%%%%%%%%%%%%%%%%%%%%%%%%%%%%%%%%%%%%%%%%%%%%%%%%%%%%%%%%%%%%%%
%  Write material card
%%%%%%%%%%%%%%%%%%%%%%%%%%%%%%%%%%%%%%%%%%%%%%%%%%%%%%%%%%%%%%%%%%%%%%%%%%%%%%%
disp('Write material card');
fich=fopen('mat3.inp','w');
% Write material card name
fprintf(fich,'*Material, name="Aluminum Foam"\n');
% Write density
fprintf(fich,'*Density, dependencies=1\n');
for j=1:length(rhof)
    fprintf(fich,'%6d,%6d,%6d\n',rhof(j)*1e-10,0.0,rhof(j));
end
% Write elastic properties
fprintf(fich,'*Elastic, dependencies=1\n');
for j=1:length(rhof)
    fprintf(fich,'%6d,%6d,%6d,%6d\n',C0_E+C1_E*(rhof(j)/rho0)^n_E,nu,0.0,rhof(j));
end
% Write crushable foam keyword
fprintf(fich,'*Crushable Foam, hardening=ISOTROPIC\n');
fprintf(fich,'%6d,%6d\n',kuchc,nup);
% Write crushable foam hardening
fprintf(fich,'*Crushable Foam Hardening, dependencies=1\n');% copy this section to add another
part
% Write Foam density zero for interpolation purposes
fprintf(fich,'**Foam density zero for interpolation purposes\n');
sigmap = C0_sigmap+C1_sigmap*(rhof(1)/rho0)^n_sigmap;
alpha2 = C0_alpha2+C1_alpha2*(rhof(1)/rho0)^n_alpha2;
gamma  = C0_gamma+C1_gamma*(rhof(1)/rho0)^n_gamma;
beta   = 1.0/(C0_beta+C1_beta*(rhof(1)/rho0)^n_beta);
epsD   = -(9.0+alpha^2)/(3*alpha^2)*log(rhof(1)/rho0);
model  = sigmap+gamma*p/epsD+alpha2*log(1./(1-(p/epsD).^beta));
for i=1:length(p)
    if p(i,1) < epsD
       fprintf(fich,'%6d,%6d,%6d,%6d\n',model(i,1),p(i,1),0.0,0.0);
    end
end
% Write all the discretized foam densities
for j=1:length(rhof)
    sigmap = C0_sigmap+C1_sigmap*(rhof(j)/rho0)^n_sigmap;
    alpha2 = C0_alpha2+C1_alpha2*(rhof(j)/rho0)^n_alpha2;
    gamma  = C0_gamma+C1_gamma*(rhof(j)/rho0)^n_gamma;
    beta   = 1.0/(C0_beta+C1_beta*(rhof(j)/rho0)^n_beta);
    epsD   = -(9.0+alpha^2)/(3*alpha^2)*log(rhof(j)/rho0);
    model  = sigmap+gamma*p/epsD+alpha2*log(1./(1-(p/epsD).^beta));
    fprintf(fich,['**Foam density' num2str(rhof(j)) '\n']);
    for i=1:length(p)
        if p(i,1) < epsD
           fprintf(fich,'%6d,%6d,%6d,%6d\n',model(i,1),p(i,1),0.0,rhof(j));
        end
    end
end
% Write Foam density base material for interpolation purposes
fprintf(fich,'**Foam density base material for interpolation purposes\n');
sigmap = C0_sigmap+C1_sigmap*(rhof(end)/rho0)^n_sigmap;
```

```
alpha2 = C0_alpha2+C1_alpha2*(rhof(end)/rho0)^n_alpha2;
gamma  = C0_gamma+C1_gamma*(rhof(end)/rho0)^n_gamma;
beta   = 1.0/(C0_beta+C1_beta*(rhof(end)/rho0)^n_beta);
epsD   = -(9.0+alpha^2)/(3*alpha^2)*log(rhof(end)/rho0);
model  = sigmap+gamma*p/epsD+alpha2*log(1./(1-(p/epsD).^beta));
for i=1:length(p)
    if p(i,1) < epsD
       fprintf(fich,'%6d,%6d,%6d,%6d\n',model(i,1),p(i,1),0.0,rho0);
    end
end
% Add fracture model
fprintf(fich,'*Depvar, delete=3\n');
fprintf(fich,'3,\n');
fprintf(fich,'1,PEEQ,"equivalent plastic strain"\n');
fprintf(fich,'2,DAMAGE,"Damage"\n');
fprintf(fich,'3,FAIL,"Failure status"\n');
fprintf(fich,'*User Defined Field, properties=7\n');
fprintf(fich,'**C0S, C1S, nFS, C0W, C1W, nFW, rho0\n');
fprintf(fich,'%6d,%6d,%6d,%6d,%6d,%6d,%6d\n',C0_sigmap,C1_sigmap,n_sigmap,C0_W,C1_W,n_W,rho0);
%fprintf(fich,'*Damage Initiation, criterion=DUCTILE\n');
%fprintf(fich,'%6d,%6d,%6d\n', 0.3,0.33,0);
%fprintf(fich,'*Damage Evolution, type=DISPLACEMENT\n');
%fprintf(fich,'%6d,\n',0.001);
fclose(fich);
%%%%%%%%%%%%%%%%%%%%%%%%%%%%%%%%%%%%%%%%%%%%%%%%%%%%%%%%%%%%%%%%%%%%%%%%%%%%%%%
% Generate text file with node set
%%%%%%%%%%%%%%%%%%%%%%%%%%%%%%%%%%%%%%%%%%%%%%%%%%%%%%%%%%%%%%%%%%%%%%%%%%%%%%%
layers = unique(node(:,stackup+1)); % Extract the different layers in the mesh
density_node_set = interp1([minpos,maxpos],[minrho,maxrho],layers); % interpolate foam density
on the layers
% Write the text file with the node set
fich=fopen('set3.inp','w');
for i=1:length(layers)
    fprintf(fich,['*Nset, nset=layer_' num2str(i) ',instance="' partname '"\n']);
    [R,C] = find(node(:,stackup+1) == layers(i));
    k = 1;
    for j=1:length(R)
        if k < 16
           fprintf(fich,'%g,',R(j));
           k = k +1;
        else
           fprintf(fich,'%g\n',R(j));
           k = 1;
        end
        if j==length(R)
           if k ~= 16
              fprintf(fich,'\n');
           end
        end
    end
end
fclose(fich);
%%%%%%%%%%%%%%%%%%%%%%%%%%%%%%%%%%%%%%%%%%%%%%%%%%%%%%%%%%%%%%%%%%%%%%%%%%%%%%%
% Generate text file with initial foam density
%%%%%%%%%%%%%%%%%%%%%%%%%%%%%%%%%%%%%%%%%%%%%%%%%%%%%%%%%%%%%%%%%%%%%%%%%%%%%%%
fich=fopen('initial_conditions3.inp','w');
fprintf(fich,'*initial conditions, type=FIELD, variable=1\n');
for i=1:length(layers)
```

```
    fprintf(fich,['layer_' num2str(i) ',%6d\n'],density_node_set(i));
end
fclose(fich);
```

Write material card

Published with MATLAB® R2013a

Appendix E

Abaqus input file.

```
*Heading
** Job name: Skum-350-fine Model name: Sandwich-shell-350-fine
** Generated by: Abaqus/CAE 6.13-1
*Preprint, echo=NO, model=NO, history=NO, contact=NO
**
** PARTS
**
*Part, name="Aluminum foam Core"
*Node
*Element, type=C3D8R
*Nset, nset=_PickedSet2, internal, generate
    1,  18207,      1
*Elset, elset=_PickedSet2, internal, generate
    1,  15000,      1
** Section: Foam Core
*Solid Section, elset=_PickedSet2, controls=EC-1, material="Aluminum Foam"
*End Part
**
*Part, name="Back layer"
*Node
*Element, type=S4R
*Nset, nset=Set-1, generate
   1,  2601,     1
*Elset, elset=Set-1, generate
   1,  2500,     1
** Section: Back layer
```

*Shell Section, elset=Set-1, material="Aluminum Alloy", controls=EC-1, section integration=GAUSS

0.8, 3

*End Part

**

*Part, name="Front layer"

*Node

*Element, type=S4R

*Nset, nset=_PickedSet2, internal, generate

1, 2601, 1

*Elset, elset=_PickedSet2, internal, generate

1, 2500, 1

** Section: Front layer

*Shell Section, elset=_PickedSet2, material="Aluminum Alloy", controls=EC-1, section integration=GAUSS

0.8, 3

*End Part

**

**

** ASSEMBLY

**

*Assembly, name=Assembly

**

*Instance, name="Aluminum foam Core-1", part="Aluminum foam Core"

310., 0., 0.

*End Instance

**

*Instance, name="Back layer-1", part="Back layer"

310., -50., 0.

*End Instance

**

```
*Instance, name="Front layer-1", part="Front layer"
      310.,        -40.,         38.
*End Instance
**
*Nset, nset=Set-1, instance="Aluminum foam Core-1"
*Elset, elset=Set-1, instance="Aluminum foam Core-1"
*Nset, nset=Set-2, instance="Aluminum foam Core-1"
*Elset, elset=Set-2, instance="Aluminum foam Core-1"
*Nset, nset=Set-4, instance="Aluminum foam Core-1"
*Elset, elset=Set-4, instance="Aluminum foam Core-1"
*Nset, nset=_PickedSet76, internal, instance="Back layer-1"
*Elset, elset=_PickedSet76, internal, instance="Back layer-1"
*Nset, nset=_PickedSet77, internal, instance="Front layer-1"
*Elset, elset=_PickedSet77, internal, instance="Front layer-1"
*Nset, nset=_PickedSet78, internal, instance="Aluminum foam Core-1"
*Elset, elset=_PickedSet78, internal, instance="Aluminum foam Core-1"
*Elset, elset="_Back layer front surface_SPOS", internal, instance="Back layer-1", generate
   1,  2500,     1
*Surface, type=ELEMENT, name="Back layer front surface"
"_Back layer front surface_SPOS", SPOS
*Elset, elset="_Core Layer Back Surface_S5", internal, instance="Aluminum foam Core-1"
*Surface, type=ELEMENT, name="Core Layer Back Surface"
"_Core Layer Back Surface_S5", S5
*Elset, elset="_Core Layer Front Surface_S3", internal, instance="Aluminum foam Core-1"
*Surface, type=ELEMENT, name="Core Layer Front Surface"
"_Core Layer Front Surface_S3", S3
*Elset, elset="_Front layer back layer_SNEG", internal, instance="Front layer-1", generate
   1,  2500,     1
*Surface, type=ELEMENT, name="Front layer back layer"
"_Front layer back layer_SNEG", SNEG
```

*Elset, elset=__PickedSurf73_SNEG, internal, instance="Back layer-1", generate

1, 2500, 1

*Surface, type=ELEMENT, name=_PickedSurf73, internal

__PickedSurf73_SNEG, SNEG

*include,input=set5.inp

*End Assembly

**

** ELEMENT CONTROLS

**

*Section Controls, name=EC-1, ELEMENT DELETION=YES

1., 1., 1.

*Amplitude, name=Amp-1

0., 0.44, 0.001, 0.410170128, 0.002, 0.382203325, 0.003, 0.355988819

0.004, 0.331422209, 0.005, 0.30840511, 0.006, 0.286844815, 0.007, 0.266653973

0.008, 0.247750289, 0.009, 0.230056237, 0.01, 0.213498792, 0.011, 0.198009175

0.012, 0.183522611, 0.013, 0.169978105, 0.014, 0.157318224, 0.015, 0.145488898

0.016, 0.134439226, 0.017, 0.124121296, 0.018, 0.114490016, 0.019, 0.105502951

0.02, 0.097120172, 0.021, 0.089304114, 0.022, 0.082019435, 0.023, 0.075232896

0.024, 0.068913236, 0.025, 0.063031055, 0.026, 0.057558715, 0.027, 0.052470229

0.028, 0.047741172, 0.029, 0.043348589, 0.03, 0.039270908, 0.031, 0.035487861

0.032, 0.031980408, 0.033, 0.028730666, 0.034, 0.02572184, 0.035, 0.022938161

0.036, 0.020364823, 0.037, 0.017987932, 0.038, 0.015794446, 0.039, 0.01377213

0.04, 0.011909505, 0.041, 0.010195804, 0.042, 0.008620933, 0.043, 0.007175424

```
        0.044,     0.005850407,          0.045,     0.004637566,          0.046,     0.003529111,
0.047,     0.002517746
        0.048,     0.001596636,          0.049,     0.000759384,          0.05,          0.
**
** MATERIALS
**
*include,input=mat5.inp
*Material, name="Aluminum Alloy"
*Damage Initiation, criterion=DUCTILE
 0.07, 0.33,   0.
*Damage Evolution, type=DISPLACEMENT
 0.001,
*Density
 2.7e-09,
*Elastic
70000., 0.33
*Plastic
 110.6,   0.
 116.5, 0.07
**
** INTERACTION PROPERTIES
**
*Surface Interaction, name=IntProp-1
*Surface Interaction, name=IntProp-2
*Surface Interaction, name=IntProp-3
*Friction
 0.1,
*Surface Behavior, pressure-overclosure=LINEAR
1.,
**
** BOUNDARY CONDITIONS
```

```
**
** Name: BC-1 Type: Displacement/Rotation
*Boundary
_PickedSet76, 1, 1
_PickedSet76, 2, 2
_PickedSet76, 3, 3
_PickedSet76, 4, 4
_PickedSet76, 5, 5
_PickedSet76, 6, 6
** Name: BC-2 Type: Displacement/Rotation
*Boundary
_PickedSet77, 1, 1
_PickedSet77, 2, 2
_PickedSet77, 3, 3
_PickedSet77, 4, 4
_PickedSet77, 5, 5
_PickedSet77, 6, 6
** Name: BC-3 Type: Displacement/Rotation
*Boundary
_PickedSet78, 1, 1
_PickedSet78, 2, 2
_PickedSet78, 3, 3
_PickedSet78, 4, 4
_PickedSet78, 5, 5
_PickedSet78, 6, 6
**
** INTERACTIONS
**
** Interaction: Int-3
*Contact, op=NEW
```

```
*Contact Inclusions, ALL EXTERIOR
*Contact Property Assignment
 ,  , IntProp-3
*include,input=initial_conditions5.inp
** ----------------------------------------------------------------
**
** STEP: Pressure Wave
**
*Step, name="Pressure Wave", nlgeom=YES
*Dynamic, Explicit
, 0.03
*Bulk Viscosity
0.06, 1.2
*field,variable=1
**
** LOADS
**
** Name: Load-1   Type: Pressure
*Dsload, amplitude=Amp-1
_PickedSurf73, P, 1.
**
** OUTPUT REQUESTS
**
*Restart, write, number interval=1, time marks=NO
**
** FIELD OUTPUT: F-Output-1
**
*Output, field, number interval=50
*Node Output
U,
```

```
*Element Output, directions=YES
DMICRT, FV, LE, PE, S, SDEG, STATUS, PEEQ
**
** HISTORY OUTPUT: H-Output-1
**
*Output, history, variable=PRESELECT, time interval=0.0006
*End Step
```